

Metal Oxo Clusters: Molecular Design for Extreme Ultraviolet Lithography



Lianjia Wu

Metal oxo clusters: molecular design for extreme ultraviolet lithography

Cover design by Lianjia Wu

ISBN: 978-94-6423-038-3

Digital version is available at <http://dare.uva.nl/en>

Printed and bound by ProefschriftMaken

Metal oxo clusters: molecular design for extreme ultraviolet lithography

ACADEMISCH PROEFSCHRIFT

ter verkrijging van de graad van doctor
aan de Universiteit van Amsterdam
op gezag van de Rector Magnificus
prof. dr. ir. K.I.J. Maex
ten overstaan van een door het College voor Promoties ingestelde commissie,
in het openbaar te verdedigen in de Agnietenkapel
op woensdag 18 november 2020, te 16:00 uur

door
Lianjia Wu

geboren te Fujian

Promotiecommissie:

Promotor:

prof. dr. A.M. Brouwer

Universiteit van Amsterdam

Copromotor:

dr. S. Castellanos Ortega

Advanced Research Center for Nanolithography

Overige leden:

prof. dr. W.J. Buma

Universiteit van Amsterdam

prof. dr. B. de Bruin

Universiteit van Amsterdam

dr. S. Grecea

Universiteit van Amsterdam

prof. dr. R. Coehoorn

Technische Universiteit Eindhoven

prof. dr. M. Tromp

Rijksuniversiteit Groningen

dr. R. Fallica

IMEC, Leuven, Belgium

Faculteit der Natuurwetenschappen, Wiskunde en Informatica

The research described in this thesis was carried out at the Advanced Research Center for Nanolithography (ARCNL), a public-private partnership of University of Amsterdam (UvA), the Vrije Universiteit Amsterdam (VU), the Netherlands Organisation for Scientific Research (NWO) and the semiconductor equipment manufacturer ASML.



Contents

1	Introduction	1
1.1	Extreme ultraviolet (EUV) lithography	2
1.2	EUV photoresists	3
1.2.1	Polymer-based resists	4
1.2.2	Low molecular-weight organic resists	6
1.2.3	Inorganic resists	6
1.2.4	Metal-based hybrid resists	7
1.3	Outline and scope of this thesis	8
	Bibliography	9
2	Effect of metal oxo core	13
2.1	Introduction	14
2.2	Experimental	15
2.2.1	Materials and characterization	15
2.2.2	Film deposition	15
2.2.3	EUV exposure	16
2.2.4	Post-exposure analysis	16
2.3	Results and discussion	17
2.3.1	Lithographic performance	17
2.3.2	Origin of the solubility switch	19
2.4	Conclusion	26
	Bibliography	27
3	The role of the organic shell	29
3.1	Introduction	30
3.2	Experimental	31
3.2.1	Materials	31

3.2.2	Ligand exchange reaction and thin film deposition	31
3.2.3	EUV exposure and characterization	31
3.3	Results and discussion	32
3.3.1	Effect of doping ligand on sensitivity	32
3.3.2	Effect of doping ligand on dense-lines and contact-holes/pillars printing	35
3.4	Conclusion	36
	Bibliography	38
4	Hybrid EUV resists with mixed organic shells	41
4.1	Introduction	42
4.2	Experimental	44
4.3	Results and discussion	46
4.3.1	Equilibrium adsorption of resins	46
4.3.2	Ligand ratios in mixed organic shells	47
4.3.3	Metal oxo clusters with mixed organic shells as EUV resists	50
4.4	Conclusion	51
	Bibliography	52
5	Hole stabilizing ligands in Ti-based metal oxo clusters	55
5.1	Introduction	56
5.2	Experimental	57
5.3	Results and Discussion	58
5.3.1	Calculated frontier molecular orbitals	58
5.3.2	Determination of the onset for ionization	59
5.3.3	Fragmentation yields as a function of the irradiation energy	62
5.4	Conclusion	63
	Bibliography	64
6	A fluorescent ligand in a Zr-based metal oxo cluster	67
6.1	Introduction	68
6.2	Experimental	70
6.3	Results and discussion	71
6.3.1	EUV lithography	71
6.3.2	Fluorescence labeling	73
6.3.3	Fourier-transform infrared spectra	75
6.3.4	UV-visible absorption spectra	76
6.3.5	Mechanisms of changes in the sensitivity and fluorescence intensity	77
6.4	Conclusion	79
	Bibliography	80

7	Effect of fluorinated ligands in hybrid EUV photoresists	83
7.1	Introduction	84
7.2	Experimental	85
7.2.1	Thin-film deposition and EUV exposure	85
7.2.2	Near edge X-ray absorption fine structure (NEXAFS)	86
7.2.3	X-ray photoelectron spectroscopy (XPS)	86
7.3	Results and Discussion	86
7.3.1	The effect of fluorinated ligands on resist sensitivity	86
7.3.2	NEXAFS	88
7.3.3	X-ray photoelectron spectra	93
7.4	Conclusion	94
	Bibliography	96
8	Fluorine-rich zirconium oxo clusters	99
8.1	Introduction	100
8.2	Experimental	101
8.2.1	Synthesis	101
8.2.2	Thin film deposition	102
8.2.3	EUV exposure and post-exposure characterization	102
8.3	Results and discussion	102
8.3.1	EUV absorptivity enhancement by fluorinated ligands	102
8.3.2	Solubility test and effect of developers	103
8.3.3	Effect of post-exposure bake	106
8.3.4	EUV-induced chemical changes in ZrTFMc	107
8.3.5	Mechanistic insights in PEB	109
8.4	Conclusion	112
	Bibliography	112
	Summary	115
	Samenvatting	119
	List of Publications	123
	Acknowledgments	125

CHAPTER 1

Introduction

1.1 Extreme ultraviolet (EUV) lithography

The invention and development of metal-oxide-semiconductor (MOS) transistors and integrated circuits¹ have shaped electronic devices from the giant first-generation electronic computer ENIAC to a laptop about 20 mm thick or a smartphone that fits in your pocket today with incredible increase in the computing performance and drop in the cost.

Back to the early days of the integrated circuit, Gordon Moore made the prediction in 1965 that for the next decade the number of components in an integrated circuit could be doubled every year.² In 1975, he modified the statement to “every two years”, which later became known as Moore’s law.³ Just a year before, Robert Dennard published a paper about optimization of transistor performance by scaling down physical dimensions of the device, known as Dennard scaling.⁴ Guided by these two “laws”, the semiconductor industry pursues the scaling down of devices, although this trend has slowed down in recent years (Fig. 1.1).

Integrated circuits are manufactured using a technology called photolithography. The minimum feature size that can be printed on chips depends on the wavelength used in photolithography, given by an equation derived from Rayleigh’s resolution criterion: $R = k_1 \lambda / NA$,⁵ where k_1 is a process-dependent parameter, λ is the wavelength of the light source, and NA is the numerical aperture of the optics systems. In deep ultraviolet lithography (DUVL) with ArF laser ($\lambda = 193$ nm), the regular photolithography cannot print features smaller than 48 nm with a single projection because of the physical limits of the optics ($k_1 > 0.25$ and $NA < 1$). The use of immersion fluid (water) brings the feature size down to 39 nm ($k_1 = 0.27$ and $NA = 1.35$).⁶ Sub-20 nm resolution can be achieved by double or multiple patterning in ArF immersion lithography, which requires additional processes.

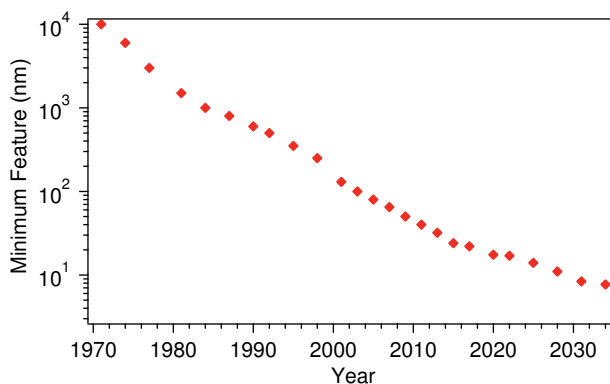


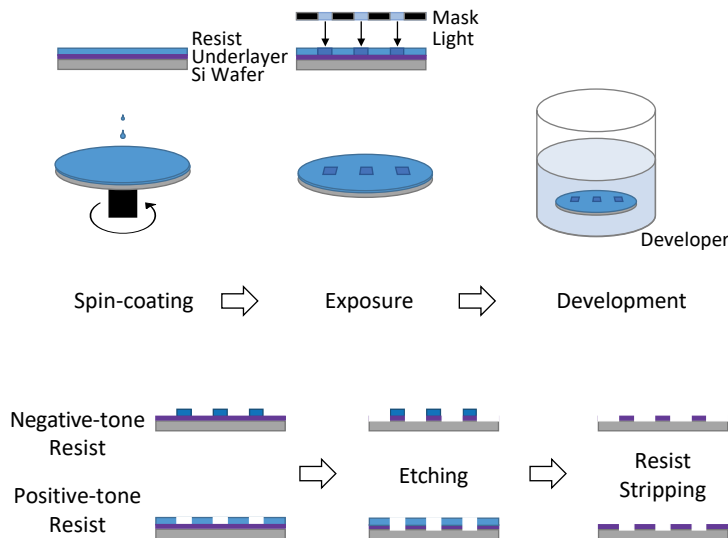
Figure 1.1: Scaling of minimum features from lithography technology requirements of Semiconductor Industry Association (SIA), International Technology Roadmap for Semiconductors (ITRS) and International Roadmap for Devices and Systems (IRDS).^{7–9}

XUV is a range of radiation with wavelength from *ca.* 10 to 100 nm, where the X stands for Extended or Extreme, but in the context of photolithography, extreme UV, abbreviated as EUV, specifically refers to light with a wavelength of 13.5 nm. Utilizing such shorter wavelength in comparison to DUVL, EUVL can pattern sub-20 nm features in one single lithographic cycle with a larger processing window (regarding k_1). For this reason, it is considered as the next generation lithography for 10 nm feature size and beyond. In fact, EUVL is in use for high-volume manufacturing (HVM) since 2020.¹⁰

1.2 EUV photoresists

Photoresists are essential in photolithography. Scheme 1.1 shows the basic lithographic steps that involve photoresists. The typical procedure starts with spin-coating a photoresist onto a silicon wafer. The resist thin film is exposed to light ($\lambda = 13.5$ nm, $E = 92$ eV) through or reflected from a mask and the exposure induces chemical changes in the exposed area of the photoresist. This leads to a solubility contrast between the exposed and unexposed areas in a suitable developer, either in a negative-tone or a positive-tone way. This means that the dissolution rate of the exposed resist is increased (positive-tone) or decreased (negative-tone) compared to the unexposed material in the developer. The designed pattern in the mask is therefore transferred to the photoresist layer after exposure and developing and, ultimately, to the Si wafer by means of etching and stripping.

Radiation-induced solubility contrast is a basic property of photoresists. The resist performance is characterized by sensitivity, resolution, and critical dimension



Scheme 1.1: The main steps in photolithography.

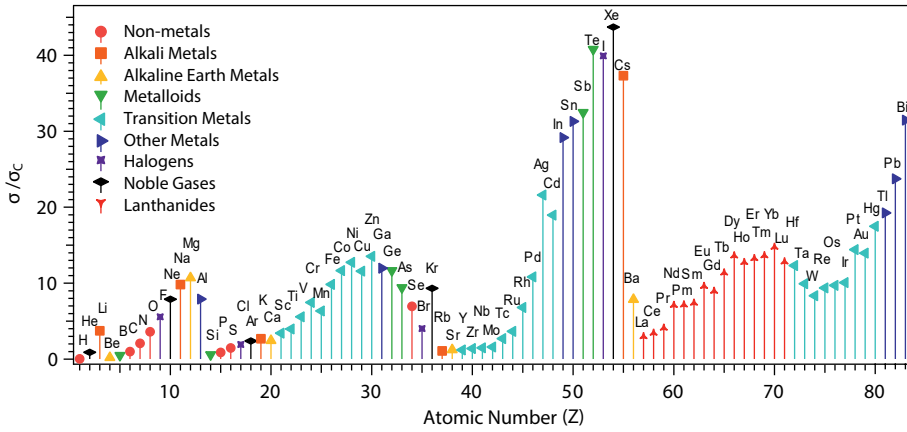


Figure 1.2: Relative photoabsorption cross sections at 92 eV of elements from $Z = 1$ to 83, normalized to carbon. Adapted from Refs. 11 and 12.

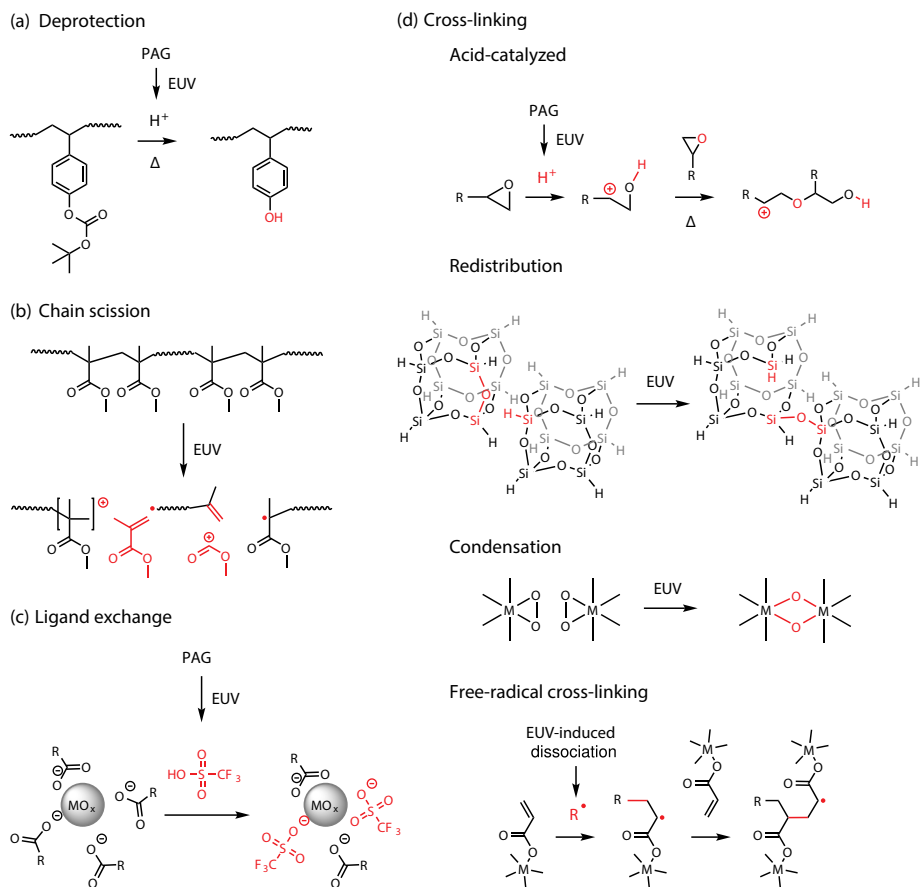
deviation. The latter can be quantified as line edge roughness (LER), line width roughness (LWR), or local critical dimension uniformity (LCDU). Sensitivity can be described by the dose of exposure in different ways, *i.e.* the minimum dose of exposure required to print desired patterns (dose-to-size), to leave negative-tone resists insoluble (dose-to-gel), or to completely remove positive-tone resists (dose-to-clear) after development, expressed in mJ/cm^2 . Resolution is the minimum feature, *i.e.* critical dimension that can be printed, expressed in nm. LER or LWR is commonly used for lines-and-spaces patterns while LCDU is typically used for contact holes or pillars. Each parameter describes the deviation from an ideal smooth feature shape, expressed in nm.

The development of new EUV photoresist materials that meet the requirements of future technologies can only be enabled by understanding the fundamental patterning mechanisms, which differ in the various resist platforms and depend on the material composition. Most EUV resists have evolved from materials initially developed for ultraviolet or electron beam lithography (EBL), including polymer-based resists, low molecular-weight organic resists, and inorganic resists. Metal-containing hybrid resists is a new category specifically chosen for EUV lithography on account of their higher EUV absorptivity arising from their metallic elements in comparison to organic materials comprised of C, H, and O (Fig. 1.2).

1.2.1 Polymer-based resists

Chemically amplified resists

Organic polymer-based chemically amplified resists (CARs) are commonly used in UV lithography.¹³ Typically, CARs are composed of a polymer matrix bearing acid-sensitive side-chains blended with photoacid generators (PAGs) which gen-



Scheme 1.2: Literature examples of patterning mechanism proposed in different material platforms: (a) deprotection in PHS matrix; (b) chain scission of PMMA; (c) ligand exchange of PAG-loaded metal oxide nanoparticles or metal clusters; and (d) cross-linking, such as photoacid-catalyzed cross-linking of epoxy, irradiation induced redistribution of hydrogen silsesquioxane, condensation of metal peroxide, and free-radical cross-linking of C=C double bonds. Adapted from Refs. 14–22.

erate acids upon irradiation. During exposure, photoacids are generated in the exposed area; in the following step of post-exposure bake, the acids diffuse and catalyze the size-chain cleavage (deprotection). The polarity of the deprotected polymer differs from the pristine material and thus results in solubility contrast between exposed and unexposed areas. An example of poly-(4-hydroxystyrene) (PHS)-based chemically amplified resist is shown in Scheme 1.2a.

The low absorbance towards EUV light limits the sensitivity of those organic resists based on C, H, and O. For the improvement in EUV reactivity, polymer-

based CARs in EUVL are typically loaded or blended with enhancers, such as a high ratio of PAGs,¹⁷ a sensitizer unit containing metal or halogen,^{23,24} an acid amplifier,^{25–27} and an acid-generating promoter.²⁸

Chain scission resists

Another type of polymer-based non-chemically amplified EUV resists is based on chain scission reactions. One of the examples is poly(methyl methacrylate) (PMMA), which works as a positive-tone photoresist in both EBL and EUVL, as shown in Scheme 1.2b. Other examples include polysulfone, ZEP resists (1:1 α -chloromethacrylate and α -methylstyrene copolymers), hemicellulose, *etc.*^{29–31}

In chain scission resists, the molecular weight (Mw) of the polymer plays an important role. It is reported that polymer resists with higher Mw show higher chemical contrast and better EUV-printability but lower sensitivity.^{16,32} Metals have been incorporated into this type of resist for absorption enhancement as well. For instance, antimony is incorporated to the polymer side chain in the form of antimonate in MAPDSA-MAPDST copolymer (MAPDSA = (4-(methacryloyloxy)phenyl)dimethylsulfonium hexafluoroantimonate and MAPDST = (4-(methacryloyloxy)phenyl)dimethylsulfonium triflate).³³ A new process of pre-exposure metal insertion of tellurium and tin has been proposed on an organic chain-scission resist.³¹

1.2.2 Low molecular-weight organic resists

Apart from cleavage of protecting groups, photoacids can catalyze cross-linking reactions of small molecules, which is also applicable to EUV resists (Scheme 1.2d), such as molecular glass and multi-trigger resists.^{34,35} Those low molecular-weight organic resists have shown potential in printing smaller features and improving LER comparing to high molecular-weight polymers.^{36,37}

1.2.3 Inorganic resists

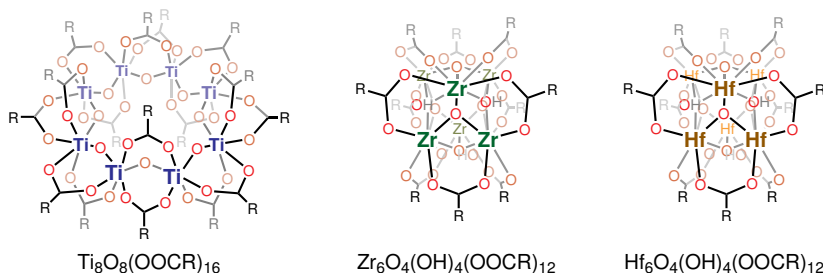
Hydrogen silsesquioxane (HSQ) and hafnium oxide peroxide hydroxide sulfate (HafSO_x) resists are inorganic non-chemically amplified EUV resists.^{21,38} The cleavage and redistribution of Si–O–Si and Si–H bonds on adjacent HSQ cages lead to cross-linking of HSQ, while in HafSO_x , radiation-induced desorption of oxygen brings about the condensation of the material for solubility switching (Scheme 1.2d).^{20,21} HSQ is used in EBL as a high-resolution resist for sub-10 nm features and holds a resolution record of 6-nm half-pitch in EUVL at an extremely high dose of 7500 mJ/cm².³⁹ HafSO_x is also a high-resolution (8 nm) resist in EUV patterning.⁴⁰ This material is deposited from an aqueous precursor of $\text{Hf}(\text{OH})_{4-2x-2y}(\text{O}_2)_x(\text{SO}_4)_y \cdot q\text{H}_2\text{O}$ and therefore the distribution of size and composition of the material can be expected. This distribution results in a distribution of solubility shifts upon exposure, leading to large roughness in the patterns.

1.2.4 Metal-based hybrid resists

Incorporating metal elements provides resist not only with enhanced EUV absorptivity but also with better etching resistance.^{41,42} Such advances make metal-based hybrid resists one of the most promising resist platforms for EUVL. The first metal-containing hybrid resists are metal-oxide nanoparticles blended with PAGs.^{43,44} The proposed patterning mechanism is the surface ligand exchange by the photoacids, as shown in Scheme 1.2c.^{17,45} Similar to polymers, the size distribution of nanoparticles limits the resist performance. The ligand exchange mechanism proposed in nanoparticle resists was recently also applied to smaller molecules of zinc dimers for high-resolution patterning.¹⁸ Metal-containing molecular materials have been studied as new resist platforms, including metal oxo clusters based on Sn (also known as Sn-oxo cages)^{46,47} and metal complex-type molecular organometallic resists (MORE) based on Cr, Fe, Co, Sn,⁴⁸ Pt, Pd,⁴⁹ Te, Bi, and Sb.²² In olefin-metal complexes, free radical polymerization reactions upon EUV exposure were proposed as the patterning mechanism (Scheme 1.2d).²² In oxalate-metal complexes, ligand dissociation and following condensation have been proposed for the formation of solubility contrast.⁴⁹

Metal oxo clusters with group 4 metals as resist platform

Inspired by the works on nanoparticles and sol-gel metal clusters as EUV and DUV resists,^{50,51} we choose carboxylato-substituted metal oxo clusters (MOCs) based on group 4 metals (Ti, Zr, and Hf) as the model photoresist materials (Scheme 1.3). Those MOCs are secondary building units (SBU) of metal-organic frameworks (MOFs) such as Ti-MIL-125,⁵² Zr- or Hf-UiO-66,⁵³ Zr-MOF-525, Zr-MOF-535,⁵⁴ and Hf-NU-1000⁵⁵ with good chemical stability. The well-defined and stable molecular structure allows for spectroscopic analysis of the EUV-induced chemical changes in the materials. Besides, the dynamics of their carboxylate ligands in solution and retention of the cluster core structure during ligand exchange reactions enable the relatively easy modification of these molecules.^{56,57} The introduction of different functional groups is performed for tuning the EUV reactivity and printability of these materials.



Scheme 1.3: MOCs studied as model EUV photoresist materials in this thesis. R denotes different functional groups.

1.3 Outline and scope of this thesis

In the mechanisms summarized above, photoacid-catalyzed deprotection and cross-linking are proposed based on studies of UV-induced chemistry. The chain-scission, bond-redistribution, and condensation reactions are based on studies of electron beam-induced chemistry. Few are verified with experiments performed using EUV irradiation. Part of the work in this thesis has been carried out at the Swiss Light Source, where powerful research tools of EUV open-frame exposure and EUV interference lithography are provided. This thesis focuses on understanding how the compositions of molecular hybrid photoresists influence the EUV-induced chemistry and ultimate lithographic performance of the materials.

In Chapter 2 we compare the resist behavior of MOCs based on different metals (Ti, Zr and Hf) featuring the same methacrylate ligands. We further investigate the EUV-induced chemical changes accounting for the solubility switch of methacrylate MOCs via multiple *ex-situ* spectroscopic techniques. In Chapters 3 and 4, we study the impact of organic components on MOCs sensitivity as EUV resists. Chapter 3 also serves as the motivation for Chapters 5–7 where the effects of different functional groups on the EUV reactivity of the material are further discussed. In Chapter 4, we describe a simple method to prepare MOCs with mixed organic shells. In Chapter 5 we investigate the photoionization process of a series of titanium oxo clusters doped with extended aromatic structures. This chapter presents photoionization studies of Ti-based MOCs in the gas phase upon VUV radiation in the range of 7–12 eV in combination with DFT calculations. In Chapter 6, we functionalize methacrylate zirconium oxo clusters with one of the ligands studied in the previous chapter to make it a fluorescent EUV photoresist. Fluorescence spectroscopy and microscopy combined with infrared and UV-visible absorption spectroscopy are utilized to investigate the EUV reactivity of the material. In Chapter 7 we study the chemical changes in a partially fluorinated zirconium oxo cluster after EUV exposure in comparison to its non-fluorinated analog using X-ray spectroscopy. Chapter 8 describes a fluorine-rich zirconium oxo cluster as an EUV resist, demonstrating that the modification of the organic components in the molecular design of metal-based hybrid materials can improve the EUV absorptivity and lithographic performance significantly.

Bibliography

- [1] J. S. Kilby, *IEEE Trans. Electron Devices*, 1976, **23**, 648–654.
- [2] G. E. Moore, *Electronics*, 1965, **38**, 114.
- [3] G. E. Moore, *International Electron Devices Meeting, IEEE*, 1975, **21**, 11–13.
- [4] R. H. Dennard, F. H. Gaensslen, H.-N. Yu, V. L. Rideout, E. Bassous and A. R. LeBlanc, *IEEE J. Solid-State Circuits*, 1974, **9**, 256–268.
- [5] U. Okoroanyanwu, *Chemistry and Lithography*, SPIE Press, 2010.
- [6] A. Yen, H. Meiling and J. Benschop, *2019 Electron Devices Technology and Manufacturing Conference (EDTM)*, 2019, 475–477.
- [7] W. J. Spencer and T. E. Seidel, in *Productivity and Cyclicity in Semiconductors: Trends, Implications, and Questions: Report of a Symposium*, National Academies Press, 2004, p. 137.
- [8] *ITRS Reports*, <http://www.itrs2.net/>.
- [9] *IRDS Reports*, <https://irds.ieee.org/>.
- [10] <https://news.samsung.com/global/samsung-electronics-begins-mass-production-at-new-euv-manufacturing-line>.
- [11] B. L. Henke, E. M. Gullikson and J. C. Davis, *At. Data Nucl. Data Tables*, 1993, **54**, 181–342.
- [12] R. Fallica, J. Haitjema, L. Wu, S. Castellanos, , A. M. Brouwer and Y. Ekinici, *Proc. SPIE*, 2017, **10143**, 101430A.
- [13] E. Reichmanis, F. M. Houlihan, O. Nalamasu and T. X. Neenan, *Adv. Mater. Opt. Electron.*, 1994, **4**, 83–93.
- [14] J. M. J. Frechet, E. Eichler, H. Ito and C. G. Willson, *Polymer*, 1983, **24**, 995–1000.
- [15] V. Bermudez, *J. Vac. Sci. Technol. B*, 1999, **17**, 2512–2518.
- [16] A. Rathore, I. Pollentier, H. Singh, R. Fallica, D. De Simone and S. De Gendt, *J. Mater. Chem. C*, 2020, **8**, 5958–5966.
- [17] L. Li, X. Liu, S. Pal, S. Wang, C. K. Ober and E. P. Giannelis, *Chem. Soc. Rev.*, 2017, **46**, 4855–4866.
- [18] H. Xu, K. Sakai, K. Kasahara, V. Kosma, K. Yang, H. C. Herbol, J. Odent, P. Clancy, E. P. Giannelis and C. K. Ober, *Chem. Mater.*, 2018, **30**, 4124–4133.
- [19] H. S. Yu, T. Yamashita and K. Horie, *Macromolecules*, 1996, **29**, 1144–1150.
- [20] D. L. Olynick, B. Cord, A. Schipotin, D. F. Ogletree and P. J. Schuck, *J. Vac. Sci. Technol. B*, 2010, **28**, 581–587.
- [21] R. T. Frederick, J. M. Amador, S. Goberna-Ferron, M. Nyman, D. A. Keszler and G. S. Herman, *J. Phys. Chem. C*, 2018, **122**, 16100–16112.
- [22] J. Passarelli, M. Murphy, R. Del Re, M. Sortland, L. Dousharm, M. Vockenhuber, Y. Ekinici, M. Neisser, D. A. Freedman and R. L. Brainard, *Proc. SPIE*, 2015, **9425**, 94250T.

- [23] J. Jiang, D. De Simone and G. Vandenberghe, *J. Photopolym. Sci. Technol.*, 2017, **30**, 591–597.
- [24] J. Jiang, G. Giordano, R. Fallica, D. De Simone and G. Vandenberghe, *J. Photopolym. Sci. Technol.*, 2019, **32**, 21–25.
- [25] S. Kruger, S. Revuru, C. Higgins, S. Gibbons, D. A. Freedman, W. Yueh, T. R. Younkin and R. L. Brainard, *J. Am. Chem. Soc.*, 2009, **131**, 9862–9863.
- [26] S. A. Kruger, C. Higgins, B. Cardineau, T. R. Younkin and R. L. Brainard, *Chem. Mater.*, 2010, **22**, 5609–5616.
- [27] S. Kruger, K. Hosoi, B. Cardineau, K. Miyauchi and R. Brainard, *Proc. SPIE*, 2012, **8325**, 832514.
- [28] S. Fujii, K. Okamoto, H. Yamamoto, T. Kozawa and T. Itani, *Jpn. J. Appl. Phys.*, 2017, **56**, 06GD01.
- [29] K. J. Lawrie, I. Blakey, J. P. Blinco, H. H. Cheng, R. Gronheid, K. S. Jack, I. Pollentier, M. J. Leeson, T. R. Younkin and A. K. Whittaker, *J. Mater. Chem.*, 2011, **21**, 5629–5637.
- [30] T. G. Oyama, A. Oshima, M. Washio and S. Tagawa, *AIP Adv.*, 2011, **1**, 042153.
- [31] K. Morita, K. Yamamoto, M. Harumoto, Y. Tanaka, C. Mori, Y. Arisawa, T. Motono, H. Stokes and M. Asai, *Proc. SPIE*, 2020, **11326**, 113260C.
- [32] T. R. Böhme and J. J. de Pablo, *J. Chem. Phys.*, 2002, **116**, 9939–9951.
- [33] C. A. da Silva Moura, G. K. Belmonte, P. G. Reddy, K. E. Gonslaves and D. E. Weibel, *RSC Adv.*, 2018, **8**, 10930–10938.
- [34] D. Yang, S. W. Chang and C. K. Ober, *J. Mater. Chem.*, 2006, **16**, 1693–1696.
- [35] A. Frommhold, A. McClelland, D. Yang, R. E. Palmer, J. Roth, Y. Ekinici, M. C. Rosamund and A. P. G. Robinson, *Proc. SPIE*, 2015, **9425**, 942504.
- [36] A. De Silva, N. Felix, J. Sha, J.-K. Lee and C. K. Ober, *Proc. SPIE*, 2008, **6923**, 69231L.
- [37] C. Popescu, G. O’Callaghan, A. McClelland, J. Roth, T. Lada and A. P. G. Robinson, *Proc. SPIE*, 2020, **11326**, 1132611.
- [38] I. Junarsa, M. P. Stoykovich, P. F. Nealey, Y. Ma, F. Cerrina and H. H. Solak, *J. Vac. Sci. Technol. B*, 2005, **23**, 138–143.
- [39] D. Fan and Y. Ekinici, *J. Micro/Nanolithogr., MEMS, MOEMS*, 2016, **15**, 033505.
- [40] N. Mojarad, M. Hojeij, L. Wang, J. Gobrecht and Y. Ekinici, *Nanoscale*, 2015, **7**, 4031–4037.
- [41] M. Trikeriotis, M. Krysak, Y. S. Chung, C. Ouyang, B. Cardineau, R. L. Brainard, C. K. Ober, E. P. Giannelis and K. Cho, *J. Photopolym. Sci. Technol.*, 2012, **25**, 583–586.
- [42] D. De Simone, M. Mao, M. Kocsis, P. De Schepper, F. Lazzarino, G. Vandenberghe, J. Stowers, S. Meyers, B. L. Clark, A. Grenville, V. Luong, F. Yamashita and D. Parnell, *Proc. SPIE*, 2016, **9776**, 97760B.

- [43] M. Trikeriotis, W. J. Bae, E. Schwartz, M. Kryszak, N. Lafferty, P. Xie, B. Smith, P. A. Zimmerman, C. K. Ober and E. P. Giannelis, *Proc. SPIE*, 2010, **7639**, 76390E.
- [44] M. Kryszak, M. Trikeriotis, E. Schwartz, N. Lafferty, P. Xie, B. Smith, P. Zimmerman, W. Montgomery, E. Giannelis and C. K. Ober, *Proc. SPIE*, 2011, **7972**, 79721C.
- [45] S. Chakrabarty, C. Ouyang, M. Kryszak, M. Trikeriotis, K. Cho, E. P. Giannelis and C. K. Ober, *Proc. SPIE*, 2013, **8679**, 867906.
- [46] B. Cardineau, R. Del Re, M. Marnell, H. Al-Mashat, M. Vockenhuber, Y. Ekinci, C. Sarma, D. A. Freedman and R. L. Brainard, *Microelectron. Eng.*, 2014, **127**, 44–50.
- [47] Y. Zhang, J. Haitjema, X. Liu, F. Johansson, A. Lindblad, S. Castellanos, N. Ottosson and A. M. Brouwer, *J. Micro/Nanolithogr., MEMS, MOEMS*, 2017, **16**, 023510.
- [48] R. Del Re, J. Passarelli, M. Sortland, B. Cardineau, Y. Ekinci, E. Buitrago, M. Neisser, D. A. Freedman and R. L. Brainard, *J. Micro/Nanolithogr., MEMS, MOEMS*, 2015, **14**, 043506.
- [49] M. Sortland, R. Del Re, J. Passarelli, J. Hotalen, M. Vockenhuber, Y. Ekinci, M. Neisser, D. A. Freedman and R. L. Brainard, *Proc. SPIE*, 2015, **9422**, 942227.
- [50] J. Jiang, S. Chakrabarty, M. Yu and C. K. Ober, *J. Photopolym. Sci. Technol.*, 2014, **27**, 663–666.
- [51] F. Stehlin, F. Wieder, A. Spangenberg, J.-M. Le Meins and O. Soppera, *J. Mater. Chem. C*, 2014, **2**, 277–285.
- [52] M. Dan-Hardi, C. Serre, T. Frot, L. Rozes, G. Maurin, C. Sanchez and G. Férey, *J. Am. Chem. Soc.*, 2009, **131**, 10857–10859.
- [53] J. H. Cavka, S. Jakobsen, U. Olsbye, N. Guillou, C. Lamberti, S. Bordiga and K. P. Lillerud, *J. Am. Chem. Soc.*, 2008, **130**, 13850–13851.
- [54] W. Morris, B. Voloskiy, S. Demir, F. Gandara, P. L. McGrier, H. Furukawa, D. Cascio, J. F. Stoddart and O. M. Yaghi, *Inorg. Chem.*, 2012, **51**, 6443–6445.
- [55] M. H. Beyzavi, R. C. Klet, S. Tussupbayev, J. Borycz, N. A. Vermeulen, C. J. Cramer, J. F. Stoddart, J. T. Hupp and O. K. Farha, *J. Am. Chem. Soc.*, 2014, **136**, 15861–15864.
- [56] P. Walther, M. Puchberger, F. R. Kogler, K. Schwarz and U. Schubert, *Phys. Chem. Chem. Phys.*, 2009, **11**, 3640–3647.
- [57] J. Kreutzer, M. Puchberger, C. Artner and U. Schubert, *Eur. J. Inorg. Chem.*, 2015, **2015**, 2145–2151.

CHAPTER 2

Effect of metal oxo core: Ti, Zr, and Hf-based metal oxo clusters as EUV resists*

Abstract

In this chapter, we compare the sensitivity of metal oxo clusters based on Ti, Zr, and Hf featuring methacrylate ligands (Mc) as EUV photoresist materials. Decarboxylation processes upon EUV exposure were found in all cases with *ex-situ* X-ray photoelectron spectroscopy (XPS) and Fourier-transform infrared spectroscopy (FTIR). However, the structural changes after film deposition and after exposure differed among the three compounds. Higher sensitivity was detected for the Hf-based material than for the Zr-based analogue, in line with its higher absorptivity. XPS analyses suggest that only a small fraction of the carboxylate ligands was lost at the dose-to-gel. This change in the chemical composition is accompanied by an increased structural disorder in the layer and a rather small degree of aggregation, according to grazing incidence small angle X-ray scattering (GISAXS). These results indicate that neither a drastic loss of organic shell nor a high degree of aggregation of the inorganic cores is required for this type of material to reliably operate as an EUV photoresist. Contrarily to what has been reported for other metal-containing EUV photoresists, the solubility switch in these materials mainly proceeds through cross-linking of the organic shells.

*The content of this chapter has been published in: S. Castellanos, L. Wu, M. Baljozovic, G. Portale, D. Kazazis, M. Vockenhuber, Y. Ekinici, T. Jung, *Proc. SPIE* **2018**, 10583, 105830A; L. Wu, M. Baljozovic, G. Portale, D. Kazazis, M. Vockenhuber, T. Jung, Y. Ekinici, S. Castellanos, *J. Micro/Nanolith. MEMS MOEMS* **2019**, 18(1), 013504. The electronic supplementary information is available at <http://dare.uva.nl/en>.

2.1 Introduction

With EUV lithography technology almost ready to be launched for high-volume manufacturing, there are still only few examples of photoresists offering the required performance to have an optimal industrial throughput for features of 10 nm critical dimension.^{1–4} Ideally, a photoresist should render patterns with line-width roughness (LWR) below 20%.^{4–6} Reaching this LWR limit, however, usually requires a dose high enough to allow the photon shot-noise to be on an acceptable level. At the same time, the dose should be low enough (typically defined below 20 mJ/cm²)^{4–6} for exposure times to allow for a high volume throughput.

Resists combining metallic elements and organic moieties are arising as the most promising candidates for the next generation of photoresists.^{1,3} It is generally accepted that the metallic atoms absorb a large fraction of the EUV light^{7,8} while the organic part is responsible for the solubility switching properties.^{9–12} In addition, the inorganic components in the photoresist provide the final patterns with good mechanical and chemical stability.¹³ However, in addition to the absorptivity, other properties arising from the metallic elements can also affect the reactivity—and therefore the sensitivity—of the photoresist. Brainard’s group reported a correlation between the reduction potential of the central metal in oxalate complexes (Co, Fe, and Cr) and their sensitivity,¹² noticing that this series of metals exhibited similar EUV cross-sections. Soppera and coworkers found that TiO_x nanoparticles (labeled as oxoclusters due to their small size but prepared using sol-gel chemistry) were clearly more sensitive towards deep ultraviolet (DUV) light than ZrO_x and HfO_x parent materials, which they attributed to the catalytic role of TiO_x responsible for the fast decarboxylation and mineralization of the material.¹⁴ Works by Ober and Giannelis have shown that both zirconium oxide and hafnium oxide nanoparticles rendered similar high sensitivity (in the presence of photoacid generator), even though Hf has a higher crosssection than Zr.^{15,16} Further investigations found that the sensitivity of photoresists based on hafnium oxide nanoparticles towards DUV and EUV correlated to the stability of the cluster–ligand bond.⁹ Therefore, it is highly relevant to elucidate what are the exact structural changes occurring right after photon absorption, determining how their efficiency correlates to their molecular composition, and ultimately, optimise the materials to render a maximum solubility switch upon exposure.

In this chapter, we investigate the EUV photochemistry of metal oxo clusters (MOCs) based on Ti, Zr, and Hf and carboxylate ligands prepared as molecular EUV photoresist materials. MOCs comprise a well-defined number of metallic atoms, bridged by O atoms and OH groups in their inorganic cores in a particular fixed arrangement.^{17,18} The number of carboxylate ligands that are coordinated to the metals is also well-defined. Thus, MOCs exhibit a structure composed of an inorganic core and organic shell, like some nanoparticles. Yet, nanoparticles are typically prepared by sol-gel reactions that yield a distribution of different sizes and shapes, whereas MOCs are isolated as single-size molecules packed in molecular crystals that form during equilibrium reactions occurring in anhydrous conditions.

The aim of this study is to compare the photoresist behaviour of hybrid molecular materials with analogous chemical composition (M_xL_{2x} , M = metal, L = ligand) but featuring different inorganic cores in terms of sensitivity and gain understanding in the chemical changes responsible for their solubility switch. The materials were exposed to an EUV interference lithography tool and chemical changes before and after EUV exposures were inspected *ex-situ* by Fourier-transform infrared (FTIR), ultraviolet-visible (UV-vis) absorption, and X-ray photoelectron spectroscopy (XPS). In addition, structural changes in the thin film, such as interparticle distance, were monitored by grazing incidence small angle X-ray scattering (GISAXS).

2.2 Experimental

2.2.1 Materials and characterization

Ti-based methacrylate MOC was synthesized by the reaction of $Ti(OiPr)_4$ with 8.4 molar equivalents of methacrylic acid in nitrogen, adapted from the method reported in the reference¹⁹. The product was identified as the octamer $Ti_8O_8Mc_{16}$ (Fig. 2.1a) by powder X-ray diffraction (PXRD), TGA, IR, and MS (calculated m/z 1872.01; found m/z 1911.94 $[M + K]^+$ (see Fig. 2.2 and Supporting Information)).

Zr-based methacrylate MOC (ZrMc) is commercially available from Sigma-Aldrich. This compound consists of a core of six Zr atoms clustered through four bridging O atoms (μ_3 -O), four bridging OH groups (μ_3 -OH) and twelve carboxylate groups of methacrylate ligands, giving the molecular formula $Zr_6O_4(OH)_4Mc_{12}$ (Mc = methacrylate. Fig. 2.1b).²⁰

Hf-based methacrylate MOC (HfMc) was synthesized following the protocol in the literature.²¹ The product was identified as the hexameric oxocluster with formula $Hf_6O_4(OH)_4Mc_{12}(HOBu)$ (Mc = methacrylate, Bu = butyl. Fig. 2.1c) from PXRD, MS (calculated m/z 2298.08 M; found m/z 2322.81 $[M + Na + 2H]^+$), nmR, IR, and TGA (see Fig. 2.2 and Supporting Information).

NMR analysis was carried out using a Bruker AV-400 NMR spectrometer. The thermogravimetric analyses (TGA) were performed using a NETZSCH thermogravimetric analyzer in an Al_2O_3 crucible. Heating was performed from 35 °C to 800 °C at a rate of 10 K/min in an 80%/20% N_2/O_2 atmosphere. IR of the powder samples was performed in a Bruker ALPHA FTIR spectrometer. PXRD experiments were carried out in a Bruker D2 PHASER diffractometer.

2.2.2 Film deposition

TiMc thin films were spin-coated (2100 rpm for 1 min) from a solution in 9:1 (v/v) $CHCl_3$ and dimethyl sulfoxide (DMSO). Thin films of ZrMc and HfMc were prepared by spin-coating (2100 rpm for 30 s) from a solution (8.4 mg/mL) in a mixed solvent consisting of 9:1 (v/v) chloroform ($CHCl_3$) and propylene glycol methyl ether acetate (PGMEA). Post application baking for 30 s at 90 °C was

applied to remove the remaining solvent. Samples were spin-coated on double-side polished silicon (200 μm thick), quartz (500 μm thick), and Cr/Au coated (2 nm/18 nm) coverslips for FTIR spectroscopy, UV-vis absorption spectroscopy, and XPS analyses, respectively.

2.2.3 EUV exposure

EUV exposures were carried out at the XIL-II beamline of the Swiss Light Source (SLS) synchrotron at the Paul Scherrer Institute (PSI) with EUV light at 92 eV ($\lambda = 13.5$ nm).²⁴ For the open-frame experiments, areas of 0.5×0.5 mm² or 1.7×1.7 mm² were exposed to EUV light through a square aperture. For the patterning experiments, a transmission mask was used providing line/space patterns with pitches of 100, 80, 60, and 44 nm. Chloroform was used as the developer.

2.2.4 Post-exposure analysis

FTIR spectroscopy of the thin films was performed in transmission mode under vacuum in a Bruker Vertex 80v spectrometer. UV-vis absorption spectroscopy was performed in a Shimadzu UV2600 spectrophotometer. XPS experiments were performed *ex-situ* and immediately after EUV exposure at PSI in a SPECS Analyzer Phoibos 150, with monochromatic AlK α source (energy of 1486.6 eV, power 200 W).

Atomic force microscopy (AFM) images were made using a Bruker Dimension Icon, using the PeakForce tapping (ScanAsyst-Air) mode. The raw images were corrected for bowing using first- and second-order corrections, and the film thickness was measured by comparing the height of the film with the height of the substrate. Scanning electron microscopy (SEM) imaging was performed using a FEI Verios 460 with a voltage of 1 kV.

GISAXS experiments were performed both at the beamline BM26B of the European Synchrotron Radiation Facility (ESRF), Grenoble (France) and at the MINA beamline at the University of Groningen (the Netherlands). An X-ray beam

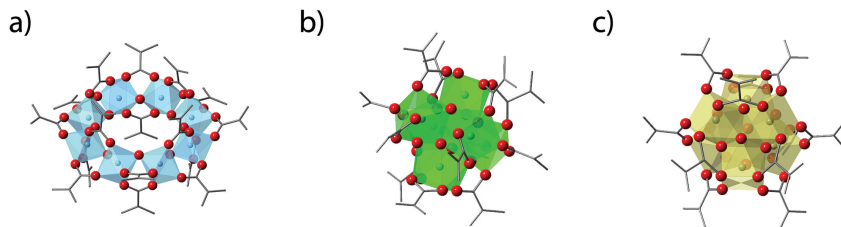


Figure 2.1: Representation MOCs used as EUV photoresists in this work: (a) TiMc, (b) ZrMc, and (c) HfMc. Polygons represent the coordination geometry of the metal cations, red spheres represent oxygen atoms and grey bars C-C bonds. Crystal structures from references^{21–23}.

of about $0.3 \times 0.3 \mu\text{m}^2$ with photon wavelength of 0.1 nm was used at the ESRF. The GISAXS patterns were acquired using a Frelon CCD detector with a pixel size $48 \times 48 \mu\text{m}^2$. The sample-to-detector distance was 173 cm. At the MINA beamline, the X-ray wavelength was 0.154 nm, the circular beam size was about 0.5 mm and the sample-to-detector distance was 24 cm. The detector used was a VANTEC500 multiwire chamber with pixel size of $136 \times 136 \mu\text{m}^2$. Images are presented with respect to the vertical $[q_z = 2\pi/\lambda(\sin\alpha_i + \sin\alpha_f)]$ and horizontal $[q_y = 2\pi/\lambda(\cos\alpha_f \sin 2\theta_f)]$ scattering wavevector, where λ is the X-ray wavelength, $2\theta_f$ is the horizontal scattering angle and α_i and α_f are the incident and vertically scattered angles.

2.3 Results and discussion

2.3.1 Lithographic performance

A critical aspect of pattern formation in inorganic photoresists with metal-oxo cores and organic shells composed of carboxylate ligands is irreversible aggregation/condensation or structural rearrangements upon spin coating and post-application bake.^{25,26} Depending on the extent of these changes, the solubility of the unexposed film can be slightly or drastically decreased. It had been previously observed that upon redissolution of the film made of the commercial ZrMc material, the individual molecular cluster could not be recovered as such.¹⁰ Furthermore, Matson et al. found that the chemical stability of Hf-based oxoclusters with methacrylate ligands upon different postapplication baking conditions had an important effect in the solubility of the thin films prepared with this material.^{26,27} In this work, this material is evidenced to lose the extra carboxylic acid molecules upon deposition. Originally, those carboxylic acids are not covalently bonded to the inorganic core but are occluded in the crystalline sample.²⁸ Their presence in the crystalline powder sample can be detected and in the IR spectrum (Fig. 2.2b–c, C=O stretching at 1697 cm^{-1} and broad band between 2770 and 3515 cm^{-1} due to O–H stretching of the carboxylic acid, marked with asterisk) and it is further supported by the mass ratio between combustible organics and

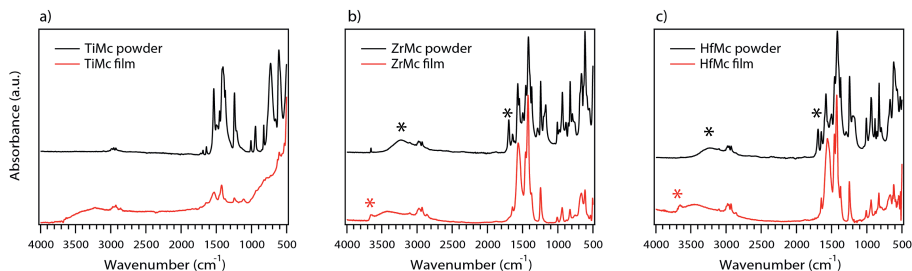


Figure 2.2: IR spectra of (a) TiMc, (b) ZrMc, and (c) HfMc as bulk powder (top, black) and thin film deposited on Si (bottom, red).

incombustible inorganic residue found in the TGA (see Fig. S2.5 and S2.9 in Supporting Information). We hypothesize that these extra non-coordinated ligands might stabilize the cluster in solution and in the crystalline form and that their loss in the thin films might make the clusters more susceptible to hydrolysis and/or rearrangements.

The solubility of TiMc in organic solvents was poor and only films of the order of 10 nm thickness could be obtained thus displaying very low intensity in IR absorption (Fig. 2.2a). Meanwhile, the deposited TiMc film could not be redissolved in chloroform, which was used as the developer for ZrMc and HfMc in this work, or other common organic solvents. This was a strong indication of the instability of these particular clusters during or after film deposition. It is known that carboxylate ligands in oxoclusters can be displaced by water or by competing chelating agents.²⁸ XPS analyses (see Fig. S2.4 in Supporting Information) point in this direction and thus optimisation of spin-coating and sample handling is required for this material. Given the poor solubility of the TiMc film, this material was excluded from the subsequent sensitivity studies. Ti-based MOCs will be further discussed in Chapters 4 and 5.

When comparing the IR spectra of the materials as powders and as thin films (Fig. 2.2), it was observed that the signals arising from extra free methacrylic acid (black asterisks) were barely detected in the thin film, yet the broad band from 2700 to 3700 cm^{-1} might arise from the O-H stretching mode of protonated carboxylic acid. The more defined band at 3670 cm^{-1} (red asterisk), on the other hand, is assigned to the O-H stretching of μ_3 -OH groups bridging metallic atoms in the MOC.^{29,30} It should be noticed, that for HfMc this band was only detectable in the thin film. Nevertheless, this stretching mode can shift to lower wavenumbers when the OH group is involved in hydrogen bonding.²⁹

The lithographic performance of ZrMc and HfMc was tested using synchrotron radiation at the SLS XIL-II endstation.²⁴ The main goal was to compare the sensitivity of the two materials with analog structures and thus the same type of chemical bonding but based on different metals that have different absorption cross-sections to 92-eV photon. Since chloroform can dissolve the original bulk material, the solubility switch induced by EUV light was studied using chloroform as the developer. Even if this might not be the optimal developer, using the same solvent for deposition and development gives direct evidence of chemical changes in the original material. HfMc displayed a lower dose-to-gel D_0 ($< 2 \text{ mJ/cm}^2$) than ZrMc (5 mJ/cm^2) as well as lower doses to attain the retainment of the whole photoresist thickness D_{100} (20 and 34 mJ/cm^2 , respectively, Fig. 2.3a). These trends in sensitivity follow the experimental linear absorptivity trends previously reported for these materials, that is, HfMc, having linear absorptivity $\alpha = 9 \mu\text{m}^{-1}$, needed less EUV photos to gel than ZrMc, with $\alpha = 5 \mu\text{m}^{-1}$.³¹ The effect of thermal treatment was tested by heating the ZrMc sample to 100 °C after exposure (post-exposure baking, PEB). However, PEB did not affect the sensitivity of the ZrMc material thus indicating that no reactive intermediate species were formed after exposure (Fig. 2.3b).

The trends in sensitivity were also observed in dense line pattern transfer

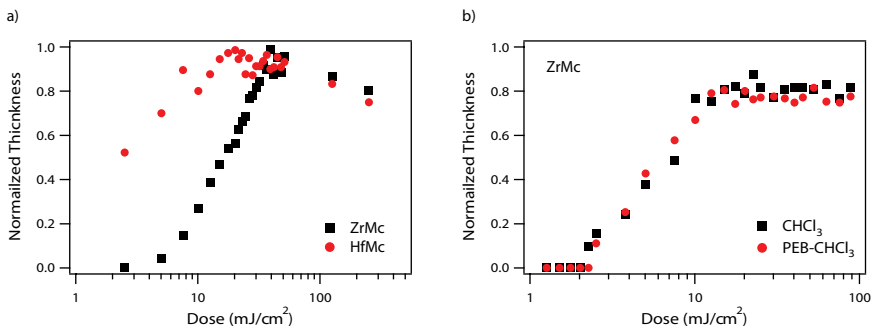


Figure 2.3: Contrast curves of a) ZrMc and HfMc developed in chloroform and b) ZrMc with and without PEB using CHCl_3 as the developer.

(Fig. 2.4). Formation of 50 nm half-pitch lines could be detected on HfMc at doses as low as 3.5 mJ/cm^2 , indicating that a chemical change was promoted with EUV exposure. Nevertheless, the solubility contrast was poor and no lines could be resolved at higher doses. Priming the Si-substrates with hexamethyldisilazane (HMDS) improved the solubility contrast and allowed to attain smaller critical dimensions (22 nm half-pitch).

SEM pictures confirmed that the unexposed material between the exposed lines remains after development for both investigated materials (Fig. 2.5). In the case of HfMc, the detachment of large patches of photoresist was observed after exposure and development (Fig. 2.5c). We suspect that the material changes its structure during the deposition process, leading to interparticle bridging and the formation of aggregates. This causes a decrease in the solubility of the deposited thin film in CHCl_3 . Furthermore, partial hydrolysis during or after deposition can result in strong interactions with the hydrophilic native oxide layer of the silicon wafer. This would explain the effect of HMDS: while aggregates might still form, the weaker interaction of the (partially hydrolyzed) MOCs with the hydrophobic surface can result in the detachment of big areas during the development process.

2.3.2 Origin of the solubility switch

The chemical composition of the materials before and after exposure was investigated by XPS, FTIR, and UV-vis spectroscopy. The aim was to compare the reactivity of the ZrMc and HfMc materials and relate it to the threshold of photoconversion that renders a solubility change.

The metal/O/C elemental ratio for the unexposed films of ZrMc and HfMc was lower than expected (estimated 1:5.3:8, found 1:3:7 in both materials). This ratio might be attributed to a loss of carboxylate ligands upon deposition (*ca.* 1.5 out of 12). It is likely that part of the carboxylate ligands rearranges to form intermolecular bridges between the clusters. For instance, the estimated ratio would match structures, in which three ligands are shared between two clusters on average. Such arrangements had been observed in crystalline structures of this

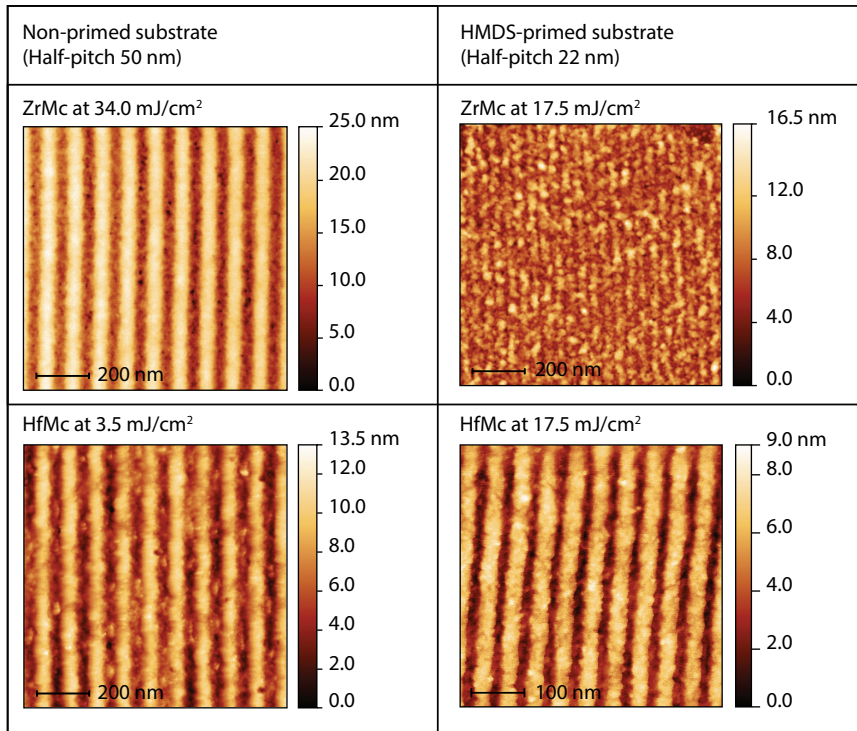


Figure 2.4: AFM images of dense line patterns on ZrMc and HfMc.

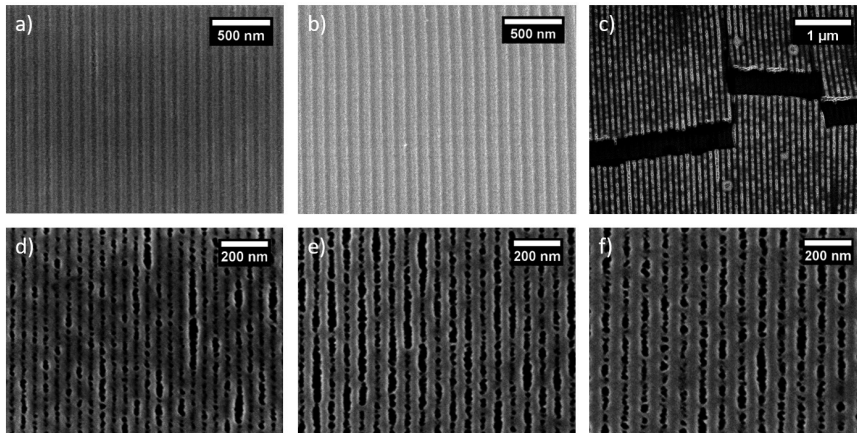


Figure 2.5: SEM images of dense patterns printed with interference lithography. On top, 100 pitch patterns on (a) ZrMc at dose 57 mJ/cm², (b) ZrMc at 106 mJ/cm², and (c) HfMc (on HMDS primed Si) at 20 mJ/cm². On bottom, patterns on HfMc (HMDS primed Si) with (d) 22 nm at 18 mJ/cm², (e) 30 nm at 21 mJ/cm², and (f) 40 nm half pitch at 22 mJ/cm².

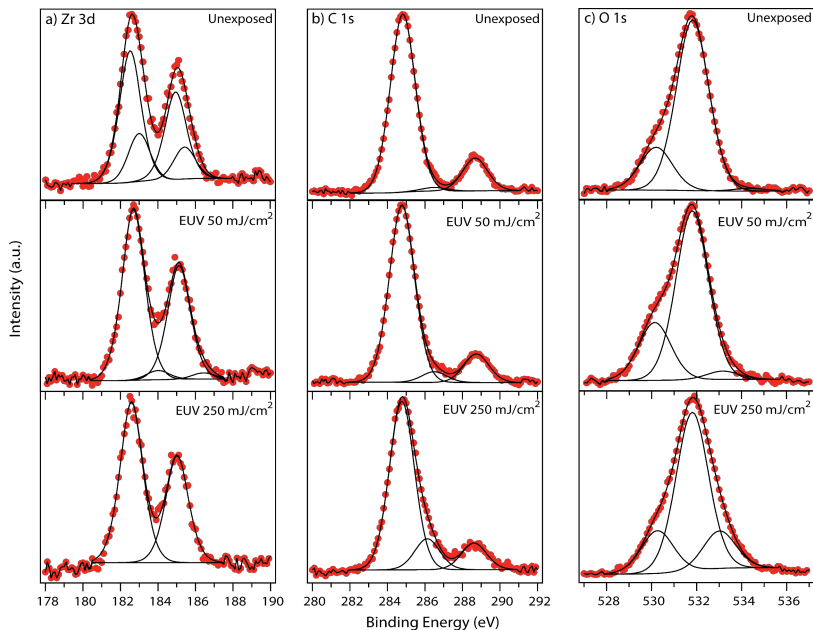


Figure 2.6: High-resolution XPS spectra of (a) Zr 3d (b) C 1s and, and (c) O 1s of ZrMc before and after EUV exposure. Experimental data are shown as dots and fits as continuous lines.

type of compounds.^{23,32} Yet, it should be noted that XPS probes the surface of the film and the ligand loss might be less in the bulk of the layer.

Inspection of the XPS high-resolution spectra for O 1s allows for estimating the degree of decarboxylation at the dose where solubility switch occurs. The proposed fitting (Fig. 2.6) is based on three components assigned to COO (532 eV), Zr–O, such as μ_3 -O groups (530 eV) and to Zr–OH (533 eV).³³ The estimated contribution of the oxygens in the carboxylate group (COO) in the O 1s peak before and after irradiation is shown in Fig. 2.7. A partial decarboxylation was observed, in line with previously reported studies,¹⁰ whereas a rise in the concentration of Zr–OH species was observed. It should be noted that the cluster may hydrate after exposure due to adsorption of moisture from the air, since these are *ex situ* experiments.

Considering that the initial ZrMc material in the thin film contains a maximum of 12 carboxylate ligands per cluster, this would mean a maximum loss of around 1.4 carboxylate groups per cluster on average after 50 mJ/cm². The experimental EUV linear absorptivity of this material ($5 \mu\text{m}^{-1}$)⁷ implies that the transmittance of the 15-nm layer used for XPS is 93%. GISAXS experiments (see below) reveal that the film is still formed of clusters arranged in a disordered manner with interparticle distances similar to the crystalline packing. The number of clusters in a volume of 15 nm \times 1 cm² can thus be estimated from the cluster size and

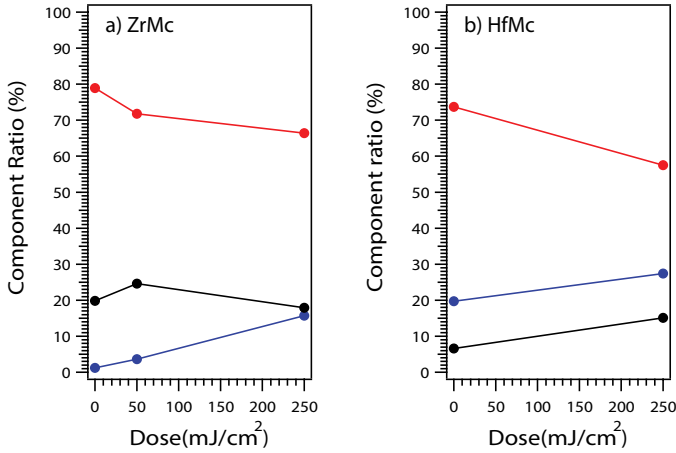


Figure 2.7: The ratio of different components in the O 1s peak in XPS for (a) ZrMc and (b) HfMc changing with EUV doses, M-O (~ 530 eV) in black, COO (~ 532 eV) in red, and MOH (~ 533 eV) in blue.

crystalline density so that an average of 0.2 absorbed photon per cluster is approximated at 50 mJ/cm^2 (1 of every 5 MOC molecules). With this assumption, a rough estimate would be that a maximum of seven carboxylate ligands is lost over five oxoclusters per absorbed photon at 50 mJ/cm^2 , a dose sufficient to induce the solubility change in ZrMc. In the case of HfMc ($9 \mu\text{m}^{-1}$, $T = 87\%$ for a 30-nm layer), only the sample at 250 mJ/cm^2 was available for analysis. At this dose, a 19% loss of the carboxylate groups was detected. Although these numbers are rough approximations, they indicate that the degree of ligand loss is not large at doses where the solubility switch occurs.

FTIR spectra of ZrMc and HfMc exposed materials revealed the partial bleach of the peaks attributed to the COO group stretching modes (Fig. 2.8). Two types of carboxylate ligands can be distinguished in ZrMc and HfMc compounds: bridging ligands, where the COO group binds to two different metallic atoms and chelating ligands, where a COO group is bonded to only one metallic atom. The peaks in the region of the IR spectrum where the vibrations attributed to the chelating COO are expected (1495 and 1459 cm^{-1})³⁴ decreases at a faster rate than those in the region where the vibration modes of the bridging carboxylate ligands are detected ($>1500 \text{ cm}^{-1}$). Such a difference in the decrease rate is more pronounced in the case of HfMc. This trend has been reported for TiO_x , ZrO_x , and HfO_x photoresists upon DUV irradiation,¹⁴ and a faster reaction of chelating carboxylate ligands was also proposed by Ober et al. from XPS analyses of ZrO_x EUV photoresists.¹⁰

A decrease in the bands assigned to the terminal methacrylate group of the ligand ($\nu \text{ C=C}$ at 1643 cm^{-1} and $\nu_s \text{ C(CH}_3\text{)=CH}_2$ at 1246 cm^{-1}) was also detected along with the decarboxylation. The decarboxylation reaction must indeed

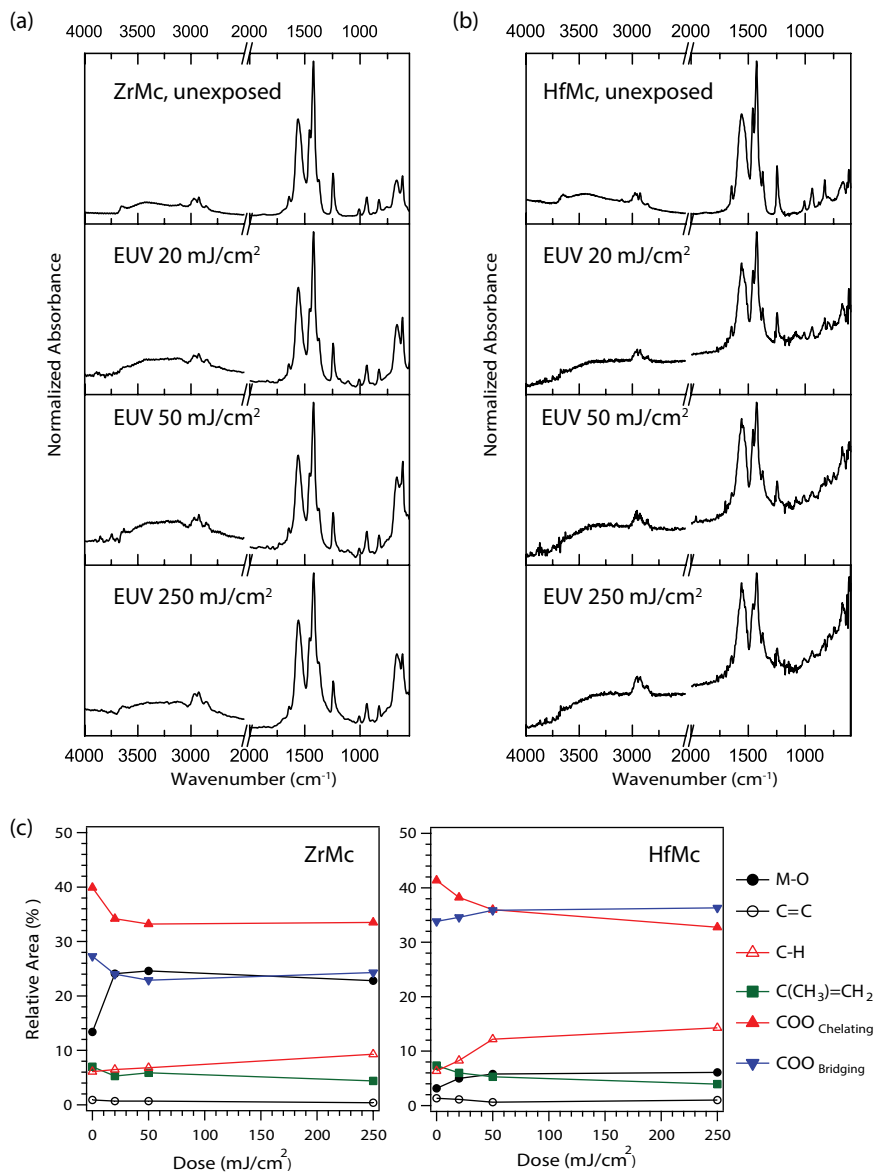


Figure 2.8: Normalized FTIR spectra before and after exposure to different EUV doses of (a) ZrMc and (b) HfMc. (c) Relative integration values (%) of FTIR peaks upon EUV exposure: ν_{as} Zr-O-Zr (714 to 644 cm⁻¹), ν_s C(CH₃)=CH₂ (1246 cm⁻¹), ν_s bridging COO + $\nu_{s/as}$ chelating COO (1488 to 1634 cm⁻¹), and ν C=C (1643 cm⁻¹).^{29,34,35}

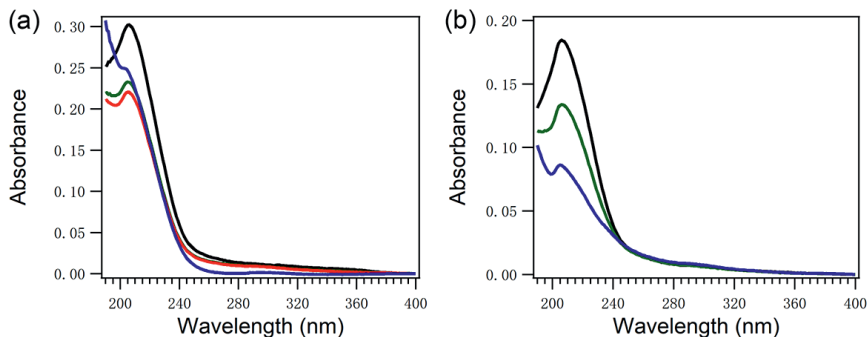


Figure 2.9: UV-vis absorption spectra of (a) ZrMc and (b) HfMc before exposure (black) and after 20 mJ/cm² (green), 50 mJ/cm² (red), and 250 mJ/cm² (blue).

generate an allyl unit, most likely a radical, that could either outgas or react with the neighboring methylene terminal groups initiating a chain reaction and polymerization. The apparent relative increase of the aliphatic C–H stretching is in agreement with such radical-induced reaction.

UV-vis absorption spectra (Fig. 2.9) are in line with the observed changes in XPS and FTIR spectroscopy. A bleach of the absorption band at about 220 nm, attributed to electronic transitions mainly located in the methacrylate ligands ($\pi \rightarrow \pi^*$), is detected. This is an indication of the decrease of terminal double bonds, either due to outgassing or to their radical-induced reaction, which yields single carbon bonds.

In order to gain more insights into the solubility switch mechanism, the particle packing in the amorphous layer before and after EUV exposure was investigated in ZrMc by means of GISAXS experiments. Given the marked difference in density between the carbon-based methacrylate shell and the metal oxo core, X-ray scattering experiments allow for the measurement of the average distance between the inorganic cores. GISAXS experiments were performed on thin films of the soluble material (unexposed) and on thin films of the insoluble material (samples exposed to 50 and 250 mJ/cm² and subsequently developed). The GISAXS patterns in Fig. 2.10a and 2.10b exhibit a single-broad Debye–Scherrer like ring, suggesting that the thin-film structure consists of ZrMc clusters arranged in a 3-D disordered manner.³⁶ Nevertheless, the scattering ring shows some anisotropy suggesting a preferential packing in the direction parallel to the Si substrate, a common arrangement of disordered multilayered nanoparticles.³⁷ The average spacing among clusters along the q_y horizontal direction calculated according to the Bragg’s law from the position of the scattering maxima in the intensity cuts reported in Fig. 2.10d was found to be $d = 2\pi/q_y^{max} = 1.2$ nm for the unexposed ZrMc. These values are in agreement with the cluster packing obtained from XRD data.²³ After exposure, the scattering intensity related to the distance between neighboring clusters becomes weaker. The intensity decrease is mostly due to the smaller areas left after exposure and development of the samples. Indeed, after normalization for

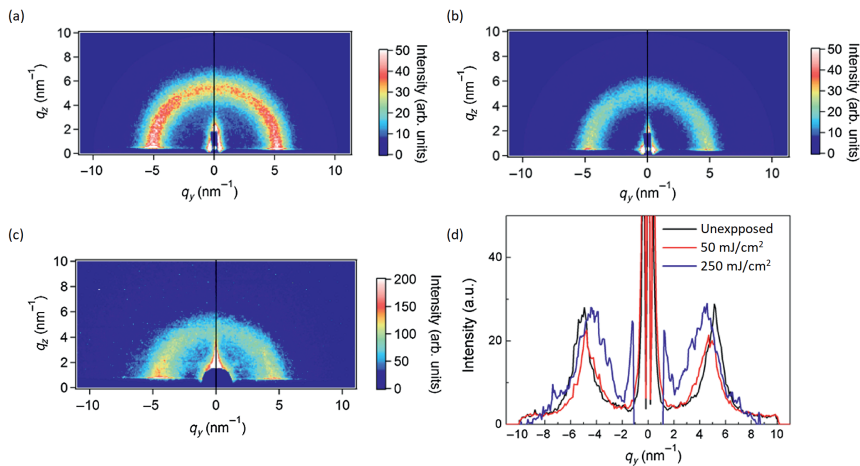


Figure 2.10: GISAXS results for thin films of ZrMc: (a) unexposed, (b) after 50 mJ/cm² exposure and development, (c) after 250 mJ/cm² exposure and development, and (d) comparison of the horizontal intensity cuts as a function of the exposure conditions. The intensity of the cuts has been normalized with respect to the exposure time and the actual sample dimension. For all the samples, the substrate is Si/SiO₂.

the actual sample dimension along the beam path, the unexposed and exposed samples show similar scattered intensity (Fig. 2.10d). After the 50 mJ/cm² dose, a slight broadening and shift of the signal to $d = 1.4$ nm are detected. The broadening and shift are even more pronounced after 250 mJ/cm² dose. This trend is associated with an increase in the packing disorder of the particles, *i.e.*, a wider distribution of interparticle distances, and a small increase of the particle size. These minor changes for both the interparticle distance and peak width observed after 50 mJ/cm² indicate that the degree of aggregation is rather small, which is in line with the low shrinking observed at D_{100} in the contrast curve of this material. It also supports the cross linking of the organic shells as an important part of the solubility switch mechanism.

Based on the spectroscopic and structural studies, we propose the mechanism shown in Fig. 2.11. Upon the irradiation, direct ionization by EUV photons and ionization during electron scattering lead to decarboxylation events and generation of allyl radicals. The latter initiates a chain reaction that cross links the molecular clusters (radical polymerization propagation), leading to a hybrid network that becomes insoluble in chloroform. We hypothesize that the higher absorption of HfMc might lead to a higher number of reactions per incident photon, which leads to a broadening (blur) of the patterned features already at relatively low doses, as discussed in Section 2.3.1.

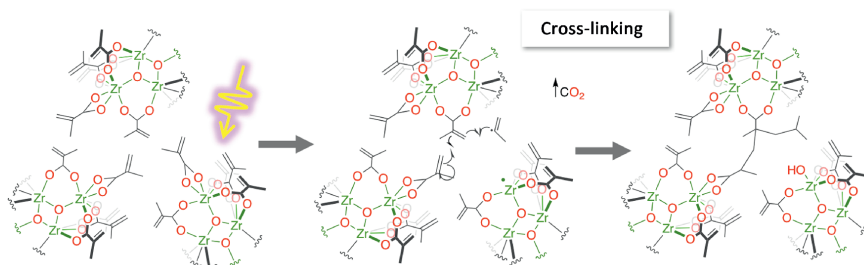


Figure 2.11: Scheme of solubility change mechanism in MOCs featuring methacrylate ligands.

2.4 Conclusion

Metal oxo clusters based on Ti, Zr, and Hf and methacrylate ligands were tested as EUV photoresist materials. Partial loss and rearrangement of carboxylate ligands in this type of compounds can affect the solubility of the thin films after deposition and might be the cause of the scumming in the dense line patterns. These observations highlight the importance of the dynamic bonding between carboxylate binding groups and metal oxo clusters and demand the optimization of the clusters' stability in thin films by molecular engineering, for instance, using more stable binding groups in the organic ligands. HfMc displayed higher sensitivity than ZrMc, thus following the trends in linear absorptivity. Although the structural changes upon EUV exposure for the two types of clusters were similar, a higher reactivity of chelating ligands was detected in HfMc, according to *ex-situ* IR analyses of the thin films. The higher reactivity of HfMc compared to ZrMc is also accompanied by a much marked blur and bridging in the dense line patterns, which could arise from the propagation of cross linking to unexposed areas. X-ray photoelectron spectroscopy indicates that the loss of a small number of carboxylate groups (in the order of 12%) is sufficient to render the solubility switch in ZrMc. This low order of decarboxylation is accompanied by an increase of disorder in the packing of the solid film, which keeps the interparticle distance of the unexposed materials, according to GISAXS experiments. These results manifest that the solubility switch in these materials does not result from a high degree of aggregation of the inorganic cores but arises from other structural rearrangements deriving from decarboxylation reactions, with a high contribution of cross linking of the terminal alkene groups in the organic ligands.

Bibliography

- [1] P. D. Ashby, D. L. Olynick, D. F. Ogletree and P. P. Naulleau, *Adv. Mater.*, 2015, **27**, 5813–5819.
- [2] H. Nakagawa, T. Naruoka and T. Nagai, *J. Photopolym. Sci. Technol.*, 2015, **27**, 739–746.
- [3] L. Li, X. Liu, S. Pal, S. Wang, C. K. Ober and E. P. Giannelis, *Chem. Soc. Rev.*, 2017, **46**, 4855–4866.
- [4] O. Yildirim, E. Buitrago, R. Hoefnagels, M. Meeuwissen, S. Wuister, G. Rispens, A. Van Oosten, P. Derks, J. Finders, M. Vockenhuber and Y. Ekinici, *Proc. SPIE*, 2017, **10143**, 101430Q.
- [5] A. Lio, *Proc. SPIE*, 2016, **9776**, 97760V.
- [6] D. De Simone, V. Rutigliani, G. Lorusso, P. De Bisschop, Y. Vesters, V. B. Carballo and G. Vandenberghe, *Proc. SPIE*, 2018, **10583**, 105830G.
- [7] R. Fallica, J. Haitjema, L. Wu, S. Castellanos, , A. M. Brouwer and Y. Ekinici, *Proc. SPIE*, 2017, **10143**, 101430A.
- [8] R. Fallica, J. K. Stowers, A. Grenville, A. Frommhold, A. P. G. Robinson and Y. Ekinici, *J. Micro/Nanolithogr., MEMS, MOEMS*, 2016, **15**, 033506.
- [9] L. Li, S. Chakrabarty, K. Spyrou, C. K. Ober and E. P. Giannelis, *Chem. Mater.*, 2015, **27**, 5027–5031.
- [10] V. Kosma, K. Kasahara, H. Xu, J. Odent, C. K. Ober and E. P. Giannelis, *J. Micro/Nanolithogr., MEMS, MOEMS*, 2017, **16**, 041007.
- [11] Y. Zhang, J. Haitjema, X. Liu, F. Johansson, A. Lindblad, S. Castellanos, N. Ottosson and A. M. Brouwer, *J. Micro/Nanolithogr., MEMS, MOEMS*, 2017, **16**, 023510.
- [12] S. Grzeskowiak, A. Narasimhan, M. Murphy, L. Napolitano, D. A. Freedman, R. L. Brainard and G. Denbeaux, *Proc. SPIE*, 2017, **10146**, 1014605.
- [13] M. Trikeriotis, M. Krysak, Y. S. Chung, C. Ouyang, B. Cardineau, R. L. Brainard, C. K. Ober, E. P. Giannelis and K. Cho, *J. Photopolym. Sci. Technol.*, 2012, **25**, 583–586.
- [14] F. Stehlin, F. Wieder, A. Spangenberg, J.-M. Le Meins and O. Soppera, *J. Mater. Chem. C*, 2014, **2**, 277–285.
- [15] M. Kryask, M. Trikeriotis, C. Ouyang, S. Chakrabarty, E. P. Giannelis and C. K. Ober, *J. Photopolym. Sci. Technol.*, 2013, **26**, 659–664.
- [16] C. Ober and E. Giannelis, *SPIE Newsroom*, 2014, 2–4.
- [17] U. Schubert, *Chem. Soc. Rev.*, 2011, **40**, 575–582.
- [18] H. Assi, G. Mouchaham, N. Steunou, T. Devic and C. Serre, *Chem. Soc. Rev.*, 2017, **46**, 3431–3452.
- [19] M. Czakler, C. Artner and U. Schubert, *Monatsh. Chem.*, 2015, **146**, 897–902.
- [20] G. Kickelbick and U. Schubert, *Chem. Ber.*, 1997, **130**, 473–477.
- [21] S. Gross, G. Kickelbick, M. Puchberger and U. Schubert, *Monatsh. Chem.*, 2003, **134**, 1053–1063.

- [22] C. Artner, M. Czakler and U. Schubert, *Chem. Eur. J.*, 2014, **20**, 493–498.
- [23] G. Kickelbick, P. Wiede and U. Schubert, *Inorg. Chim. Acta*, 1999, **284**, 1–7.
- [24] N. Mojarad, J. Gobrecht and Y. Ekinici, *Microelectron. Eng.*, 2015, **143**, 55–63.
- [25] L. Li, S. Chakrabarty, J. Jiang, B. Zhang, C. K. Ober and E. P. Giannelis, *Nanoscale*, 2016, **8**, 1338–1343.
- [26] E. C. Mattson, S. M. Rupich, Y. Cabrera and Y. J. Chabal, *Proc. SPIE*, 2018, **10583**, 1058309.
- [27] E. C. Mattson, Y. Cabrera, S. M. Rupich, Y. Wang, K. A. Oyekan, T. J. Mustard, M. D. Halls, H. A. Bechtel, M. C. Martin and Y. J. Chabal, *Chem. Mater.*, 2018, **30**, 6192–6206.
- [28] F. Faccioli, M. Bauer, D. Pedron, A. Sorarù, M. Carraro and S. Gross, *Eur. J. Inorg. Chem.*, 2015, **2015**, 210–225.
- [29] P. Piszczek, A. Radtke, A. Grodzicki, A. Wojtczak and J. Chojnacki, *Polyhedron*, 2007, **26**, 679–685.
- [30] V. Guillermin, S. Gross, C. Serre, T. Devic, M. Bauer and G. Férey, *Chem. Commun.*, 2010, **46**, 767–769.
- [31] R. Fallica, J. Haitjema, L. Wu, S. Castellanos, A. M. Brouwer and Y. Ekinici, *J. Micro/Nanolithogr., MEMS, MOEMS*, 2018, **17**, 023505.
- [32] M. Puchberger, F. R. Kogler, M. Jupa, S. Gross, H. Fric, G. Kickelbick and U. Schubert, *Eur. J. Inorg. Chem.*, 2006, 3283–3293.
- [33] Y. S. Li, P. C. Wong and K. A. R. Mitchell, *Appl. Surf. Sci.*, 1995, **89**, 263–269.
- [34] J. Kreutzer, P. Blaha and U. Schubert, *Comput. Theor. Chem.*, 2016, **1084**, 162–168.
- [35] J. Kreutzer, M. Puchberger, C. Artner and U. Schubert, *Eur. J. Inorg. Chem.*, 2015, **2015**, 2145–2151.
- [36] G. Portale, L. Sciortino, C. Albonetti, F. Giannici, A. Martorana, W. Bras, F. Biscarini and A. Longo, *Phys. Chem. Chem. Phys.*, 2014, **16**, 6649–6656.
- [37] J. Toudert, D. Babonneau, S. Camelio, T. Girardeau, F. Yubero, J. P. Espinós and A. R. Gonzalez-Elipe, *J. Phys. D: Appl. Phys.*, 2007, **40**, 4614–4620.

The role of the organic shell in metal oxo clusters for EUV lithography*

Abstract

In this chapter, we aim for gaining more understanding of the contribution of the organic components in inorganic-organic hybrid molecular resists to their sensitivity towards EUV light. A method to investigate the effect of specific functionalities on the sensitivity of metal oxo clusters is presented, which consists in the “doping” of the methacrylate shell of zirconium oxo clusters through the introduction of fluorinated, iodinated and extended aromatic ligands. By introducing each of these functionalities in small ratios to the methacrylate ligand (1:11 and 2:10) the main physiochemical properties of the materials (solubility and molecular packing in the thin film) are expected to be unaltered. Our investigations show that the sensitivity is enhanced in the presence of halogens and drastically decreased when extended aromatic compounds are introduced. The trends are uncorrelated with the absorptivity estimated for each material, which seems to indicate that the doping functionalities might interfere with the cross-linking of the methacrylate ligands or introduce new chemical pathways. Our results indicate that specific organic functionalities can be used to tune the reactivity of hybrid compounds for EUV light by introducing them in doping amounts, thus preserving the processability of the precursor material.

*The content of this chapter has been published in: L. Wu, M. Vockenhuber, Y. Ekinici and S. Castellanos, *Proc. SPIE* **2019**, 10957, 109570B. Correction: Doses in Fig. 3.2 were corrected with a factor of 1.7, because of a recalibration performed after the publication to account for the size of the pinhole used for these experiments, which was different from the standard one. The electronic supplementary information is available at <http://dare.uva.nl/en>.

3.1 Introduction

The main motivation for the introduction of inorganic resists in EUV lithography was the need for higher EUV absorption cross-sections. While the enhancement of absorptivity is indeed a major advantage of these materials compared to polymer-based chemically amplified resists (CAR), there are many other chemical features in inorganic resists that can be advantageous if properly tuned. Inorganic resists are typically based on discrete entities (molecules or nanoparticles) that can act as small voxels in the lithographic process, which is seen as favorable for the reduction of pattern roughness.¹⁻³ They are also not relying on an amplification mechanism (or at least, not one based on photoacid generators), which simplifies the system and reduces stochastic sources. In addition, inorganic resists are expected to present less electron blur due to the different scattering of electrons when the inorganic units are present in the thin film compared to polymeric materials.⁴

In most cases, the inorganic component is coated and/or stabilized by an organic component. For many of these hybrid resists, the organic shell confers the solubility properties of the material, so that, once the latter is cleaved, this leads to the formation of less soluble, cross-linked inorganic networks.⁵⁻⁷ However, some works have evidenced that the organic shell can play a more active role in the patterning mechanism.^{2,8-11} The organic moieties can also promote the formation of new bonds, especially when they have terminal double bonds that are prone to undergo radical polymerization. This phenomenon was observed in molecular organometallic resists (MORE)⁸ and in oxo clusters.^{9,10} Ober's group proposed that EUV irradiation can induce the replacement of ligands in ZrO_2 and HfO_2 nanoparticles by the sulphonic acid generated in the process, thus rendering the solubility switch.¹¹ Recently, this concept was also applied to smaller molecules based on Zn-dimers where, as a result of EUV exposure, ligands with positive charge density at their terminal positions were replaced with by ligands with terminal negative charge density, leading to a solubility switch due to a change in the molecular polarity.²

Therefore, the design of new EUV resist materials that can meet all the requirements to keep up with Moore's law demands the understanding of the role of both inorganic and organic components in these new types of hybrid resist. With this in mind, we performed a study on the effect of small variations in the organic shell of a series of molecular hybrid compounds that shared a common inorganic core. The materials of choice are metal oxo clusters (MOCs). MOCs comprise a dense multimetallic inorganic core with a fixed number of metallic atoms and bridging oxygens/hydroxide groups and a specific number of organic ligands that are responsible for the shape and stability of the inorganic core. Each organic ligand is bonded to either one or two metallic cations through a carboxylate group. An intrinsic property of such bonding is its dynamic character, meaning that, in solution, the carboxylate ligands can "walk" around the cluster¹² or that in the presence of competing chelating agents, the ligands can be exchanged by another species.¹³⁻¹⁵

In this chapter, we exploit the dynamic behavior of MOCs to generate a library

of “doped” materials. Starting with a methacrylate-based MOC as precursor material, we introduce a ligand with a particular functionality, such as extended (hetero)aromatic, fluorinated or iodinated moiety, in small ratios (*i.e.* less than 17%). We found that the sensitivity of resulting MOCs towards EUV light was much affected by the introduction of these “doping ligands”. These findings underline the contribution of the organic components in the reactivity and lithographic performance of hybrid EUV resists.

3.2 Experimental

3.2.1 Materials

Zirconium(IV) oxo hydroxy methacrylate ($\text{Zr}_6\text{O}_4(\text{OH})_4\text{Mc}_{12}$, denoted as ZrMc_{12} in this chapter), 2-(trifluoromethyl)acrylic acid (TFMAA), 3-iodopropionic acid (I-PA), 2,2'-bithiophene-5-carboxylic acid (BTA), caesium fluoride, carbazole, and 4-fluorobenzene, as well as all the solvents were purchased from Sigma-Aldrich and used as received. 4-(9H-carbazol-9-yl)benzoic acid (CBA) was synthesized as previously reported in the reference.^{16,17}

3.2.2 Ligand exchange reaction and thin film deposition

Shell-doped MOCs are prepared via ligand exchange reactions. As an example of the preparation method of the doped system, the precursor ZrMc_{12} (5 mmol) was added to a solution of TFMAA (5 mmol) and CHCl_3 (900 μL). The suspension was sonicated for 5 minutes. To the reaction mixture of ZrMc_{11}F was added 100 μL of propylene glycol methyl ether acetate (PGMEA). The reaction mixture was again sonicated for 2 minutes and filtered through a 0.2- μm syringe filter to remove any particles. The filtrate was spin-coated onto silicon substrates at 2100 rpm for 30 s and thin films were baked at 90 °C for 30 s to remove residual solvents. $\text{ZrMc}_{10}\text{F}_2$ films were deposited in the same way but using two molar equivalents of TFMAA to ZrMc_{12} . The final numbers of the fluorinated ligands in the doped organic shell of ZrMc_{11}F and $\text{ZrMc}_{10}\text{F}_2$ were determined by the atomic concentration of fluorine and zirconium in the films from X-ray photoelectron spectroscopy (XPS, see Fig. S3.1 and S3.2 in Supporting Information).

Thin films of other shell-doped MOCs were prepared in an analogue method with I-PA, BTA, and CBA and noted as ZrMc_{11}I , $\text{ZrMc}_{10}\text{I}_2$, $\text{ZrMc}_{11}\text{BTC}$, $\text{ZrMc}_{10}\text{-BTC}_2$, and $\text{ZrMc}_{10}\text{CB}_2$.

3.2.3 EUV exposure and characterization

EUV exposure was performed with the EUV interference lithography tool at the XIL-II beamline of Swiss Light Source (SLS) at the Paul Scherrer Institute (PSI). Exposed resists were developed in CHCl_3 for 30 s and dried under nitrogen without post-exposure bake. The thickness of resists at each dose was measured using a Bruker atomic force microscopy (AFM) with the ScanAsyst mode and that of

unexposed sample was determined by making a scratch and measuring. Images of line/space patterns were recorded using an FEI Verios 460 scanning electron microscopy (SEM) with a voltage of 1 kV.

3.3 Results and discussion

3.3.1 Effect of doping ligand on sensitivity

The reason to work at a “doping” level was an attempt to avoid a significant alteration in the physical properties of the original material. Mainly, we wanted to keep the solubility properties of the non-doped precursor compound in order to be able to work with similar developers and make the study more comparable. Although a certain dipole moment could be introduced by breaking the symmetry of the original ZrMc_{12} cluster, we expected that the exchange of 1 or 2 X ligands out of 12 (8% and 17%) to yield ZrMc_{11}X or $\text{ZrMc}_{10}\text{X}_2$, respectively would not dramatically change the intermolecular interactions (Fig. 3.1).

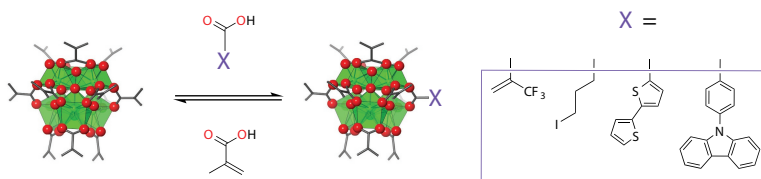


Figure 3.1: Schematic representation of the doping process of methacrylate-based MOC by ligand-exchange reaction containing a functionality X= fluorinated, iodinated, or extended aromatic system.

We therefore assume that the packing of the doped MOCs is close to that of the undoped material, given that the thin film presents a disordered arrangement of spherical molecules. This assumption allows us to estimate the densities of doped MOCs. The linear absorption coefficient α of each doped material was calculated according to the equation $\alpha = \mu \times \delta / \text{Mw}$, where μ is the sum of atomic absorption cross-sections, δ is the density of the thin film and Mw is the molecular weight (Table 3.1).¹⁸

The choice of the doping ligands followed different criteria. In the case of the halogenated ligands, the main aim was to enhance the absorption and the yield of primary photoelectrons. Both fluorine and iodine have much higher EUV photon absorption cross-sections than carbon or zirconium.¹⁹ In addition, it had been reported that iodine can emit multiple electrons per absorbed photon.²⁰ In the case of the extended aromatic fragments, two potential effects were anticipated. On the one hand, extended aromatic structures have lower band gaps than saturated carbon chains. It had been reported by Denbeaux and coauthors that a correlation had been found in chemically amplified resists between the band gap of the polymeric platform and their sensitivity.²¹ This was attributed to a likely higher secondary electron yield (more ionization events induced by the generated

photoelectrons) occurring in polymers with lower bandgaps. On the other hand, we also found that the introduction of extended aromatic structures in Ti-based oxo clusters provided them with the ability to stabilize the radical cations that result from their photoionization (see Chapter 5).¹⁵ Therefore, with the introduction of extended aromatic structures in this work, our aim was to investigate which of these two phenomena would dominate in the sensitivity of the material. That is, an increase in secondary electrons due to a lower bandgap should lead to a sensitivity enhancement. Contrarily, stable radical cations could act as quenchers in the polymerization reaction involving the terminal bonds of the methacrylate ligands, the mechanism that had been found responsible for the solubility switch in methacrylate Zr- and Hf-based metal oxo clusters.

Thin films of this series of doped materials were exposed to EUV in the XIL-II station at Paul Scherrer Institute.²² Using a multidose open frame exposure, the contrast curve for each compound was obtained. As in the case of the undoped precursor, all materials acted as negative tone resists and the same development procedure was used in all cases.

It can be observed in Fig. 3.2 that the presence of fluorine and iodine in the clusters has a positive effect on the sensitivity compared to the precursor material. This is in line with the slightly higher absorptivity of these materials. However, the trend does not follow a linear relationship with the photon absorption nor does the iodinated material show much lower doses to gel than the fluorinated material. In fact, an increase in the ratio of halogenated ligand did not seem to further increase the sensitivity. It should be noticed that in the case of the iodinated ligand, the incorporation of this particular ligand also means a decrease in the number of terminal double bonds in the organic shell. We suspect that this might be the reason for the negative effect on sensitivity in the case of the doubly doped $\text{ZrMc}_{10}\text{I}_2$. The influence on the sensitivity in the clusters doped with aromatic ligands is much more drastic. The dose-to-gel (D_0 , which is the onset where the thickness of resist is measurable) increases by one order of magnitude when a doping ratio of aromatic ligand to methacrylate of 1:11 is used and up to $40\times$ fold when the doping ratio is 2:10. The lack of proportionality between sensitivity and calculated absorptivity is thus even more evident for these compounds.

Therefore, we hypothesize that, although the absorptivity must influence, the changes in the sensitivity are strongly dependent on the contribution of new re-

Table 3.1: Calculated linear absorptivity of pristine ZrMc_{12} and doped $\text{ZrMc}_{12-n}\text{X}_n$ ($n = 1$ or 2), where X is the doping ligand. T (%) is the EUV transmittance of MOCs thin films with thickness of 30 nm and # Photons is the increase of the number of absorbed photons for such thin films in comparison to the undoped precursor.

MOC	ZrMc_{12}	ZrMc_{11}I	$\text{ZrMc}_{10}\text{I}_2$	ZrMc_{11}F	$\text{ZrMc}_{10}\text{F}_2$	$\text{ZrMc}_{11}\text{BTC}$
α (μm^{-1})	4.2	5.1	6.1	4.6	5.0	4.3
T (%)	88	86	83	87	86	88
# Photons	-	+22%	+44%	+10%	+18%	+3%

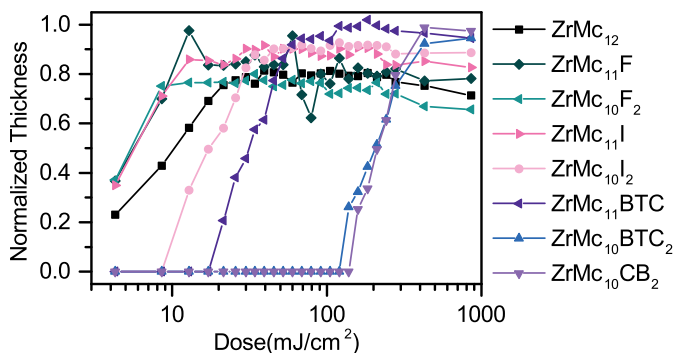


Figure 3.2: Contrast curves of ZrMc_{12} and doped Zr-based MOCs $\text{ZrMc}_{12-n}\text{X}_n$ ($n = 1$ or 2) obtained with the same development process (CHCl_3 for 30 s).

action pathways arising from the new ligands. The polarization of C–F and C–I bonds can favor the cleavage of these bonds. For instance, it is known that halogenated compounds can undergo dissociative electron attachment of the C–halogen bond.^{23,24} This new reactivity might further contribute to the solubility switch of the product, in addition to the cross-linking of the terminal double bonds in the methacrylate ligands. The drop of sensitivity for MOCs doped with extended aromatic ligands, on the other hand, could be related to the stabilization of the radical cations that are generated during the electron cascade. These species would act as hole traps, interrupting the radical or cationic polymerization of the terminal double bonds. They can also be termination points of those chain reactions, since these aromatic radical cations can uptake the electron or react with the propagating radicals and stop the propagation process. Investigations to elucidate the exact mechanisms with spectroscopic methods will be discussed in Chapters 6 and 7.

The contrast curves seem to further indicate an enhancement in the solubility contrast γ for all doped materials compared to the precursor (Fig. 3.3). This observation might be also related to the introduction of new reaction pathways parallel to (or competing with) the cross-linking reactions between methacrylate ligands, which could lead to new photoproducts that exhibited larger solubility contrast. Yet, further investigations involving solubility rates and the identification of the photoproducts are necessary to confirm and understand this effect.

After observing the effect of the aromatic extended ligands on the sensitivity of the Zr-based materials, we performed the doping on the analogous HfMc_{12} MOC. The negative effect in the sensitivity was also reproduced on this compound. This result shows the potential of the ligand doping strategy on MOCs as EUV resists. Once the positive or negative effect of a particular ligand on the sensitivity is determined, the trend can be readily transferred to MOCs based on other metals.

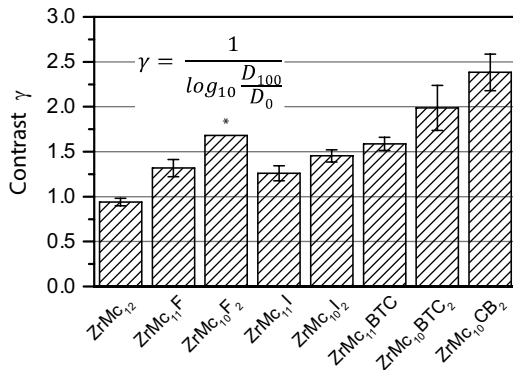


Figure 3.3: Calculated contrast for each doped Zr-MOC in comparison to ZrMc₁₂. *D₀ is estimated from linear fitting at the linear regime of the contrast curve. D₁₀₀ is the minimum dose at which the maximum thickness of converted material was found.

3.3.2 Effect of doping ligand on dense-lines and contact-holes/pillars printing

Dense line patterning experiments by EUV interference lithography were performed on the fluorinated doped material ZrMc₁₁F. No optimization of the development process was carried out for this preliminary tests on the lithographic performance. Instead, the same developing conditions as for open frame experiments were used in order to compare with previous results obtained on the ZrMc₁₂. Smaller pitches could be resolved for the doped material compared to the undoped ZrMc₁₂ material²⁵ (Fig. 3.4).

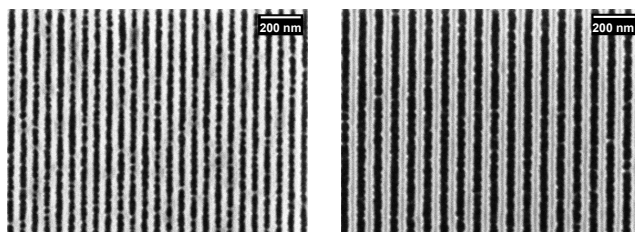


Figure 3.4: SEM images of dense line patterns on ZrMc₁₁F. Left: line width 30 nm (pitch 60 nm), dose 36.4 mJ/cm². Right: line width 40 nm (pitch 80 nm), dose 38.0 mJ/cm².

*Errors were calculated based on the standard error of the slope and intercept from linear fitting in contrast curves according to rules of error propagation. The errors from D₁₀₀ were omitted. The contrast curve of ZrMc₁₀F₂ has only two data points in the slope and therefore the standard error is not available.

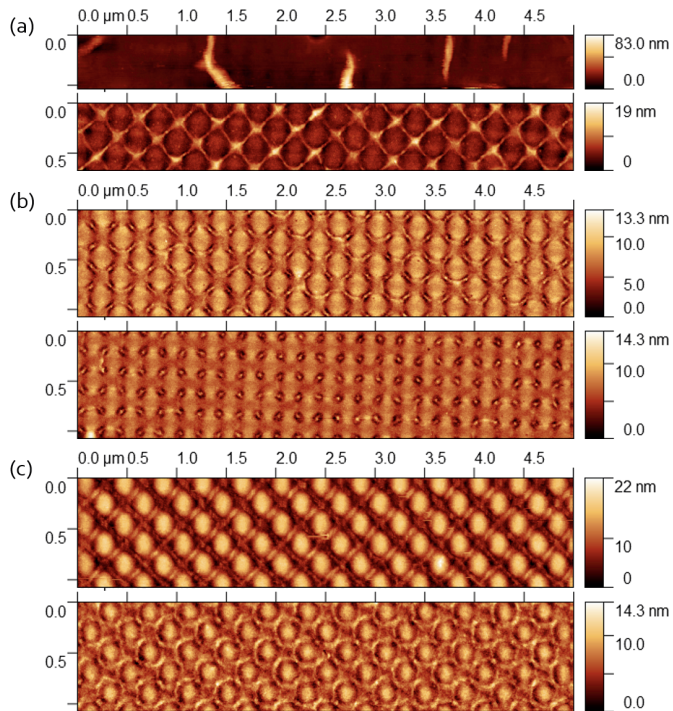


Figure 3.5: AFM images showing the doping effect in contact-pillars/holes. (a) ZrMc_{12} 1.5 mJ/cm^2 , (b) ZrMc_{11}F 1.5 mJ/cm^2 , and (c) $\text{ZrMc}_{10}\text{CB}_2$ 15 mJ/cm^2 .

The effect of the fluorinated doping ligand as well as of the extended aromatic ligand was also investigated for the printing of pillars and holes (Fig. 3.5). As for the dense line patterns, the development step was not optimized for these preliminary tests and chloroform was used as the developer. The enhanced contrast of the doped materials compared to the precursor material seemed to enable the formation of this type of pattern. Pillars were resolved clearly for both the materials, although they presented scumming. In addition, the positive (for ZrMc_{11}F) and negative (for $\text{ZrMc}_{11}\text{CB}_2$) influence of the doping ligand on the sensitivity became evident in the dose-to-size of each material (1.5 mJ/cm^2 and 15 mJ/cm^2 , respectively). The higher doses for $\text{ZrMc}_{11}\text{CB}_2$ might account for the better quality for the pillar patterning.

3.4 Conclusion

The doping of the methacrylate shell in Zr-based metal oxo clusters (MOCs) with carboxylate ligands featuring fluorine, iodine, or extended aromatic moieties has an important impact in the sensitivity of these hybrid molecular materials that can act as negative tone EUV resists. Ligands bearing fluorine or iodine had a

positive effect on the sensitivity. Yet, this enhancement is not proportional to the estimated increase in absorptivity and thus might be the result of other (chemical) factors that add to photon absorption, such as electron-induced bond dissociation reactions. Contrarily, the incorporation of extended aromatic structures has a detrimental effect on the sensitivity of the material, which is further stressed when more doping ligands are present in the cluster. We suspect that the ability of the extended aromatic structures to stabilize radical cations might interfere with the cross-linking of the methacrylate terminal double bonds, which is the mechanism that renders the solubility change in this type of resists. Although further investigations to reveal the mechanistic explanations of these effects will be discussed in later chapters, these results already highlight the great potential of MOCs as platforms to understand EUV chemistry and to identify which structural parameters can be used to tune lithographic performance. The synthetic versatility of MOCs, arising from the dynamic behavior of the carboxylate ligands, allows to easily attain a different combination of the two components (metals and ligands) of these hybrid resists. In this fashion, both the absorptivity (and likely the photoelectron yield) can be tuned by means of the metal content whereas the reactivity of the electron cascade can be modified by the organic shell.

Bibliography

- [1] A. Lio, *Proc. SPIE*, 2016, **9776**, 97760V.
- [2] H. Xu, K. Sakai, K. Kasahara, V. Kosma, K. Yang, H. C. Herbol, J. Odent, P. Clancy, E. P. Giannelis and C. K. Ober, *Chem. Mater.*, 2018, **30**, 4124–4133.
- [3] L. Li, X. Liu, S. Pal, S. Wang, C. K. Ober and E. P. Giannelis, *Chem. Soc. Rev.*, 2017, **46**, 4855–4866.
- [4] A. Vaglio Pret, T. Graves, D. Blankenship and J. J. Biafore, *Proc. SPIE*, 2017, **10146**, 1014609.
- [5] W. D. Hinsberg and S. Meyers, *Proc. SPIE*, 2017, **10146**, 1014604.
- [6] B. Cardineau, R. Del Re, H. Al-Mashat, M. Marnell, M. Vockenhuber, Y. Ekinici, C. Sarma, M. Neisser, D. A. Freedman and R. L. Brainard, *Proc. SPIE*, 2014, **9051**, 90511B.
- [7] Y. Zhang, J. Haitjema, X. Liu, F. Johansson, A. Lindblad, S. Castellanos, N. Ottosson and A. M. Brouwer, *J. Micro/Nanolithogr., MEMS, MOEMS*, 2017, **16**, 023510.
- [8] R. Del Re, M. Sortland, J. Passarelli, B. Cardineau, Y. Ekinici, M. Vockenhuber, M. Neisser, D. A. Freedman and R. L. Brainard, *Proc. SPIE*, 2015, **9422**, 942221.
- [9] S. Castellanos, L. Wu, M. Baljovic, G. Portale, D. Kazazis, M. Vockenhuber, Y. Ekinici and T. Jung, *Proc. SPIE*, 2018, **10583**, 105830A.
- [10] E. C. Mattson, Y. Cabrera, S. M. Rupich, Y. Wang, K. A. Oyekan, T. J. Mustard, M. D. Halls, H. A. Bechtel, M. C. Martin and Y. J. Chabal, *Chem. Mater.*, 2018, **30**, 6192–6206.
- [11] M. Kryask, M. Trikeriotis, C. Ouyang, S. Chakrabarty, E. P. Giannelis and C. K. Ober, *J. Photopolym. Sci. Technol.*, 2013, **26**, 659–664.
- [12] P. Walther, M. Puchberger, F. R. Kogler, K. Schwarz and U. Schubert, *Phys. Chem. Chem. Phys.*, 2009, **11**, 3640–3647.
- [13] T. Frot, S. Cochet, G. Laurent, C. Sassoie, M. Popall, C. Sanchez and L. Rozes, *Eur. J. Inorg. Chem.*, 2010, 5650–5659.
- [14] J. Kreutzer, M. Puchberger, C. Artner and U. Schubert, *Eur. J. Inorg. Chem.*, 2015, **2015**, 2145–2151.
- [15] L. Wu, M. Tiekink, A. Giuliani, L. Nahon and S. Castellanos, *J. Mater. Chem. C*, 2019, **7**, 33–37.
- [16] G.-S. Liou, S.-H. Hsiao, N.-K. Huang and Y.-L. Yang, *Macromolecules*, 2006, **39**, 5337–5346.
- [17] S.-H. Hsiao and Y.-T. Chiu, *RSC Adv.*, 2015, **5**, 90941–90951.
- [18] R. Fallica, J. Haitjema, L. Wu, S. Castellanos, , A. M. Brouwer and Y. Ekinici, *J. Micro/Nanolithogr., MEMS, MOEMS*, 2018, **17**, 023505.
- [19] B. L. Henke, E. M. Gullikson and J. C. Davis, *At. Data Nucl. Data Tables*, 1993, **54**, 181–342.

-
- [20] D. F. Ogletree, *X-Rays, Electrons and Lithography: Fundamental Processes in Molecular Radiation Chemistry*, presented in part at the 10th International Workshop on EUV Lithography, Berkely, June, 2017.
- [21] S. Grzeskowiak, J. Kaminsky, S. Gibbons, M. Murphy, J. Chandonait, R. L. Brainard and G. Denbeaux, *Proc. SPIE*, 2018, **10586**, 105860D.
- [22] N. Mojarad, J. Gobrecht and Y. Ekinici, *Microelectron. Eng.*, 2015, **143**, 55–63.
- [23] S. G. Rosenberg, M. Barclay and D. H. Fairbrother, *ACS Appl. Mater. Interfaces*, 2014, **6**, 8590–8601.
- [24] M. Mahmoodi-Darian, S. E. Huber, A. Mauracher, M. Probst, S. Deniff, P. Scheier and T. D. Märk, *J. Chem. Phys.*, 2018, **148**, 074301.
- [25] L. Wu, M. Baljozovic, G. Portale, D. Kazazis, M. Vockenhuber, T. Jung, Y. Ekinici and S. Castellanos, *J. Micro/Nanolithogr., MEMS, MOEMS*, 2019, **18**, 013504.

Hybrid EUV resists with mixed organic shells: a simple preparation method*

Abstract

Metal-containing molecular hybrid compounds, such as metal oxo clusters (MOCs), are promising resist materials for extreme ultraviolet (EUV) lithography. The solubility, processability, and reactivity towards EUV photons in these compounds are mostly determined by the composition of their organic shells. Therefore, gaining molecular control on the composition of the shell is crucial to tune their lithographic performance in terms of sensitivity, resolution, and line-edge roughness. In this chapter, a new method to prepare MOCs that feature two types of carboxylate ligands is presented. In this method, amine-functionalized resins are used for the purification step. By using this protocol, Ti- and Zr-based MOCs with mixed-ligands organic shells were synthesized. The new compounds showed clear differences in the processability and sensitivity as EUV resists compared to their analogues featuring only one type of ligand. The results validate this new synthetic approach for the preparation of custom-made EUV resists towards better lithographic performance.

*The content of this chapter has been published in: L. Wu, J. Liu, M. Vockenhuber, Y. Ekinici and S. Castellanos, *Eur. J. Inorg. Chem.* **2019**, 2019, 4136-4141. Supporting information is available for free via the Internet at <https://doi.org/10.1002/ejic.201900745>.

4.1 Introduction

The roadmap of the semiconductor industry demands the continuous miniaturization of the electronic components in computer chips. To fulfill this goal, a new nanolithography technology is introduced into the market: extreme ultraviolet lithography (EUVL).¹⁻³ This technique evolved from the traditional optical photolithography, where a pattern is written with light shining on a photosensitive material known as a resist. The illuminated areas undergo photochemical reactions that lead to changes in the solubility properties of the material. This allows for the selective dissolution of either the exposed or the unexposed areas with a suitable developer. One of the main differences of EUVL with respect to previous generations of photolithography is the wavelength used for the pattern projection. EUVL employs 13.5 nm in order to overcome the resolution limits of the deep UV technology, which employs 193 nm wavelength. The main consequence is that absorption of light in this energy regime (soft X-ray) leads to photoionization instead of resonant electronic transitions and, therefore, the chemical reactions are mainly performed by the secondary electrons generated upon irradiation. In addition, the probability of absorption of EUV photons is mainly determined by the elemental composition of the resist,^{4,5} rather than the selection rules of classical photochemistry, where the characteristics of the frontier molecular orbitals can be used to predict the absorption probability.

Since conventional resists based on light elements exhibit low EUV absorptivity, new resist materials that incorporate elements with high EUV photon absorption cross-section, such as metallic elements, are attracting much interest in the EUVL field.^{3,6} Yet, while the inorganic elements in these materials are considered responsible for the photon capture, the mechanism that leads to the solubility change is mainly determined by the reactivity of their organic components.^{7,8}

Metal oxo clusters (MOCs) are molecular hybrid compounds with inorganic core-organic shell structures,^{9,10} which are ideal platforms as EUV resist.^{7,11} They have well-defined inorganic cores and organic shells and, as a result of their molecular nature, they are small and have homogeneous (monodisperse) sizes by definition. These aspects contribute to the reduction of stochastic sources that are partly responsible for the “noise” in the nanopatterns, that is, irregularities in the features’ edges (measured as line-edge roughness) and/or widths (measured as line-width roughness).¹²

In Chapter 2, we showed that Zr-based oxo cluster featuring methacrylate ligands (Fig. 4.1) are promising EUV photoresists.⁷ This material is comprised of an hexametalic oxocore and twelve ligands in bridging and chelating coordination modes¹³ ($\text{Zr}_6\text{O}_4(\text{OH})_4\text{M}_{12}$, denoted as Zr_6M_{12} in this chapter). The change in solubility that this material undergoes upon EUV irradiation mainly originates from the cross-linking of the methacrylate ligands. Yet, the lithographic performance of Ti-based oxo cluster could not be tested due to the poor solubility of this material, which hindered its deposition as a thin film.¹⁴ This compound consists of an octameric ring of metal atoms bridged by μ_2 -O oxygens and 16 methacrylate ligands ($\text{Ti}_8\text{O}_8\text{M}_{16}$, denoted as Ti_8M_{16}).¹⁵

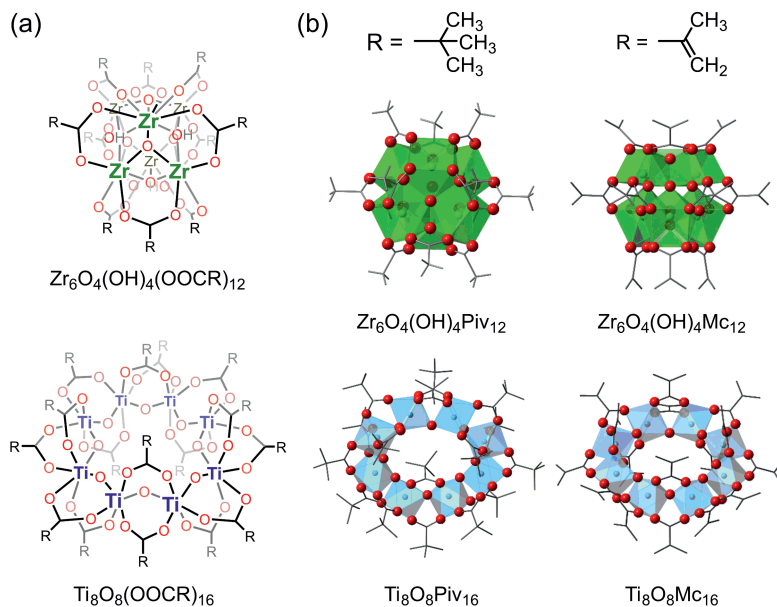


Figure 4.1: (a) General molecular formulae of the hexameric Zr-based and the octameric Ti-based oxo clusters with carboxylate ligands. (b) Molecular structure of the clusters as resolved from X-ray crystalline diffraction.^{13,15–17} The coloured polyhedra represent the coordination geometry of the metal, the red spheres the oxygen atoms and the grey bars the carbon backbone of the pivalate or methacrylate ligands.

The analogous material featuring pivalate ligands (Ti_8Piv_{16})^{16,18}, renders better solubility in organic solvents like chloroform, toluene, and tetrahydrofuran. However, the films obtained by spin-coating are of bad quality due to their poor wettability on the Si-substrate, even when the Si surface is functionalized to be hydrophobic.

A characteristic of MOCs that makes them particularly interesting as EUV resists is their synthetic versatility. The latter arises from the dynamic bonding between the metals in the oxo-core and the carboxylate ligands in the shell, which allows for easy exchange of the organic ligands^{16,19–22} and thus a simple way of modifying their composition. This offers a much advantageous tool to study the chemistry that different functionalities can undergo upon EUV irradiation and investigate their impact on the lithographic performance of the material.^{23,24} Such need of fundamental understanding on the EUV-induced chemistry is a pressing issue in the field of EUV lithography, since the success of this new technology is partly depending on the sensitivity, resolution limit, and defect density that the photoresist material can yield in the patterning process.

Despite the simplicity of ligand exchange reactions between ligands that have the same coordination geometries (binding multiplicity and angle), the isolation

and purification of the resulting MOCs with mixed shells is not straightforward. The most common method of isolation of MOCs is crystallization.^{16,20} However, purification of MOCs designed for lithographic applications by means of crystallization is not optimal for two main reasons. First, as part of the lithographic process, the material must be deposited as homogeneous thin films of a few nanometers of thickness (20–30 nm) using spin-coating. This means that the MOCs must be soluble in organic solvents and able to provide homogeneous amorphous films. Yet, structural characteristics that enhance solubility and amorphous solid phases typically do not favour packing in crystalline arrangements. Second, as explained above, it is highly desired that several functionalities can be incorporated simultaneously in the MOCs (mixed-shell) so that the chemistry that yields the solubility change of the material can be finely tuned. However, crystallization becomes extremely challenging when a distribution of oxocluster molecules with mixed-shell compositions is formed during ligand exchange reactions. In fact, to the best of our knowledge, isolation of metal oxo clusters resulting from ligand exchange on the Zr₆ and Ti₈ oxo cores by crystallization has only been reported for fully exchanged organic shells,¹⁶ whereas oxoclusters with mixed-shells could only be isolated by crystallization when crystals are formed during the condensation reaction between the metal alkoxide precursor and a mixture of carboxylic acids.²⁰ Furthermore, in the latter case, accessing all ratios of the two ligands would require a broad screening of reaction conditions.

In this chapter, we conceived a preparation method of mixed-shell Zr- and Ti-MOCs based on a purification step with resins functionalized with basic amine groups. Having two different ligands in the organic shell of these compounds had two main purposes. In the case of Ti-MOCs, we aimed at introducing ligands that facilitate their dissolution together with ligands that favour the formation of thin films and also enable the cross-linking reaction as a means for patterning. In the case of Zr-MOCs, the mixed-ligand shell enables studying the effect of decreasing the number of terminal double bonds in the organic shell. Once the mixed-shell were attained by ligand exchange reactions, the basic resins were used to extract the excess of carboxylic acids. This method allows for the easy preparation of metal oxo clusters with complex organic shell composition and proves to be a good synthetic tool that allows modulating the EUV sensitivity of this type of material by tuning their molecular structure.

4.2 Experimental

General remarks. Polystyrene-resins functionalized with tertiary amines were purchased from Sigma-Aldrich (dimethylaminomethyl-polystyrene, catalogue number 39205; piperidine, polymer-bound, catalogue number 494615).

¹H NMR experiments were performed in a Bruker Avance 300 MHz spectrometer, FTIR-ATR experiments of bulk samples were performed in a Bruker ALPHA-II FTIR spectrometer. FTIR spectra of spin-coated thin films were recorded with a Bruker Vertex 80v spectrometer. TGA was performed using NETZSCH thermo-

gravimetric analyzer in an Al_2O_3 crucible and heating was performed from 35 °C to 800 °C at 10 K/min in an 80:20 N_2/O_2 atmosphere. Thickness measurements were performed using a Bruker atomic force microscopy (AFM) with the ScanAsyst mode.

Synthesis of $\text{Ti}_8\text{Piv}_{16}$ and $\text{Zr}_6\text{Piv}_{12}$. $\text{Ti}_8\text{Piv}_{16}$ was synthesized as described in reference¹⁹. $\text{Zr}_6\text{Piv}_{12}$ was prepared with an analogous method. Pivalic acid (2.0 g, 20 mmol) was added to zirconium propoxide (70 wt.% in 1-propanol, 1.0 mL, 2.3 mmol). The mixture was placed in an autoclave and heated up at 80 °C for 24 h. The reaction gave white crystals that were filtered off and washed with diethyl ether to give the insoluble cluster $\text{Zr}_6\text{Piv}_{12}$ (540 mg, 76%), as identified from powder X-ray diffraction (see Figure S1 in Supporting Information) and IR, which gave identical features as compared to the ones reported in the literature for the same compound.¹⁷ Thermogravimetric analysis (TGA) was also in agreement with the expected composition (calculated ZrO_2 residue 39%, found 32%, see Figure S4 in Supporting Information).

Equilibrium adsorption of resins. To the carboxylic acid (0.1 mmol) in deuterated chloroform (1 mL) solution was added the dimethylaminomethyl or piperidine-functionalized resin (0.1 mmol of amine content estimated from N content according to the supplier). The solution was stirred for 30 min. The resin was then filtered out of the solution. To 0.75 mL of the solution, toluene or pyridine (10 μL) was added as a standard for quantification of acid left in solution by ^1H NMR (300 MHz) measurement.

Determination of ligand ratio after ligand exchange reaction and purification with resin. $\text{Ti}_8\text{Piv}_{16}$ (10 mg) were dissolved in CDCl_3 (1 mL) and the carboxylic ligand was added in molar ratios of 1:12, 1:16, 1:20 or 1:36. The reaction mixture was stirred for 30 min. The resin was added to the reaction in a 1:1 molar ratio of carboxylic acid/amine in resin (based on N content of the resin) and the mixture was stirred for 30 min. The solution was filtered and analyzed by ^1H NMR. The composition of the organic shell was determined by the signal ratio between the bonded ligands.

Scaled-up synthesis of $\text{Ti}_8\text{Piv}_{10}\text{Mc}_6$ and $\text{Zr}_6\text{Piv}_4\text{Mc}_8$. $\text{Ti}_8\text{Piv}_{16}$ and $\text{Zr}_6\text{Piv}_{12}$ (300 mg) were dissolved or suspended in chloroform (20 mL) respectively. MAA was added in molar ratios of 1:16 or 1:36. The reaction mixture was stirred for 30 min. Resin was added in a ratio of amine to carboxylic ligand ratio of 1:1 (based on N content of the resin) and the reaction mixture was stirred for 30 min. The resin was filtered out and the solvent was evaporated. The product was analyzed with ^1H NMR (see in Supporting Information) and IR spectrometer.

Spin coating of mixed-ligand MOCs. $\text{Ti}_8\text{Piv}_{10}\text{Mc}_6$ or $\text{Zr}_6\text{Piv}_4\text{Mc}_8$ was dissolved in toluene (10 mg/mL). The solution was filtered with a 0.2- μm filter and deposited onto a silicon substrate by spin-coating (2400 rpm, 30 s, 2000 rpm/s acceleration for $\text{Ti}_8\text{Piv}_{10}\text{Mc}_6$ and 3000 rpm/s for $\text{Zr}_6\text{Piv}_4\text{Mc}_8$).

Exposure in XIL-II beamline. EUV open-frame exposure was performed at the XIL-II beamline of Swiss Light Source (SLS) at the PSI. Doses were varied from 3.75 to 756 mJ/cm^2 . Toluene and chloroform were tested as developers for 20 s and 15 s respectively for the exposed resists.

4.3 Results and discussion

4.3.1 Equilibrium adsorption of resins

Resins that are functionalized with tertiary amines have been used in the past to remove carboxylic acids from organic solvents.^{25,26} In the present work, the resins that were selected for the purification step after ligand exchange reaction were polystyrene (PS) resins functionalized with tertiary amines, PS-N-piperidine (denoted as PIP) and PS-N-dimethylamine (denoted as DMA). Bulky amines were chosen to avoid any competition with the carboxylate ligand in the coordination with the metals of the MOC inorganic core. The affinity of these two basic resins towards five different carboxylic acids (pivalic, methacrylic, propionic, butyric, and isobutyric acid) that are of interest to enhance solubility properties and film formation capability of MOCs was evaluated by means of ¹H NMR. To do so, the change of concentration of the acid in a solution of deuterated chloroform after adding the corresponding resin (1:1 molar ratio of amine on resin/acid) was used to calculate the equilibrium adsorption, q_e ,^{27,28} as:

$$q_e = (c_0 - c_e)/m \times V$$

where c_0 and c_e are the initial concentration and the concentration in equilibrium in mg/L, m is the mass of resin in g and V is the volume of the suspension in L (Fig. 4.2).

In all cases, the resin functionalized with piperidine showed stronger affinity towards all carboxylic acids and in particular towards methacrylic acid. On the other hand, the carboxylic acid with the bulkier backbone, pivalic acid (Piv), appeared to adsorb more poorly on both resins.

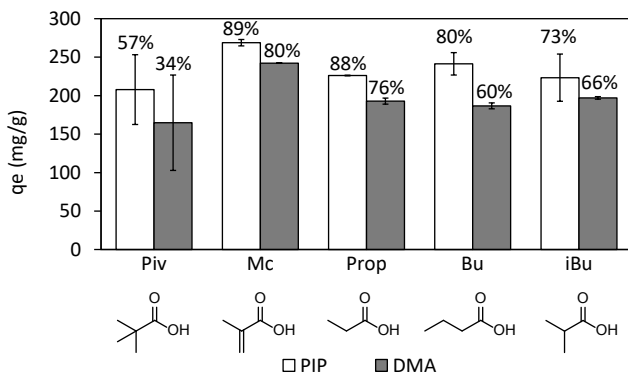


Figure 4.2: Equilibrium adsorption (q_e) measured for dimethylaminomethyl- (DMA) and piperidine-functionalized (PIP) resins and five different carboxylic acids. The percent of acid adsorbed by each resin is indicated on top of the bar. All reactions were performed using a 1:1 molar ratio of amine on the resin to carboxylic acid.

4.3.2 Ligand ratios in mixed organic shells

The use of resins for the purification process was first tested on Ti-oxo clusters on a small scale and monitored by ^1H NMR. $\text{Ti}_8\text{Piv}_{16}$ was used as starting material and ligand exchange reactions with different molar ratios of MOC to methacrylic acid (1:16 and 1:20) were performed on this compound in deuterated chloroform. After that, the resulting solution was treated with basic resin, the resin was filtered out, and the composition of the filtered solution was newly determined (Fig. 4.3). This last step was realised twice to monitor how the second cycle of resin treatment could further remove the free carboxylic acids.

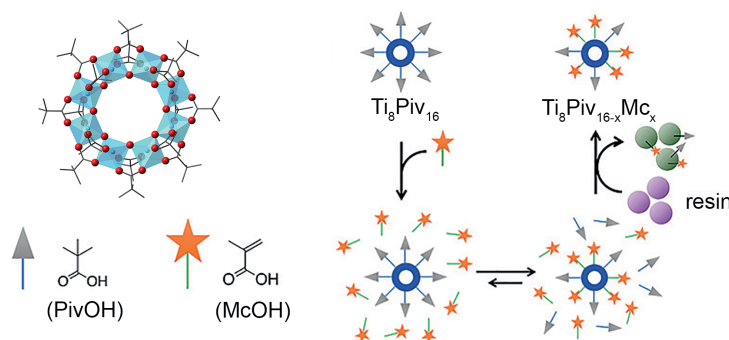


Figure 4.3: Scheme showing the steps of the new protocol for the preparation of mixed-ligand metal oxo clusters. The pristine oxo cluster with pivalate ligands $\text{Ti}_8\text{Piv}_{16}$ is dissolved in a solution with methacrylic acid and ligand exchange occurs. The amine-functionalized resin is added and the non-coordinated carboxylic acids are adsorbed on it and removed by filtration.

The chelation dynamics of the carboxylate ligands on this MOC are slow enough at room temperature to allow to distinguish the protons of ligands that are bonded to the metals from the ones of the acids that are non-bonded and free in the deuterated chloroform solution (Table 4.1). The average ratio of pivalate/methacrylate ligand in the Ti-MOC that resulted from these exchange reactions was calculated from the peak areas in the ^1H NMR spectra (Fig. 4.4).

When stoichiometric amounts of methacrylic acid were added to $\text{Ti}_8\text{Piv}_{16}$, an

Table 4.1: ^1H NMR chemical shifts of carboxylic acids and carboxylate ligands in the solution mixture of the ligand exchange reactions of titanium oxo clusters in CDCl_3 .

^1H NMR chemical shifts (ppm)		Free acid	Coordinated ligand
Pivalic acid/pivalate	$-\text{CH}_3$	1.24	1.16, 1.19
Methacrylic acid/methacrylate	$-\text{CH}_3$	1.95	1.86, 1.92
	$=\text{CH}_2$	5.68, 6.24	5.49, 5.55, 6.19, 6.21

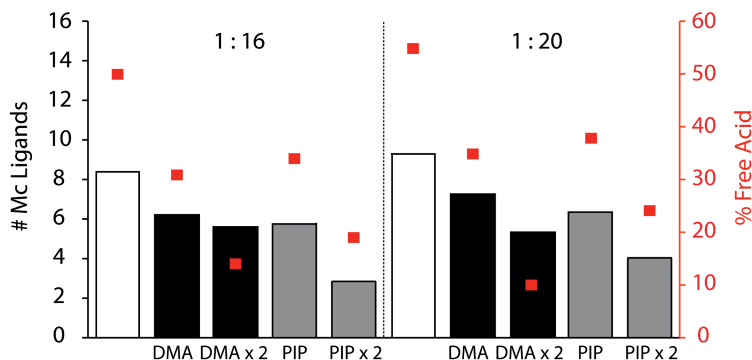


Figure 4.4: Columns: number of methacrylate ligands (x) incorporated in $\text{Ti}_8\text{Piv}_{16-x}\text{Mc}_x$ after ligand exchange reaction (white) and after treatment with one or two cycles ($\times 2$) of DMA (black) or PIP (grey) resins. Red squares: percent of free acid in the solution over the total amount of carboxylate ligands and carboxylic acids.

oxo cluster with almost 1:1 ratio of methacrylate/pivalate ligands was obtained, *i.e.* $\text{Ti}_8\text{Piv}_8\text{Mc}_8$. The average amount of methacrylate ligands in the shell was increased by increasing the molar ratio of methacrylate acid in the reaction mixture (Fig. 4.4, white columns). After treating the mixtures with each basic resin (DMA and PIP) in a 1:1 carboxylic acid/amine molar ratio (amine concentration estimated from the nitrogen content specified by the commercial provider), the percent of non-coordinated carboxylic acids decreased from 50% to 14% in the 1:16 MOC/methacrylic reaction, and from 55% to 10% in the 1:20 reaction after two resin treatment cycles (red squares in Fig. 4.4). However, the ratio of the methacrylate ligand in the oxocluster also decreased. This effect is stronger in the case of the PIP resin which made the content of methacrylate ligands in the MOC shell decrease from 8 to a minimum of 3 (1:16 ratio) and from 9 to a minimum of 4 (1:20 ratio) after the resins treatment. The results are in line with the higher affinity of both resins towards methacrylic acid compared to pivalic acid previously observed. Nevertheless, in all cases, Ti-MOCs with a binary composition in the organic shell and a reduced amount of free acids were obtained.

The approach was scaled up and utilised to prepare Ti-based MOCs and Zr-based MOCs with mixed shells that contain both methacrylate and pivalate ligands. DMA-resin was used since it reverted the introduction of methacrylate to a less extent than the PIP-resin (Fig. 4.5).



Figure 4.5: Scheme of ligand exchange reactions followed by resin purification.

For the ligand exchange reaction with $\text{Ti}_8\text{Piv}_{16}$, a 1:16 MOC/acid molar ratio was employed. In this experiment, the solution treated with DMA-resin (one cycle only) yielded the same ratio observed in the NMR experiment (Piv/Mc 10:6). Yet, the number of free acids was even lower than the one detected in the NMR studies (*ca.* 18% of free acid) thus yielding a product with an average formula of $\text{Ti}_8\text{Piv}_{10}\text{Mc}_6 \cdot 2\text{PivOH} \cdot 1\text{McOH}$. We assume that the evaporation of the solvent at reduced pressure after the resin treatment contributed to reducing the amount of free acid. Characterization of this compound by IR spectroscopy displayed a mixture of characteristic peaks of the MOCs with pure pivalate ($\text{Ti}_8\text{Piv}_{16}$) and pure methacrylate ($\text{Ti}_8\text{Mc}_{16}$) shells (Fig. 4.6). In addition, peaks associated with the non-coordinated free carboxylic acid (C=O stretching at 1700 cm^{-1} and broad-band corresponding to O-H stretching in the $2400\text{--}3600\text{ cm}^{-1}$ range) were also present.

In the case of the Zr-based cluster, our aim was to investigate how the incorporation of a small number of pivalate ligands in a methacrylate rich organic shell would affect the cross-linking mechanism induced by EUV light compared to previously studied $\text{Zr}_6\text{Mc}_{12}$ photoresist. For this reason, a higher ratio of methacrylic

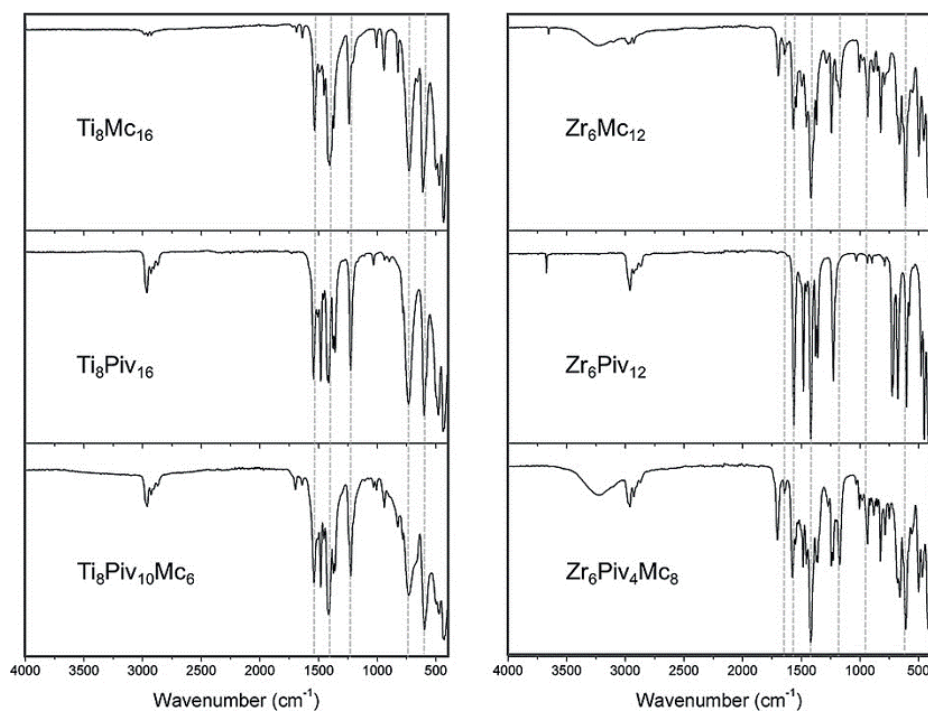


Figure 4.6: IR spectra of the products of the scaled-up ligand exchange reactions after treatment with DMA and isolation of the cluster as a powder by means of reduced pressure solvent evaporation.

acid was used for the ligand exchange reaction on $\text{Zr}_6\text{Piv}_{12}$ and the resin treatment was applied only in one cycle. In contrast to the case of the Ti-based pivalate oxoclusters, the $\text{Zr}_6\text{Piv}_{12}$ cluster is originally not soluble in chloroform. However, when this compound is suspended in chloroform in the presence of methacrylic acid, the incorporation of the methacrylate ligands in the clusters by means of ligand exchange reactions leads to the dissolution of the mixed-shell compound. The ^1H NMR spectrum after the reaction revealed that a cluster with a 4:8 Piv/Mc ratio was obtained (see Supporting Information). Yet, the dynamics of exchange between free acids and bonded acid are too fast to determine the content of free acid for this product by ^1H NMR. Nevertheless, and as in the case of the Ti-based counterpart, the IR displayed peaks characteristic for $\text{Zr}_6\text{Piv}_{12}$ and $\text{Zr}_6\text{Mc}_{12}$ (synthesized according to the literature) as well as the presence of free acids by the broad O–H stretching band and the C=O stretching peak, as in the Ti-MOC (Fig. 4.6). The average composition of the final product is thus estimated as $\text{Zr}_6\text{Piv}_4\text{Mc}_8$ from NMR experiments.

4.3.3 Metal oxo clusters with mixed organic shells as EUV resists

The isolated products $\text{Ti}_6\text{Piv}_{10}\text{Mc}_6$ and $\text{Zr}_6\text{Piv}_4\text{Mc}_8$ were tested as EUV resists. The first noticeable effect of providing the titanium oxo cluster with a mixed organic shell was that it enabled its deposition as a thin film from solution by spin-coating, in contrast to the case of the analogous compounds with only pivalate or only methacrylate ligands. The sensitivity to extreme ultraviolet light of the materials was evaluated using synchrotron radiation at the EUV interference lithography tool (XIL-II) at Paul Scherrer Institute (PSI).²⁹ This property is defined as the minimum dose of EUV light necessary to induce a chemical change that leads to a change in the solubility of the compound and is determined by means of a contrast curve. That is, the extent of the chemical changes induced by EUV light can be indirectly measured by the differences in the solubility rate of the material in a specific solvent as a function of dose. For negative tone resists, such as the ones studied in the present work, the solubility rate decreases with the EUV exposure dose. Therefore, the amount of material left on the substrate, measured as thickness, for a given development time increases with the dose, which yields the aforementioned contrast curve plot (Fig. 4.7).

Our experiments showed that the titanium oxo cluster with mixed-ligand organic shell $\text{Ti}_8\text{Piv}_{10}\text{Mc}_6$ acted as a negative-tone EUV resist when toluene was used as the developer (Fig. 4.7). In the case of the zirconium oxo cluster, chloroform was used as a developer to compare with previous results obtained for the analogous material with only methacrylate ligands ($\text{Zr}_6\text{Mc}_{12}$). It was observed that the sensitivity of the mixed-shell compound $\text{Zr}_6\text{Piv}_4\text{Mc}_8$ was lower than the one of $\text{Zr}_6\text{Mc}_{12}$, that is, a higher dose is required to induce a solubility switch in the mixed-shell oxo cluster. This observation is in agreement with the lower number of cross-linkable terminal double bonds of $\text{Zr}_6\text{Piv}_4\text{Mc}_8$ compared to the previously studied $\text{Zr}_6\text{Mc}_{12}$. That is, the radiation-induced cross-linking of terminal double

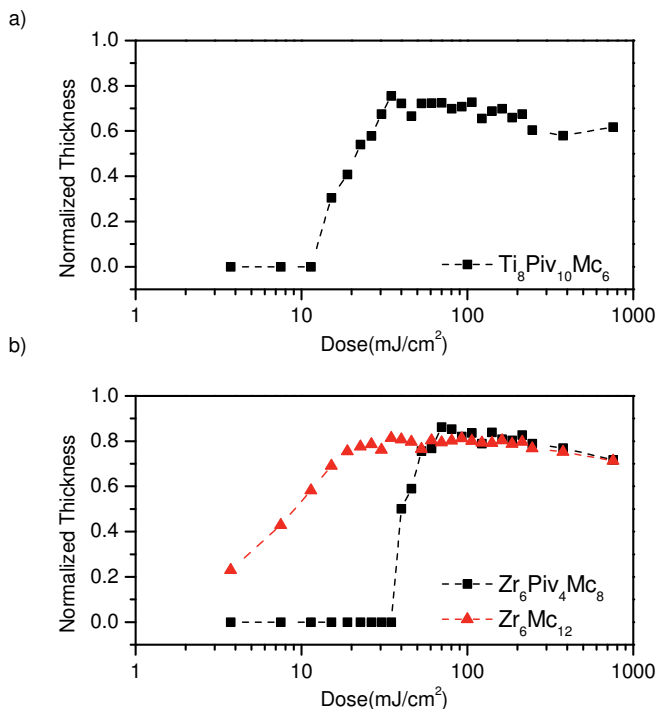


Figure 4.7: Contrast curves of (a) $\text{Ti}_8\text{Piv}_{10}\text{Mc}_6$ (original thickness $d_0 = 17$ nm) using toluene for development, (b) $\text{Zr}_6\text{Mc}_{12}$ ($d_0 = 24$ nm), and $\text{Zr}_6\text{Piv}_4\text{Mc}_8$ ($d_0 = 24$ nm) using chloroform as the developer.

bonds is less likely to occur in clusters with a lower ratio of methacrylate ligands. Therefore, the extent of chemical change that leads to a change in solubility rate requires more photons in the case of the mixed-ligand cluster.

4.4 Conclusion

Metal oxo clusters based on Ti and Zr featuring mixed carboxylate organic shells can be easily prepared and isolated by means of ligand exchange reactions followed by a basic resin treatment to remove the exceeding acid molecules. These methods allow incorporating two types of carboxylate ligands in different ratios avoiding a crystallization step. This protocol proved to be a useful tool for the modification of the lithographic performance of metal oxo clusters that act as extreme ultraviolet photoresist. In particular, the introduction of pivalate and methacrylate ligands in Ti-octamer ($\text{Ti}_8\text{Piv}_{10}\text{Mc}_6$) enables its deposition in thin films and its utilization as a negative-tone resist. On the other hand, the presence of these two ligands in Zr-hexamer oxoclusters ($\text{Zr}_6\text{Piv}_4\text{Mc}_8$) led to the decrease in sensitivity of the material compared to the parent compound with only methacrylate ligands. This

result is in line with the lower number of terminal units that can cross-link upon light exposure, which yields slower cross-linking kinetics and thus require higher photon doses for a full transformation into an insoluble network. Our work proves that the processability and the reactivity of this type of materials can be finely tuned by means of this new synthetic protocol and thus offers a versatile tool for the preparation of future extreme ultraviolet resist materials for nanolithography applications.

Bibliography

- [1] R. A. Lawson and A. P. Robinson, *Frontiers of Nanoscience*, Elsevier, 2016, vol. 11, pp. 1–90.
- [2] P. D. Ashby, D. L. Olynick, D. F. Ogletree and P. P. Naulleau, *Adv. Mater.*, 2015, **27**, 5813–5819.
- [3] L. Li, X. Liu, S. Pal, S. Wang, C. K. Ober and E. P. Giannelis, *Chem. Soc. Rev.*, 2017, **46**, 4855–4866.
- [4] R. Fallica, J. Haitjema, L. Wu, S. Castellanos, , A. M. Brouwer and Y. Ekinici, *J. Micro/Nanolithogr., MEMS, MOEMS*, 2018, **17**, 023505.
- [5] R. Fallica, J. K. Stowers, A. Grenville, A. Frommhold, A. P. G. Robinson and Y. Ekinici, *Proc. SPIE*, 2016, **9776**, 977612.
- [6] H. Xu, V. Kosma, K. Sakai, E. P. Giannelis and C. K. Ober, *J. Micro/Nanolitho. MEMS MOEMS*, 2018, **18**, 1.
- [7] L. Wu, M. Baljovic, G. Portale, D. Kazazis, M. Vockenhuber, T. Jung, Y. Ekinici and S. Castellanos, *J. Micro/Nanolithogr., MEMS, MOEMS*, 2019, **18**, 013504.
- [8] E. C. Mattson, Y. Cabrera, S. M. Rupich, Y. Wang, K. A. Oyekan, T. J. Mustard, M. D. Halls, H. A. Bechtel, M. C. Martin and Y. J. Chabal, *Chem. Mater.*, 2018, **30**, 6192–6206.
- [9] U. Schubert, *Coord. Chem. Rev.*, 2017, **350**, 61–67.
- [10] U. Schubert, *Chem. Soc. Rev.*, 2011, **40**, 575–582.
- [11] H. Xu, K. Sakai, K. Kasahara, V. Kosma, K. Yang, H. C. Herbol, J. Odent, P. Clancy, E. P. Giannelis and C. K. Ober, *Chem. Mater.*, 2018, **30**, 4124–4133.
- [12] R. Maas, M.-C. van Lare, G. Rispens and S. F. Wuister, *J. Micro/Nanolithogr., MEMS, MOEMS*, 2018, **17**, 041003.
- [13] G. Kickelbick and U. Schubert, *Chem. Ber.*, 1997, **130**, 473–477.
- [14] S. Castellanos, L. Wu, M. Baljovic, G. Portale, D. Kazazis, M. Vockenhuber, Y. Ekinici and T. Jung, *Proc. SPIE*, 2018, **10583**, 105830A.
- [15] C. Artner, M. Czakler and U. Schubert, *Chem. Eur. J.*, 2014, **20**, 493–498.
- [16] T. Frot, S. Cochet, G. Laurent, C. Sassoie, M. Popall, C. Sanchez and L. Rozes, *Eur. J. Inorg. Chem.*, 2010, 5650–5659.

- [17] P. Piszczek, A. Radtke, A. Grodzicki, A. Wojtczak and J. Chojnacki, *Polyhedron*, 2007, **26**, 679–685.
- [18] P. Piszczek, M. Richert, A. Grodzicki, T. Głowiak and A. Wojtczak, *Polyhedron*, 2005, **24**, 663–670.
- [19] C. H. Hendon, D. Tiana, M. Fontecave, C. Sanchez, L. D'Arras, C. Sassoys, L. Rozes, C. Mellot-Draznieks and A. Walsh, *J. Am. Chem. Soc.*, 2013, **135**, 10942–10945.
- [20] F. R. Kogler, M. Jupa, M. Puchberger and U. Schubert, *J. Mater. Chem.*, 2004, **14**, 3133–3138.
- [21] J. Kreutzer, M. Puchberger, C. Artner and U. Schubert, *Eur. J. Inorg. Chem.*, 2015, **2015**, 2145–2151.
- [22] V. Guillerm, S. Gross, C. Serre, T. Devic, M. Bauer and G. Férey, *Chem. Commun.*, 2010, **46**, 767–769.
- [23] L. Wu, M. Vockenhuber, Y. Ekinici and S. Castellanos, *Proc. SPIE*, 2019, **10957**, 109570B.
- [24] L. Wu, M. Tiekink, A. Giuliani, L. Nahon and S. Castellanos, *J. Mater. Chem. C*, 2019, **7**, 33–37.
- [25] B. C. Bookser and S. Zhu, *J. Comb. Chem.*, 2001, **3**, 205–215.
- [26] H. M. Anasthas and V. G. Gaikar, *React. Funct. Polym.*, 2001, **47**, 23–35.
- [27] H. Uslu and S. Majumder, *J. Chem. Eng. Data*, 2017, **62**, 1501–1506.
- [28] S. Kumar, S. Batra and D. Datta, *J. Mol. Liq.*, 2017, **247**, 289–293.
- [29] N. Mojarad, J. Gobrecht and Y. Ekinici, *Microelectron. Eng.*, 2015, **143**, 55–63.

Hole stabilizing ligands in Ti-based metal oxo clusters: a gas phase study*

Abstract

In this chapter, we investigate the photoionization process induced by synchrotron radiation in the 7–12 eV photon energy range of a series of octameric ring-shaped titanium oxo cluster cations in the gas phase by tandem mass spectrometry. The photoionization threshold of the parent ion was decreased by about 2 eV as a result of the doping of the organic shell of the pristine pivalate titanium oxo cluster with bis-thiophenylcarboxylate (BTC), 4-(9H-carbazol-9-yl)benzoate (CB), and anthracene carboxylate (AC) ligands. In addition, the ionization process is found non-dissociative in the case of the doped titanium oxo clusters, unlike the non-doped parent pivalate titanium oxo cluster, which undergoes ligand loss upon ionization. These results indicate that the doping with extended aromatic structures stabilizes the ionization product of the clusters, which is consistent with our DFT calculations, showing that the highest occupied molecular orbital (HOMO) resides on the aromatic system in the case of the doped titanium oxo clusters. These experiments evidence that doping of the organic shell of metal oxo clusters is a powerful strategy to tune their photochemical reactivity and highlight the potential of this type of compounds as EUV resists.

*The content of this chapter has been published in: L. Wu, M. Tiekink, A. Giuliani, L. Nahon and S. Castellanos, *J. Mater. Chem. C* **2019**, 7, 33–37. Supporting information is available for free via the Internet at <https://doi.org/10.1039/C8TC05273E>.

5.1 Introduction

Hybrid inorganic–organic materials are catching the attention of scientists in the field of nanolithography in connection with the introduction of extreme ultraviolet (EUV) lithography.^{1–4} This new technology is currently being implemented in the semiconductor industry in order to reach the sub-20 nm nodes required for the steady miniaturization of the components in integrated circuits. The much shorter wavelength (13.5 nm) employed by EUV lithography as compared to the ones used in traditional optical lithography (365, 248, or 193 nm light) allows to achieve the theoretical limit of 10 nm resolution in the optical projection. This drastic change in photon energy poses some challenges for the state-of-the-art photoresists, the photoactive materials that capture the optical pattern. A major concern is the low absorption of previous photoresists based on polymeric platforms at 13.5 nm. Another fundamental problem is that the correlation between the materials' reactivity towards EUV light and its molecular structure is not well established, given the complexity of the EUV-induced chemistry. In contrast to the previous lithography, where a photoacid generator was selectively excited with UV light, the energy of EUV light surpasses by far the ionization potential of the photoresist material and leads to photoelectron emission, even from core atomic levels.⁵ The photoemitted electrons scatter through the material and transfer their energy inducing further excitations and ionizations in the surrounding material.^{2,6} Investigating at the molecular level the contribution of each of these processes to the formation of the final pattern is necessary in order to design new photoresists for EUV lithographic applications.

Metal oxo clusters (MOCs), as molecular hybrid materials with a core/shell-like configuration,^{7–9} are promising EUV photoresists.^{10,11} The inorganic metal oxo core gives MOCs enhanced EUV absorption,¹² and, as shown by other inorganic photoresists, can potentially yield better mechanical and chemical stability as well as etch resistance in the final patterns, as compared to conventional organic photoresist.^{13,14} The molecular identity of MOCs, in turn, provides them with small and homogeneous size, which is expected to decrease the roughness of the patterns generated by EUV lithography. Recently, we proved that these types of materials can effectively work as EUV photoresists and that their EUV absorption and sensitivity can be modified by playing with the composition of the inorganic core.¹⁰ In addition, because of their exchangeable organic shell,^{15–17} MOCs have a remarkable synthetic versatility.

In this work, we took advantage of this last feature to tune the photon-induced reactivity of Ti-MOCs. The organic shells of Ti-based MOCs were “doped” with extended aromatic ligands to modify their highest occupied molecular orbital (HOMO) levels. By raising the energy of the HOMO, the ionization energy is lowered. It has been reported that EUV chemically amplified resists (CARs) with lower band gaps lead to the generation of more acids.¹⁸ This is attributed to the formation of more electron–hole pairs during the scattering of photoelectrons emitted upon EUV absorption. Meanwhile, the resulting holes can be stabilized in the conjugated structure, which can be used as a channel to modulate hole-induced

reactivity. Thus, by tuning the band gap of the materials and of the localization of their frontier orbitals, it is anticipated that their reactivity upon EUV exposure can be also tuned.

The photodissociation and photoionization of this series of Ti-based MOCs towards vacuum ultraviolet (VUV) radiation in the 7–12 eV energy range were investigated in the gas phase by mass spectrometry (MS). Although vacuum ultraviolet action spectroscopy based on mass spectrometry (VUV-MS) has been previously used to study metallic nanoparticles,^{19–21} and very recently to study molecular tin-based oxo-cages,²² to the best of our knowledge, this is the first time that this technique is used to investigate the photochemistry of well-defined metal oxo clusters. These experiments confirm the effect of the doping with aromatic ligands onto the ionization potential and stabilization of the ionized products. Furthermore, the study of the fragmentation processes induced by different photon energies can help to understand the chemistry triggered upon irradiation with higher energy photons, *i.e.* EUV photons. Specifically, it can give insights into the chemistry induced upon exposure to EUV light during the lithographic application, which mainly leads to the ionization of the material.

5.2 Experimental

General remarks. Reagents and solvents were purchased from Sigma-Aldrich and used as received without further purification.

Synthesis of titanium oxo clusters. $\text{Ti}_8\text{O}_8(\text{OOCtBu})_{16}$, denoted as Ti_8L_{16} , and 4-(9H-carbazol-9-yl)benzoic acid (CBA) were synthesized as previously reported.^{23–25} The doping of the organic shell to synthesize $\text{Ti}_8\text{L}_{15}\text{CB}$, $\text{Ti}_8\text{L}_{15}\text{BTC}$ and $\text{Ti}_8\text{L}_{15}\text{AC}$ was performed through ligand exchange reactions. A solution of the aromatic carboxylic acid (1:1 molar ratio) in chloroform was added to a solution of Ti_8L_{16} in chloroform. The resulting yellow-green solution was stirred magnetically at room temperature for 1 hour. The solvent was evaporated under vacuum. Acetonitrile was added to the yellow solid. The suspension was filtered and washed with acetonitrile. The product was dried under vacuum and characterized with ^1H NMR and IR (see Fig. S1–S8 in Supporting Information).

DFT calculations. DFT calculations of titanium oxo clusters were performed using Gaussian 09.²⁶ The geometries of molecules were optimized using DFT calculations with the hybrid B3LYP functional and the 6-31G(d) basis set.^{27,28} The pivalate ligands of the oxo clusters were simplified to acetate ligands to save computational efforts.

Ionization and vacuum ultraviolet action spectroscopy based on mass spectrometry. Mass spectrometry was performed using a linear quadrupolar ion trap (Thermo Scientific LTQ XL) mass spectrometer using an atmospheric pressure photoionization (APPI) source, and coupled to the DESIRS beamline at SOLEIL synchrotron radiation facility (France),^{29,30} allowing to perform VUV action spectroscopy. In each experiment, 1 mg of analyte (titanium oxo cluster) was dissolved in 1 mL toluene and the solution was filtered before infusion into

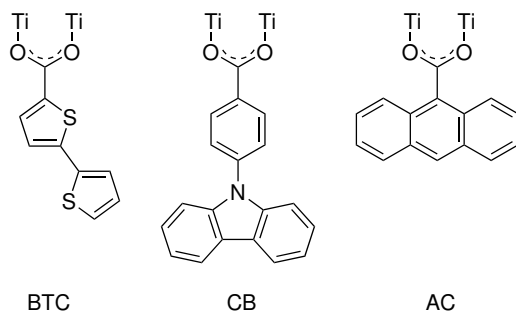
the APPI source at 4–6 $\mu\text{L}/\text{min}$ flow rates. The molecule was ionized by the krypton discharge lamp of the ion source. The targeted precursor ions $[\text{P}]^+ = [\text{M-L}]^+$ (where M = titanium oxo cluster and L = pivalate ligand) were selectively trapped and irradiated at a suitable photon dose that did not yield photoproducts above 10% relative yield and mass spectra were recorded in the 7–12 eV energy range. Photons were monochromatized by a 200 grooves per mm low dispersion grating and filtered from any high order light contribution using a Kr-filled gas filter. Fragmentation yield curves were normalized to the photon flux variations as measured by a Si photodiode (IRD AXUV).

5.3 Results and Discussion

5.3.1 Calculated frontier molecular orbitals

The MOCs investigated in this work consist of an octameric ring-shaped titanium oxo cluster connected through 8 bridging oxygen atoms and 16 bridging carboxylate ligands (8 in equatorial position and 8 in axial position with respect to the ring). In the precursor material, the cluster features 16 pivalate ligands (Ti_8L_{16} , L = pivalate). Three carboxylate ligands based on extended aromatic systems were selected to dope the organic shell of the pivalate titanium oxo cluster precursor: 4-(9H-carbazol-9-yl)benzoate (CB)^{24,25} and 2,2'-bithiophene-5-carboxylate (BTC) featuring electron-rich heteroaromatic structures, and 9-anthracenecarboxylate (AC), as shown in Scheme 5.1. Each aromatic carboxylate ligand was incorporated in the titanium oxo pivalate cluster Ti_8L_{16} by means of ligand exchange to yield $\text{Ti}_8\text{L}_{15}\text{CB}$, $\text{Ti}_8\text{L}_{15}\text{BTC}$ and $\text{Ti}_8\text{L}_{15}\text{AC}$, respectively.

Fig. 5.1 shows the calculated highest-occupied molecular orbital (HOMO) and lowest unoccupied molecular orbital (LUMO) energy and contour plot of the newly designed titanium oxo clusters when a ligand doping ratio of 1:15 is used. To simplify the calculation, acetate titanium oxo clusters, rather than pivalate titanium oxo clusters were used. The two isomers resulting from the substitution of a pi-



Scheme 5.1: Aromatic ligands introduced in the $\text{Ti}_8\text{O}_8\text{Piv}_{16}$ (Ti_8L_{16}) cluster by ligand exchange.

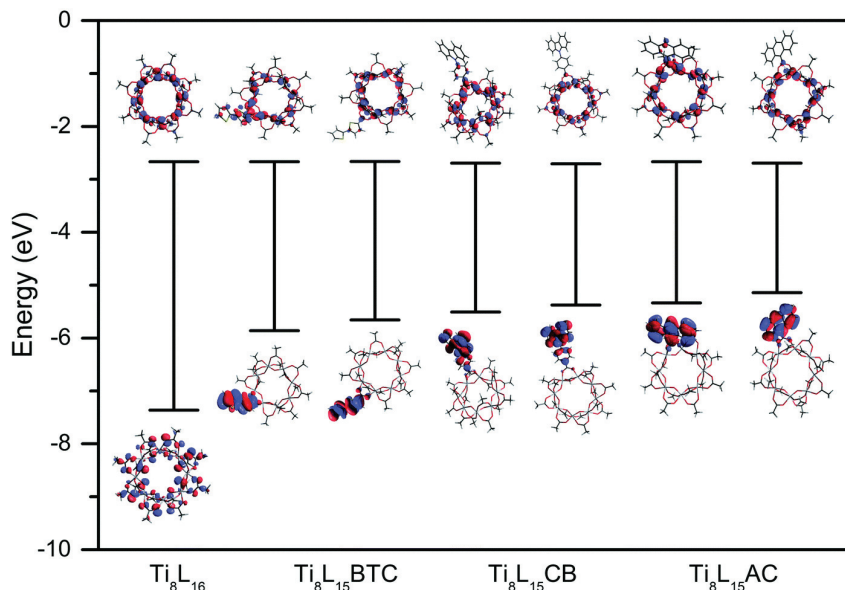


Figure 5.1: HOMO/LUMO energies and contour plots of the different titanium oxo clusters calculated with DFT using the hybrid B3LYP functional and the 6-31G(d) basis set.

valate ligand in the axial or the equatorial position have been considered. According to the DFT calculations, the HOMOs of the doped titanium oxo clusters are located on the corresponding aromatic ligand and their eigenvalues are hence raised in comparison to the pristine cluster featuring only pivalate ligands, while their LUMOs remain on the ring structure of octameric titanium oxo core regardless of the presence of doping ligands. The calculated HOMO energy of Ti_8L_{16} is 7.37 eV, while this value increases by 1.5–2.2 eV for $\text{Ti}_8\text{L}_{15}\text{BTC}$, $\text{Ti}_8\text{L}_{15}\text{CB}$, and $\text{Ti}_8\text{L}_{15}\text{AC}$ (for calculations $L = \text{acetate}$), no matter which position (axial/equatorial) the new ligand exchanged (Table S1 in Supporting Information).

5.3.2 Determination of the onset for ionization

APPI was used to generate the parent charged species from the initial neutral titanium oxo cluster molecules. In this technique, photons of 10.0 and 10.6 eV emitted by a krypton lamp are shone on the gas phase formed from the neutral molecules and the solvent (toluene). The latter gets ionized and reacts by charge exchange and/or proton transfer reactions with the neutral molecule. In the case of this series of titanium oxo clusters, APPI yielded the product corresponding to the loss of one pivalic acid, $[\text{M-L}]^+$. The resulting positively charged $[\text{M-L}]^+$ ion was selectively trapped as parent ion $[\text{P}]^+$ for VUV-MS experiments. The trapped parent ions were clearly identified as $[\text{Ti}_8\text{L}_{15}]^+$ with m/z 2027.5, $[\text{TiL}_{14}\text{BTC}]^+$ with

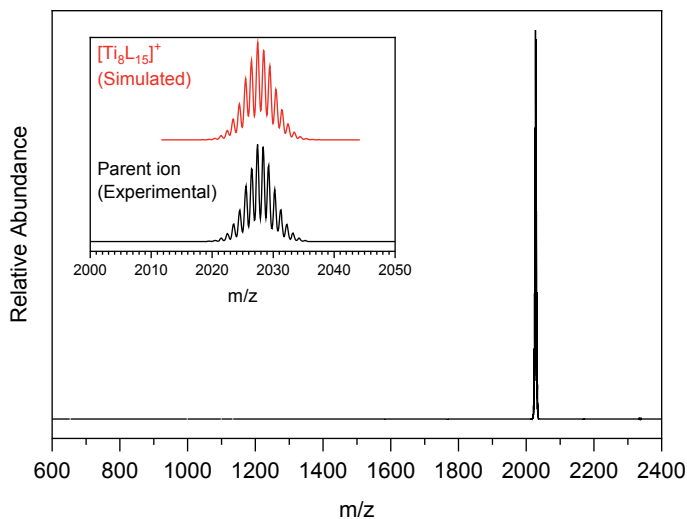


Figure 5.2: Mass spectra of parent ion $[\text{Ti}_8\text{L}_{15}]^+$ and the simulated isotopic distribution.

m/z 2135.4, $[\text{Ti}_8\text{L}_{14}\text{CB}]^+$ with m/z 2212.5, and $[\text{TiL}_{14}\text{AC}]^+$ with m/z 2147.5, respectively (Fig. 5.2). In all cases, the isotopic distribution perfectly matches the expected ratios for an octameric titanium oxo cluster (see Fig. S9–S11 in Supporting Information).

Fig. 5.3 displays the mass spectra of four trapped parent ions after VUV irradiation at 11 eV. For all four parent ions, the main photoproduct is identified as the product of pivalate photodissociation $[\text{P-L}]^+$: $[\text{Ti}_8\text{L}_{14}]^{+\bullet}$ (m/z 1926), $[\text{Ti}_8\text{L}_{13}\text{BTC}]^{+\bullet}$ (m/z 2035), $[\text{Ti}_8\text{L}_{13}\text{CB}]^{+\bullet}$ (m/z 2111), and $[\text{Ti}_8\text{L}_{13}\text{AC}]^{+\bullet}$ (m/z 2046), respectively. Note that the dissociation of the aromatic ligand from the doped parent to yield $[\text{Ti}_8\text{L}_{14}]^+$ was barely detected. Dications $[\text{Ti}_8\text{L}_{14}\text{BTC}]^{2+\bullet}$ (m/z 1068), $[\text{Ti}_8\text{L}_{14}\text{CB}]^{2+\bullet}$ (m/z 1107), and $[\text{TiL}_{14}\text{AC}]^{2+\bullet}$ (m/z 1074) also appear in the spectra, although in much lower concentration. Interestingly, in the case of the non-doped titanium oxo cluster, the ionized parent ion $[\text{Ti}_8\text{L}_{15}]^{2+\bullet}$ was not detected and only the dication $[\text{Ti}_8\text{L}_{14}]^{2+}$ (m/z 913) appears in the low mass region of the spectrum. Finally, dicationic species assigned to $[\text{P-L}]^{2+}$, $[\text{Ti}_8\text{L}_{13}\text{BTC}]^{2+}$ (m/z 966), $[\text{Ti}_8\text{L}_{13}\text{CB}]^{2+}$ (m/z 1005), and $[\text{TiL}_{13}\text{AC}]^{2+}$ (m/z 972) were present in much lower concentration.

In order to determine the photoionization energy threshold for this set of materials, the relative yield of dication formation upon irradiation in the 7–12 eV energy range for the non-doped $[\text{Ti}_8\text{L}_{15}]^+$ and doped $[\text{Ti}_8\text{L}_{14}\text{BTC}]^+$, $[\text{Ti}_8\text{L}_{14}\text{CB}]^+$, and $[\text{Ti}_8\text{L}_{14}\text{AC}]^+$ was monitored (Fig. 5.4). In the plots, it can be observed that the dicationic species $[\text{P-L}]^{2+}$ is detected above 11 eV in all compounds. However, in the case of the doped clusters, an extra curve can be plotted for the “clean” photoionization product $[\text{P}]^{2+}$, which is not accompanied by ligand disso-

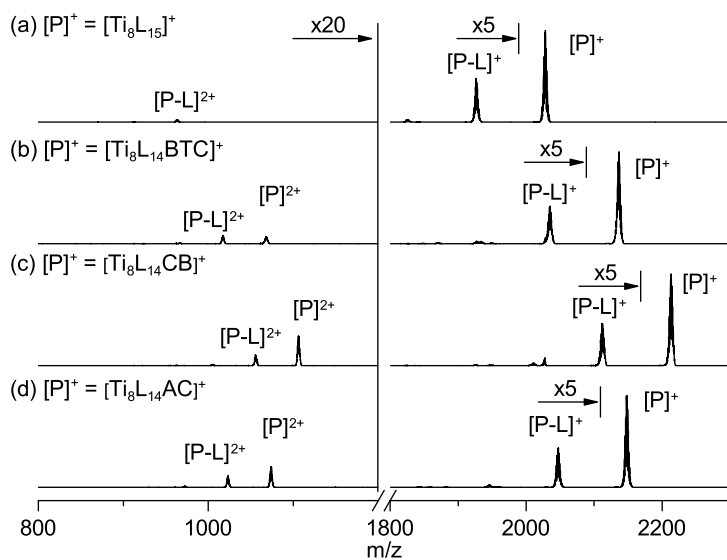


Figure 5.3: Mass spectra after photon activation at 11 eV for four parent ions.

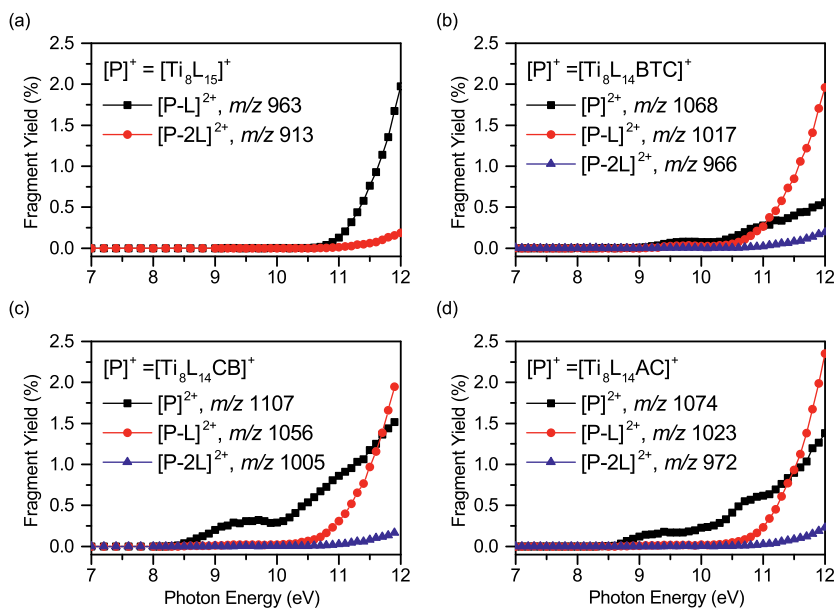
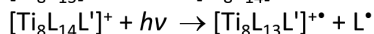
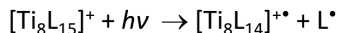


Figure 5.4: Fragment yields resulting from ionization of the parent ion $[P]^+$ as a function of photon energy.

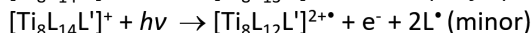
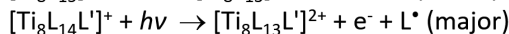
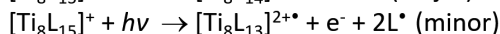
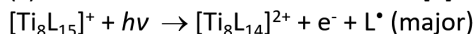
(a) $h\nu > 7$ eV pivalate ligand dissociation $[P]^+ \rightarrow [P-L]^+$



(b) $h\nu > 8.4 - 9$ eV ionization of doped parent clusters $[P]^+ \rightarrow [P]^{2+}$



(c) $h\nu > 11$ eV dissociative ionization $[P]^+ \rightarrow [P-L]^{2+}$



Scheme 5.2: Proposed photoexcitation reactions of the parent ions for the pristine titanium oxo cluster and the derived doped series.

ciation. The ionization energy onsets for the doped compounds are 9.0 ± 0.6 eV for $[\text{Ti}_8\text{L}_{14}\text{BTC}]^+$, 8.4 ± 0.5 eV for $[\text{Ti}_8\text{L}_{14}\text{CB}]^+$ and 8.6 ± 0.3 eV for $[\text{Ti}_8\text{L}_{14}\text{AC}]^+$ (see Fig. S12–S15 Supporting Information*).

These results indicate that in the case of the doped MOCs, which feature one aromatic ligand, the hole generated upon photoionization can be stabilized by the conjugated system. The non-doped parent compound, on the other hand, undergoes a dissociative ionization where a pivalate ligand is lost so that no $[\text{TiL}_{15}]^{2+\bullet}$ species is detected. The lower energy onsets for the photoionization of the doped clusters nicely follow the trends in their calculated HOMO values, where the presence of the aromatic ligands raises the HOMO levels by 1.5 to 2.2 eV. Yet, above 11 eV all compounds undergo a dissociative ionization. The photoreactions in the 7–12 eV energy range for the studied oxo clusters are summarized in Scheme 5.2.

5.3.3 Fragmentation yields as a function of the irradiation energy

The plot of the total fragmentation yield normalized by the photon flux as a function of photon energy gives the action spectra (equivalent to an absorption spectrum) of the four titanium oxo clusters (Fig. 5.5). Photon absorption below 8.4 eV only yields the photodissociation of the pivalate ligands (see Fig. S16 in Supporting Information). Above, multiple decay paths contribute to the spectra: pivalate dissociation, net ionization, and dissociative ionization. A broad band can be observed at 8.5 eV for all compounds except for $[\text{Ti}_8\text{L}_{14}\text{CB}]^+$, where it appears as a smooth shoulder. At 10.5 eV, on the other hand, a sharp peak can

*Correction: The errors of ionization energy onsets in the publication were relative errors calculated from the linear fitting parameters based on error propagation rules.

be observed in all oxo clusters. This spectral feature could be related to a shape resonance in the dissociative ionization channel previously discussed.

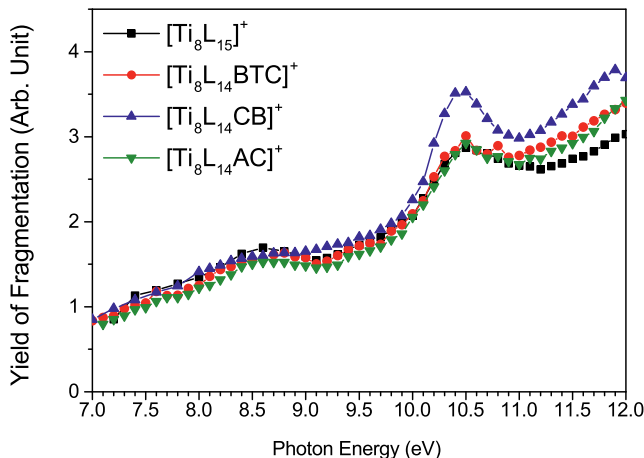


Figure 5.5: Action spectra of parent ions $[\text{Ti}_8\text{L}_{15}]^+$, $[\text{Ti}_8\text{L}_{14}\text{BTC}]^+$, $[\text{Ti}_8\text{L}_{14}\text{CB}]^+$, and $[\text{Ti}_8\text{L}_{14}\text{AC}]^+$. The estimated error is 16% (error bars are omitted for better visualization).

5.4 Conclusion

Doping the organic shell of Ti-based metal oxo clusters with extended aromatic structures proved to be a straightforward method to decrease the photoionization threshold of this compound and to stabilize the ionized species, as evidenced by photofragmentation studies using VUV-MS. While the pristine titanium oxo cluster $\text{Ti}_8\text{O}_8\text{Piv}_{16}$ only undergoes dissociative ionization when irradiated with photon energies above 11 eV, the incorporation of phenylcarbazole-, bis-(thienyl)-, and anthracenyl-based carboxylate ligands in a 1:15 ratio opens an extra ionization channel located at ~ 2.0 – 2.5 eV lower energies. This different reactivity is attributed to the introduction of a new HOMO level that is mainly located in the aromatic doping ligand. This work highlights the great potential of MOCs as photoresists, since the synthetic versatility offered by ligand exchange reactions can be exploited to modify at will the reactivity of their ionized states. This feature makes them ideal molecular materials for the study of EUV induced photochemistry and will assist in the development of new EUV photoresist materials.

Bibliography

- [1] M. Neisser, K. Cho and K. Petrillo, *J. Photopolym. Sci. Technol.*, 2012, **25**, 87–94.
- [2] P. D. Ashby, D. L. Olynick, D. F. Ogletree and P. P. Naulleau, *Adv. Mater.*, 2015, **27**, 5813–5819.
- [3] L. Li, S. Chakrabarty, K. Spyrou, C. K. Ober and E. P. Giannelis, *Chem. Mater.*, 2015, **27**, 5027–5031.
- [4] L. Li, X. Liu, S. Pal, S. Wang, C. K. Ober and E. P. Giannelis, *Chem. Soc. Rev.*, 2017, **46**, 4855–4866.
- [5] K. D. Closser, D. F. Ogletree, P. Naulleau and D. Prendergast, *J. Chem. Phys.*, 2017, **146**, 164106.
- [6] A. Narasimhan, L. Wisheart, S. Grzeskowiak, L. E. Ocola, G. Denbeaux and R. L. Brainard, *J. Photopolym. Sci. Technol.*, 2017, **30**, 113–120.
- [7] U. Schubert, *Coord. Chem. Rev.*, 2017, **350**, 61–67.
- [8] U. Schubert, *Chem. Soc. Rev.*, 2011, **40**, 575–582.
- [9] L. Rozes and C. Sanchez, *Chem. Soc. Rev.*, 2011, **40**, 1006–1030.
- [10] S. Castellanos, L. Wu, M. Baljovic, G. Portale, D. Kazazis, M. Vockenhuber, Y. Ekinici and T. Jung, *Proc. SPIE*, 2018, **10583**, 105830A.
- [11] H. Xu, K. Sakai, K. Kasahara, V. Kosma, K. Yang, H. C. Herbol, J. Odent, P. Clancy, E. P. Giannelis and C. K. Ober, *Chem. Mater.*, 2018, **30**, 4124–4133.
- [12] R. Fallica, J. Haitjema, L. Wu, S. Castellanos, , A. M. Brouwer and Y. Ekinici, *J. Micro/Nanolithogr., MEMS, MOEMS*, 2018, **17**, 023505.
- [13] M. Trikeriotis, M. Krysak, Y. S. Chung, C. Ouyang, B. Cardineau, R. L. Brainard, C. K. Ober, E. P. Giannelis and K. Cho, *J. Photopolym. Sci. Technol.*, 2012, **25**, 583–586.
- [14] D. De Simone, M. Mao, M. Kocsis, P. De Schepper, F. Lazzarino, G. Vandenberghe, J. Stowers, S. Meyers, B. L. Clark, A. Grenville, V. Luong, F. Yamashita and D. Parnell, *Proc. SPIE*, 2016, **9776**, 97760B.
- [15] J. Kreutzer, M. Puchberger, C. Artner and U. Schubert, *Eur. J. Inorg. Chem.*, 2015, **2015**, 2145–2151.
- [16] P. Walther, M. Puchberger, F. R. Kogler, K. Schwarz and U. Schubert, *Phys. Chem. Chem. Phys.*, 2009, **11**, 3640–3647.
- [17] T. Frot, S. Cochet, G. Laurent, C. Sassoie, M. Popall, C. Sanchez and L. Rozes, *Eur. J. Inorg. Chem.*, 2010, 5650–5659.
- [18] S. Grzeskowiak, J. Kaminsky, S. Gibbons, M. Murphy, J. Chandonait, R. L. Brainard and G. Denbeaux, *Proc. SPIE*, 2018, **10586**, 105860D.
- [19] S. Daly, M. Krstić, A. Giuliani, R. Antoine, L. Nahon, A. Zavras, G. N. Khairallah, V. Bonačić-Koutecký, P. Dugourd and R. A. J. O’Hair, *Phys. Chem. Chem. Phys.*, 2015, **17**, 25772–25777.
- [20] C. S. Ah, H. S. Han, K. Kim and D.-J. Jang, *J. Phys. Chem. B*, 2000, **104**,

- 8153–8159.
- [21] S. Daly, C. M. Choi, A. Zavras, M. Krstić, F. Chirot, T. U. Connell, S. J. Williams, P. S. Donnelly, R. Antoine, A. Giuliani, V. Bonačić-Koutecky, P. Dugourd and R. A. J. O’Hair, *J. Phys. Chem. C*, 2017, **121**, 10719–10727.
- [22] J. Haitjema, L. Wu, A. Giuliani, L. Nahon, S. Castellanos, and A. M. Brouwer, *J. Photopolym. Sci. Technol.*, 2018, **31**, 243–247.
- [23] P. Piszczek, M. Richert, A. Grodzicki, T. Głowiak and A. Wojtczak, *Polyhedron*, 2005, **24**, 663–670.
- [24] S.-H. Hsiao and Y.-T. Chiu, *RSC Adv.*, 2015, **5**, 90941–90951.
- [25] G.-S. Liou, S.-H. Hsiao, N.-K. Huang and Y.-L. Yang, *Macromolecules*, 2006, **39**, 5337–5346.
- [26] M. J. Frisch, G. W. Trucks, H. B. Schlegel, G. E. Scuseria, M. A. Robb, J. R. Cheeseman, G. Scalmani, V. Barone, G. A. Petersson, H. Nakatsuji, X. Li, M. Caricato, A. Marenich, J. Bloino, B. G. Janesko, R. Gomperts, B. Mennucci, H. P. Hratchian, J. V. Ortiz, A. F. Izmaylov, J. L. Sonnenberg, D. Williams-Young, F. Ding, F. Lipparini, F. Egidi, J. Goings, B. Peng, A. Petrone, T. Henderson, D. Ranasinghe, V. G. Zakrzewski, J. Gao, N. Rega, G. Zheng, W. Liang, M. Hada, M. Ehara, K. Toyota, R. Fukuda, J. Hasegawa, M. Ishida, T. Nakajima, Y. Honda, O. Kitao, H. Nakai, T. Vreven, K. Throssell, J. A. Montgomery, J. Peralta, J. E., F. Ogliaro, M. Bearpark, J. J. Heyd, E. Brothers, K. N. Kudin, V. N. Staroverov, T. Keith, R. Kobayashi, J. Normand, K. Raghavachari, A. Rendell, J. C. Burant, S. S. Iyengar, J. Tomasi, M. Cossi, J. M. Millam, M. Klene, C. Adamo, R. Cammi, J. W. Ochterski, R. L. Martin, K. Morokuma, O. Farkas, J. B. Foresman and D. J. Fox, *Gaussian 09, Revision A.02*, Gaussian, Inc., Wallingford CT, 2009.
- [27] Y. Fan, H.-M. Li, R.-H. Duan, H.-T. Lu, J.-T. Cao, G.-D. Zou and Q.-S. Jing, *Inorg. Chem.*, 2017, **56**, 12775–12782.
- [28] H.-T. Lv, H.-M. Li, G.-D. Zou, Y. Cui, Y. Huang and Y. Fan, *Dalton Trans.*, 2018, **47**, 8158–8163.
- [29] A. R. Milosavljevic, C. Nicolas, J.-F. Gil, F. Canon, M. Réfrégiers, L. Nahon and A. Giuliani, *J. Synchrotron Radiat.*, 2012, **19**, 174–178.
- [30] L. Nahon, N. De Oliveira, G. A. Garcia, J.-F. Gil, B. Pilette, O. Marcouillé, B. Lagarde and F. Polack, *J. Synchrotron Radiat.*, 2012, **19**, 508–520.

A fluorescent ligand in a Zr-based metal oxo cluster*

Abstract

Extreme ultraviolet (EUV) lithography uses 13.5 nm light to reach sub-20 nm resolution. However, the process of pattern formation induced by this high-energy light is not well-understood. In this work, we provided an inorganic EUV photoresist with fluorescent properties to study the patterning process by introducing a carbazole-derivative as a ligand. The resulting material displayed a remarkable loss of sensitivity towards EUV light. The mechanism behind this effect was investigated using fluorescence spectroscopy and microscopy in combination with infrared and UV-visible absorption spectroscopy. Hole traps and steric hindrance provided by the carbazole benzoate ligand can be the reasons for the reduced reactivity of the modified photoresist material. Our work shows that fluorescent labelling can give relevant mechanistic insights in the patterning process of resists.

*L. Wu, M. F. Hilbers, O. Lugier, N. Thakur, M. Vockenhuber, Y. Ekinci, A. M. Brouwer, and S. Castellanos, "Introduction of a fluorescent ligand in an inorganic extreme ultraviolet resist", manuscript in preparation. The electronic supplementary information is available at <http://dare.uva.nl/en>.

6.1 Introduction

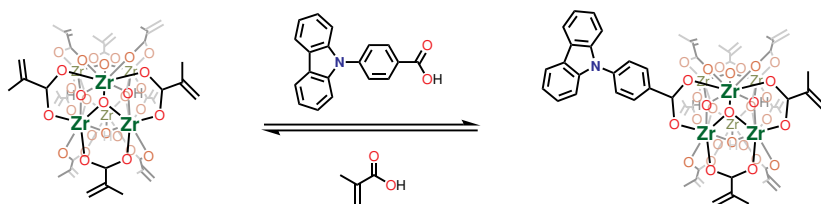
Photolithography is a process to manufacture micro-/nano-electronics in which a mask is used to project light with a desired pattern on a photosensitive layer—known as a (photo)resist—that coats a silicon wafer. After exposure, either the irradiated or non-irradiated parts of the photoresist can be selectively removed in a solvent called developer. This is a consequence of the chemical reactions occurring in the irradiated part, which lead to different solubility properties compared to the pristine material. The patterned photoresist acts as a sacrificial template that allows transferring the desired pattern to the silicon wafer underneath during an etching step. Currently, the fabrication of nanostructures with features smaller than 30 nm using the state-of-the-art deep ultraviolet lithography (DUVL) requires immersion lithography¹ with double or multiple patterning processes to overcome the inherent diffraction limit associated to the employed wavelength (193 nm, $E = 6.4$ eV).^{2–4} In contrast, with the newly developed extreme ultraviolet lithography (EUVL), the desired small features can be printed in one patterning cycle due to its shorter wavelength (13.5 nm, $E = 92$ eV). Therefore, although DUVL still dominates in semiconductor manufacture, EUVL has been launched into the market for the next generation of chips with even smaller features and higher computing performance. Yet, one of the critical points for EUVL to establish in the market is that new photoresist materials with optimal performance need to be developed. However, EUV-induced radiation chemistry in photoresists is not yet as well understood as the photochemistry triggered by DUV light,^{5,6} which hinders their rational design. This is because the chemical reactions induced by EUV photons are the consequence of multiple processes, such as ionization events and the generation of electron cascades in the photoresist.⁷

Metal-containing inorganic-organic hybrid molecular materials, such as metal oxo clusters (MOCs), are being considered as potential EUV resists.^{8–11} In their core/shell-like molecular structure, the metal-oxo core generally contributes the most to the EUV absorptivity and to the etching resistance while the organic ligand-shell determines the reactivity that renders the solubility switch. In MOCs with carboxylate ligands, the dynamic behaviour of carboxylates in solution enables to modify the composition of the ligand shell via exchange reactions^{12,13} and therefore potentially to combine different functionalities in the resulting material.

A way to investigate the lithographic process in a photoresist is to use fluorescent labels. For instance, they can be used to image the transfer of the optical projection to the material. Fluorescent dyes have been employed in the research of polymer-based photoresist used in microlithography.^{14–16} However, the added small molecules that act as fluorescent labels can aggregate in the polymer matrix and induce defects in patterned photoresist films.^{17,18} This limits the use of these labels for photoresist research, especially as the requirements for nanolithography become more constraining in terms of resolution and linewidth roughness. As an alternative, fluorescent ligand doping in MOCs can facilitate the dispersion of the fluorescent label and prevent the phase separation problem, as in this case the ligand is chemically bonded and is thus part of the discrete entities that form the

molecular material.

Here we report a methacrylate (Mc) zirconium oxo cluster $Zr_6O_4(OH)_4(OMc)_{12}$ (denoted as **ZrMc**) functionalized with a fluorescent carboxylate ligand, 4-(9H-carbazol-9-yl)benzoate (CB). The carbazole unit was incorporated into **ZrMc** via ligand exchange reaction in a ratio of one fluorescent label per molecule, *i.e.* the resulting material, denoted as **ZrMc-CB**, features a CB/Mc ratio of 1:11 on average (Scheme 1). This means that the deposited photoresist film retains a high concentration of methacrylate in the organic ligand shell, so that the material's processability is preserved.



Scheme 6.1: Functionalization of ZrMc by ligand exchange.

The influence of the fluorescent CB ligand was expected on four aspects of the MOC-based EUV photoresist. First, from an application point of view, the CB ligand incorporated in the precursor MOC can work as a fluorescent label for the detection of residual resist after development, for the end-point of etching¹⁴ or for the fabrication of fluorescent patterns. Furthermore, fluorescence microscopy is a good metrology tool for the characterization of photoresist patterning since it is a non-invasive technique, as opposed to scanning electron microscopy (SEM) and can offer molecular resolution by means of super-resolution fluorescence imaging techniques.¹⁹ Second, extended aromatic structures have lower electronic band gaps, which provide higher valence band energies than the precursor MOC. Therefore, doping with an extended aromatic carboxylate is expected to lower the ionization potential of the MOCs.²⁰ This could potentially yield more electrons in the secondary electron cascade induced by EUV photons, leading to higher reactivity and sensitivity. On the other hand, this type of ligands also stabilize the radical cations generated after ionization,²⁰ thus preventing a subsequent decarboxylation and cross-linking reactions. Both reactions have been demonstrated as the main contributions to the solubility switch mechanism of **ZrMc** as an EUV photoresist²¹ and for similar materials.^{22,23} Therefore, doping with CB could also lead to a third change in the **ZrMc** properties: the decrease of sensitivity due to lower reactivity. The fourth aspect to consider is that this extended aromatic carboxylate ligand is bulky, which can increase the average intermolecular distance of **ZrMc** in the solid state. A longer packing distance can lead to lower reactivity because it decreases the probability of intermolecular cross-linking between methacrylate ligands. In summary, the introduction of the fluorescent ligand could affect the reactivity in a positive or negative way.

In this work, we examined the influence of incorporating a CB ligand in the

ZrMc MOC on its lithographic performance and used the fluorescence properties provided by this ligand to investigate structural changes occurring on the **ZrMc-CB** resist after EUV exposure together with complementary Fourier-transform infrared (FTIR) and UV-visible absorption spectroscopy. The spectroscopic results indicate that in the functionalized MOC the carbazole unit is rather inert while the Mc ligands are the main contribution to the EUV-induced reactivity of the photoresist material. Yet, the phenylcarbazole unit interferes in the cross-linking mechanism that renders the solubility switch of the material. Our work provides an understanding of the role of different organic components/functional groups in the design of new EUV photoresist materials.

6.2 Experimental

Synthesis

Reagents and solvents were purchased from Sigma-Aldrich and dried with molecular sieves before use. $\text{Zr}_6\text{O}_4(\text{OH})_4(\text{OMc})_{12}$ was synthesized by the reaction of zirconium(IV) propoxide with four molar equivalents of methacrylic acid in dry air instead of inert gas, adapted from the method which has been reported.²⁴ 4-(9H-carbazol-9-yl)benzoic acid (CBA) was synthesized as reported previously.^{25,26} The dynamics of ligand exchange in solution were evidenced by the ^1H and ^{13}C NMR spectra of the 1:1 (molar ratio) CBA:ZrMc in CD_2Cl_2 where peak broadening and changes in chemical shift were observed (Fig. S6.1).

Thin film deposition

To a solution of CBA in chloroform (5.3 mmol, 0.9 mL) **ZrMc** (9.0 mg, 5.3 mmol) was added. The resulting reaction mixture was sonicated at room temperature for 2 minutes and then 0.1 mL of propylene glycol methyl ether acetate (PGMEA) was added. The solution was sonicated for another 2 minutes and filtered before spin-coating. Thin films were spin-coated at a spinning rate of 2100 rpm for 30 seconds with an acceleration of 3000 rpm/s onto Si substrates for patterning tests and for FTIR spectroscopy and on quartz substrates for UV-visible absorption and fluorescence spectroscopies. The samples were baked at 90 °C for 30 seconds after spin-coating, to remove residual solvents. The reference **ZrMc** thin film was prepared in the same way without adding CBA.

EUV exposure and characterization

The spin-coated thin films were irradiated with EUV light at the XIL-II beamline of Swiss Light Source in the Paul Scherrer Institute. Samples for dense line-space patterning were exposed using the EUV interference lithography tool with periodic line/space patterns of pitches of 44, 60, 80, and 100 nm. Samples for contrast curve and fluorescence intensity were exposed with an open-frame mask of $0.5 \times 0.5 \text{ mm}^2$ aperture at varied doses from 2 and 4 to 994 mJ/cm^2 , respectively. Samples for

fluorescence, infrared, and UV-visible absorption spectroscopy were exposed with a $1.7 \times 1.7 \text{ mm}^2$ aperture. The exposure areas were adjacent in a 4×4 square matrix at a single dose of 85, 170, or 425 mJ/cm^2 in order to attain a large exposed area to record full spectra in the spectrometer (no spatial resolution). After exposure, the sample was immersed in chloroform for 30 seconds without further processing for all developed samples.

Fluorescence spectra were measured with a Horiba SPEX Fluorolog 3 spectrometer. The emission spectra were obtained with excitation at 345 nm with a bandwidth of 3 nm and recorded from 360 to 630 nm with a bandwidth of 3 nm. UV absorption spectra of **ZrMc** and **ZrMc-CB** were obtained with a Shimadzu UV-2600 spectrophotometer. FTIR spectra of thin films were recorded on a Bruker VERTEX 80v vacuum FT-IR spectrometer and fast-Fourier transform (FFT) low-pass filtering was applied to the spectra with a cutoff frequency of 0.04 Hz to remove the interference fringes in high wavenumber range. The film thickness was measured by the height referenced to the substrate on a Bruker AFM (Dimension Icon) with the ScanAsyst mode. Top-down SEM image of line-space pattern was recorded using a FEI Verios 460 scanning electron microscope with high voltage of 5.0 kV.

Fluorescence intensity measurement

The fluorescence emission intensity of **ZrMc-CB** exposed at each applied dose of EUV was recorded in the middle of each exposed field using a Picoquant Microtime 200 confocal microscope coupled with a frequency doubled tunable Ti: sapphire laser (Chameleon Ultra, Coherent, $\lambda = 345 \text{ nm}$) and equipped with 447/60 bandpass filter to the detector. The fluorescence intensity at each dose was analysed from the recorded image (field of view: $80 \times 80 \text{ }\mu\text{m}^2$, resolution: 2.5 pixels per μm) using ImageJ software.

Theoretical calculations

Density functional theory (DFT) calculations were performed using the Gaussian 16 package²⁷ with the B3LYP hybrid density functional and the Def2SVP basis set.^{28,29}

6.3 Results and discussion

6.3.1 EUV lithography

To evaluate the lithographic performance of **ZrMc-CB** as an EUV photoresist material, the sample was exposed with an open-frame mask for a dose test known as contrast curve. The same test was performed on **ZrMc** for comparison. For a contrast curve, multiple spots are exposed to a different EUV dose and the thickness remaining after development on each spot indicates the degree of solubility switch of the resist attained after each dose. In the case of a negative tone resist,

as the ones studied here, a ratio of the layer thickness will remain after development above a certain dose threshold. This dose threshold is known as dose-to-gel, D_0 , while the dose required to reach maximum thickness is noted as D_{100} . The contrast factor γ , relates both parameters and is defined as $\gamma = 1/\log_{10}(D_{100}/D_0)$. As shown in Fig. 6.1, **ZrMc-CB** is less sensitive to EUV compared to the non-functionalized MOC **ZrMc**, as it requires a higher dose to become less soluble in the developer of choice.³⁰ Table 6.1 summarizes the D_0 , D_{100} and γ of both materials with the same developer and development process. The curves did not show a significant improvement or deterioration of the contrast factor, but a drop of almost one order of magnitude in the sensitivity for **ZrMc-CB**. The structural changes after EUV exposure responsible for this effect were investigated via spectroscopic techniques in the next section. The top-down SEM image of the line-space pattern of **ZrMc-CB** (Fig. S6.2) also shows a negative effect of the carbazole unit on the sensitivity of the photoresist: for resolving 50 nm half-pitch patterns a higher dose (90 mJ/cm²) was required than for the **ZrMc** material (57 mJ/cm²).²¹

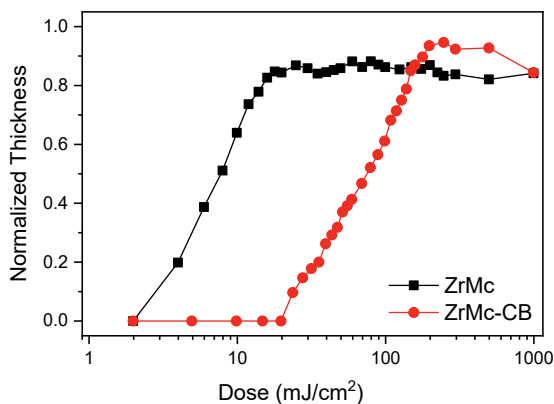


Figure 6.1: Contrast curves of ZrMc and ZrMc-CB, developed in chloroform for 30 seconds, without baking treatment.

Table 6.1: Comparison of sensitivity and contrast between ZrMc and ZrMc-CB*

MOC	D_0 (mJ/cm ²)	D_{100} (mJ/cm ²)	γ
ZrMc	2.5 ± 0.3	16.8 ± 1.7	1.2 ± 0.1
ZrMc-CB	22.6 ± 0.8	195.7 ± 7.2	1.1 ± 0.1

* Standard deviations were calculated from error propagation of the slope and intercept of the fitted line between D_0 and D_{100} .

6.3.2 Fluorescence labeling

The incorporation of the CB ligand in the **ZrMc** provided **ZrMc-CB** with fluorescent emission, as intended. The fluorescence spectra of **ZrMc-CB** thin film display an emission band around 430 nm upon UV excitation while the precursor material **ZrMc** is not fluorescent. We selected three doses to track changes in the spectral shape after EUV exposure. As shown in Fig. 6.2, the emission spectra of exposed samples at doses up to 170 mJ/cm² show only the slight broadening of the emission band. At the highest dose of 425 mJ/cm², the emission peak red-shifts 6 nm. We conclude that no decarboxylation reaction occurs on the CB ligand, as this would yield phenylcarbazole embedded in the film and its fluorescence should lead to the appearance of a new emission band at *ca.* 378 nm.³¹ In general, any bond dissociation that would interrupt the extended aromatic system of the CB ligand would lead to a blue shift of the emission.

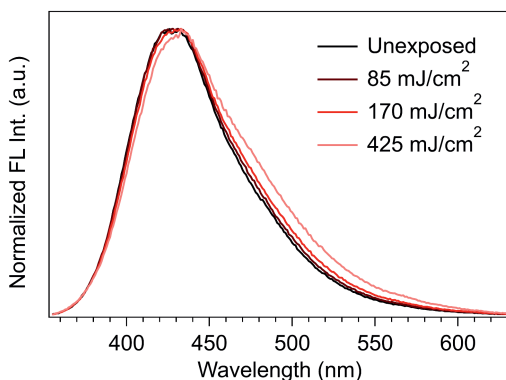


Figure 6.2: Normalized fluorescence spectra of pristine and exposed ZrMc-CB films on quartz ($\lambda_{exc} = 345$ nm).

The changes in the fluorescence emission intensity of **ZrMc-CB** as a function of EUV dose were measured with a fluorescence microscope. In the as-exposed sample (no development step applied), fluorescence is reduced with the dose of EUV exposure but still detectable even at the highest applied dose of 994 mJ/cm² (Fig. 6.3a). In this sample, the reduction of the fluorescence intensity shows different rates at low and high dose regimes, separated at D_{100} . In contrast, in the developed sample the curve of fluorescence intensity displays three regimes (Fig. 6.3b). In the first regime, the emission intensity firstly remains at the background level below D_0 ; the second regime starts where the intensity increases with the exposure dose up to D_{100} ; above this value, the third regime takes place in which the sample is over-exposed, and the emission intensity steadily decreases. Such behaviour in the first two regimes is correlated to the remaining thickness of the photoresist after the development at each dose. As shown in the contrast curve (Fig. 6.1), in the exposed areas that received EUV doses below the solubility switch threshold (D_0), no fluorescent material remains on the substrate after

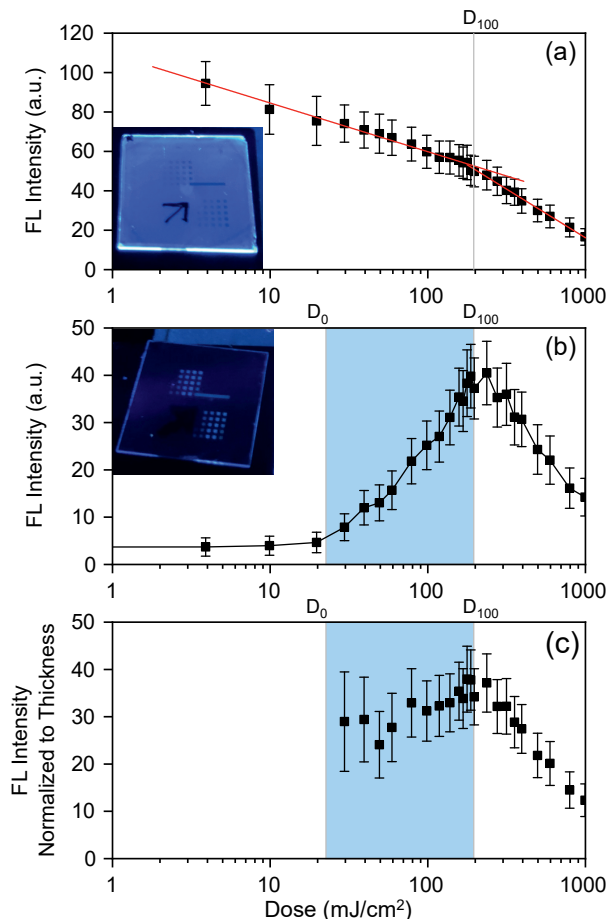


Figure 6.3: (a) Fluorescence intensity of ZrMc-CB film exposed to the given EUV dose before development. (b) Fluorescence intensity of ZrMc-CB film after development. (c) Fluorescence intensity normalized to the thickness of the developed sample.

immersing the sample into the developer, as the material is still soluble in that solvent. The emission intensity increases with the dose between D_0 and D_{100} , in line with the rising amount of material staying in that area on the substrate. In fact, when the fluorescence intensity is normalised to the thickness left at the measured spot, a constant value is obtained for this D_0 – D_{100} range. The third regime displays a decreasing trend in both absolute and normalised scales, in line with the quenching effect observed in the undeveloped sample for this dose range.

Therefore, EUV exposure leads to a decrease in fluorescent emission of the **ZrMc-CB** compared to the unexposed film. Yet, two different dose ranges were detected; below D_{100} , the insoluble product that keeps forming with increasing

dose emits with higher intensity than the product that results from overexposure above D_{100} . The origin of the reduced fluorescence could be bleaching or quenching because of cleavage or modification of the CB ligand, and/or the modification of its surroundings upon EUV irradiation, so that fluorescence quenching is favoured in the environment generated after exposure. Further investigations with FTIR and UV-visible absorption spectroscopy were performed to answer this question.

6.3.3 Fourier-transform infrared spectra

The FTIR absorption spectra of **ZrMc-CB** films exposed to different EUV doses are shown in Fig. 6.4a, with the spectrum of an unexposed **ZrMc-CB** film as the reference. Because of the low concentration of the carbazole benzoate ligand in the MOC film, the spectrum of **ZrMc-CB** shows features mainly from the methacrylate ligands.^{21,23,32} The bands at 2800-3010 cm^{-1} are ascribed to C-H stretching of the methyl group and the absorption at 2960 cm^{-1} shows a significant increase at the dose of 425 mJ/cm^2 . The bands in the range of 1350-1450 cm^{-1} are assigned to COO symmetric stretching overlapping with C-H bending of $-\text{CH}_3$, and bands at 1556-1600 cm^{-1} originate from COO asymmetric stretching. The bands centered at 1640 cm^{-1} and 1240 cm^{-1} are due to the C=C stretching mode and C-C=C rocking mode in the methacrylate respectively. The relative absorption intensity of these four regions decreases with EUV irradiation, while the absorption band from C=C stretching mode bleaches faster than that of COO (Fig. 6.4b). On the other hand, the band centered in 750 cm^{-1} is assigned to the C-H bending mode in the extended-aromatic structure in the carbazole benzoate ligand.³³ This absorption band shows no remarkable change after exposure

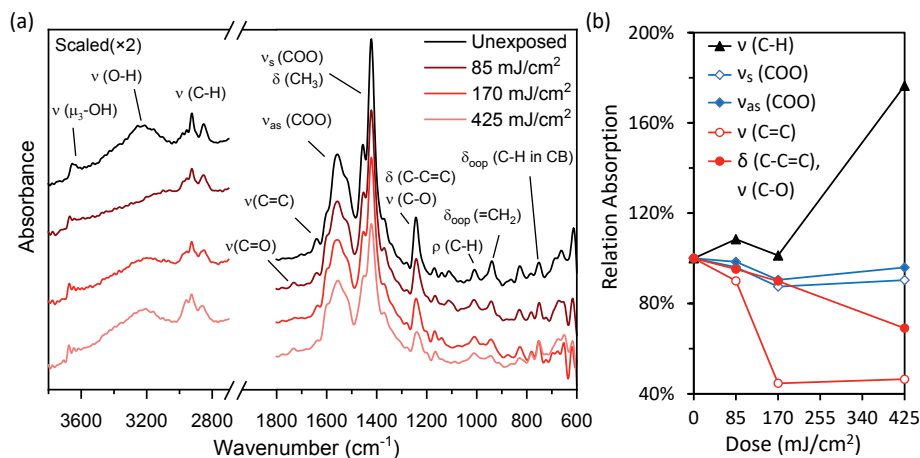


Figure 6.4: (a) IR absorption spectra of an unexposed ZrMc-CB film and films exposed to EUV light of 85, 170, and 425 mJ/cm^2 . (b) The change of relative absorption of C-H, COO and C=C stretching modes.

to EUV light. These trends indicate that ligand cleavage and cross-linking reactions happen in the methacrylate ligands upon EUV irradiation in analogy to the behavior observed for **ZrMc** the precursor.²¹

6.3.4 UV-visible absorption spectra

The UV-visible absorption spectra of CBA solution in pentane, and **ZrMc** and **ZrMc-CB** thin films are shown in Fig. 6.5a. The spectrum of **ZrMc-CB** thin film displays a small baseline drift due to light scattering and a slight redshift with respect to that of CBA in solution. In contrast, the UV absorption spectrum of drop-casted CBA film shows lower intensity for the bands at 291 and 337 nm and a larger redshift compared to **ZrMc-CB** (Fig. S6.4 in Supporting Information). These differences are attributed to π - π stacking of the CB units in the solid state, a very common phenomenon in extended aromatic structures and in particular

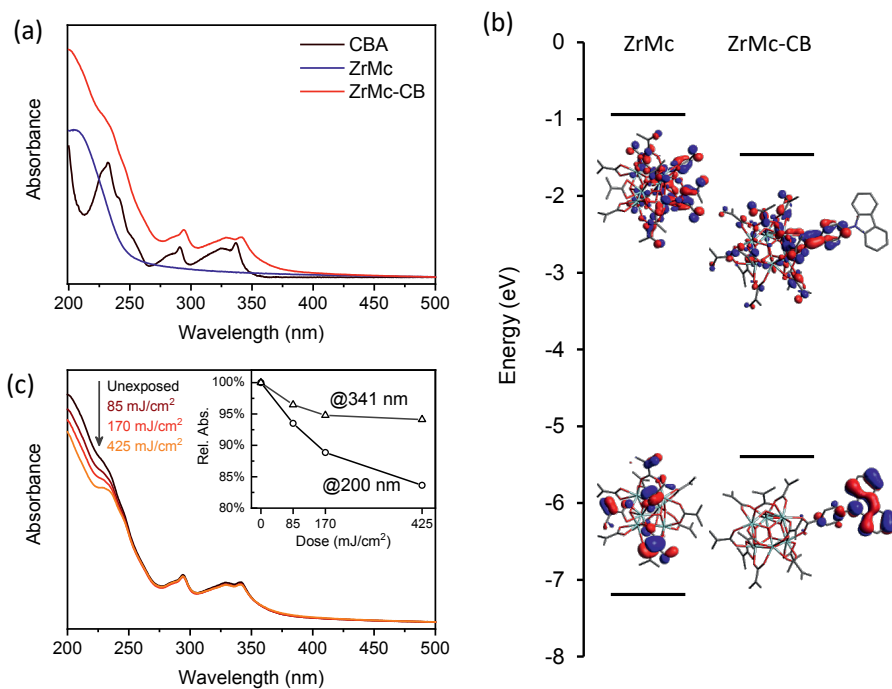


Figure 6.5: (a) UV absorption spectra of CBA in dilute pentane solution (rescaled $\times 0.3$ for clarity), and **ZrMc** and **ZrMc-CB** spin-coated thin films on quartz substrates. (b) The frontier orbitals (HOMO and LUMO) of **ZrMc-CB** calculated at B3LYP level of theory using Def2SVP basis set. (c) UV absorption spectra of unexposed and EUV exposed area in the **ZrMc-CB** film. Inset: Absorption spectral changes of **ZrMc-CB** after EUV exposure of different doses. Normalized to the absorbance of the unexposed sample.

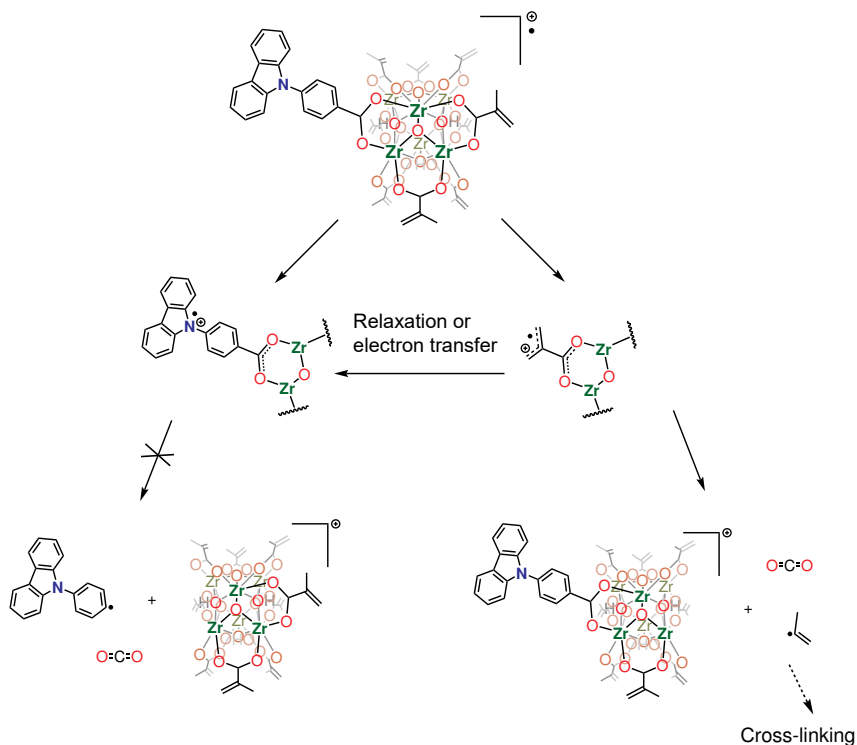
for carbazole derivatives.^{34–36} In the UV absorption spectrum of **ZrMc-CB** thin film, the absorption band around 200 nm is assigned to the $\pi \rightarrow \pi^*$ electronic transition of the methacrylate ligand. The absorption bands around 230–250 nm, 290 nm, and 330 nm originate from the carbazole unit.³⁷ The fact that the bands assigned to the CB present almost no shift in **ZrMc-CB** compared to CBA in solution indicates that there is no strong electronic interaction between the π -system and the metal oxo-core. This is in agreement with quantum chemistry calculations, which reveal that the introduction of CBA in a Zr-MOC brings the highest occupied molecular orbital (HOMO) and the lowest unoccupied molecular orbital (LUMO) localized on the CB ligand (Fig. 6.5b).

After exposure to EUV light with three different doses, the bleaching of absorption bands was detected (Fig. 6.5c). The absorption band at 200 nm of **ZrMc-CB**, assigned to the π - π^* electronic transitions located in the methacrylate ligand, decreased in line with the bleaching of C=C stretching bands in the FTIR spectra. The carbazole absorption in the 275–370 nm range is only slightly bleached (Fig. 6.5c Inset).

6.3.5 Mechanisms of changes in the sensitivity and fluorescence intensity

Different from deep UV exposure, where the absorption and photo-excitation are limited to certain components in resist materials, EUV is mainly absorbed by the atoms with the higher photon-absorption cross-sections at 92 eV. In the case of Zr-based MOC, this is likely to occur at the oxygen atoms. In the case of **ZrMc**, photoionization can lead to the formation of allyl radicals, as previously proposed in the literature.^{21,38} However, in the case of **ZrMc-CB** there is a more complex situation. The O atoms of the Mc ligands participate in different molecular orbitals (HOMO-X and below) compared to the O atoms in the CB ligand (from HOMO to HOMO-Y). This means that two different radical cations can be considered, as shown in the two routes in Scheme 6.2. Yet, it is plausible that when a hole is generated in the O of a Mc ligand, the molecule relaxes by an electron descending from the HOMO to the hole at the deeper molecular orbital, thus yielding the radical cation on the CB ligand. It should be mentioned that ionization can also be induced by the generated photoelectrons and secondary electrons when their kinetic energy is higher than the ionization potential of the molecules. In this case, the probability of the ionization on either ligand is not straight forward to predict.

The cross-linking between clusters through methacrylate ligands is initiated by free-radicals.^{21,38} While Mc ligands can yield free allyl radicals, the radical cation on the carbazole ligands is stabilized and less likely to dissociate. In addition to that, as CB is an electron donor, electron transfer from the neutral CB to Mc radical cations can also prevent the formation of allyl radicals. Therefore as hypothesized in the Introduction, the reactivity of the precursor **ZrMc** can be reduced with the incorporation of the carbazole unit to the cluster because of its hole stabilizing property, as it can decrease the yield of free radicals in the materials upon EUV irradiation.³⁹ This explains the low reactivity and sensitivity



Scheme 6.2: Hole-initiated reactions of ZrMc-CB radical cation induced by EUV that lead to decarboxylation and the formation of free radicals initiating cross-linking.

of **ZrMc-CB** in contrast to **ZrMc**.

Overall, the spectral changes in fluorescence, FTIR, and UV absorption of **ZrMc-CB** films that were exposed to EUV photons up to 170 mJ/cm² are in agreement with the promotion of crosslinking and decarboxylation reactions of Mc ligands with EUV exposures previously proposed for the **ZrMc** material. These reactions still seem to play a crucial role in the solubility switch in **ZrMc-CB**, while the carbazole benzoate ligand is rather stable at those doses. At higher doses, 425 mJ/cm² for example, the UV absorption band is only bleached by 6% at 341 nm while fluorescence emission intensity is about 64% less than that of the unexposed sample. This reveals that the decrease of the fluorescence is not only caused by a lower photon absorption of the excitation light ($\lambda = 345$ nm) but also by other quenching mechanisms. It could be argued that some carbazole derivative with lower fluorescence quantum yield than the intact ligand might be formed after EUV exposure. For instance, carbazole radical cations tend to be reactive in positions 3 and 6.⁴⁰ If water molecules are present in the film, OH groups could insert in position 3 or 6 after ionization of the **ZrMc-CB**, which might affect the

fluorescence of the CB unit. However, this kind of modification in the carbazole will lead to spectral shifts both in the absorption and emission spectra. The subtle spectral changes in the bands associated with CB in UV absorption fluorescence spectra do not support this explanation. Alternatively, the fluorescence quenching could be due to the opening of competing relaxation pathways in the areas that have been chemically modified by EUV light. We hypothesize that decarboxylation reactions occurring in the methacrylate ligands might change the electron affinity of the Zr-based inorganic core. It is plausible that, after partial loss of methacrylate ligands because of EUV irradiation, the inorganic core acts as an electron acceptor so that the excited states of the carbazole unit relax by means of electron transfer, a path that competes with the emissive relaxation. This might explain the progressive decrease of the fluorescence intensity vs dose in Fig. 6.3. At low doses, certain decarboxylation and cross-linking occur. Once the terminal double bonds are depleted (above D_{100}), further decarboxylation events and subsequent processes keep favouring fluorescence quenching.

6.4 Conclusion

In this work, we have demonstrated a straightforward method to functionalize metal oxo clusters with a fluorescent label (carbazole benzoate) via ligand exchange reaction. The processability and lithographic contrast of the precursor material are preserved. Yet, the functionalized MOC showed a drop in the sensitivity which we attribute to the hindering of polymerization reactions, either because the hole trap of CB or because the intermolecular packing distance is increased. Fluorescent spectroscopy allowed us to further investigate how the fluorescent label can give mechanistic information. The carbazole benzoate ligand does not show significant structural changes after EUV exposure. However, its fluorescent emission is quenched, which we attribute to changes in the surrounding matrix induced by EUV light. We propose that electron transfer from the excited phenylcarbazole unit to the inorganic cluster is enabled in the exposed areas and therefore competes with the fluorescent emission. From these results, we predict that extended-aromatic structures can be utilized in the design of new EUV photoresist materials for tuning the reaction kinetics. Furthermore, we envision that, to carry out fluorescent labeling yet avoid the deterioration of the resist sensitivity, the ligand exchange can be applied during or after development for surface modification of the created nanopattern.

Bibliography

- [1] J. Mulkens, D. G. Flagello, B. Streefkerk and P. Gräupner, *J. Micro/Nanolithogr., MEMS, MOEMS*, 2004, **3**, 104–115.
- [2] R. H. French and H. V. Tran, *Annu. Rev. Mater. Res.*, 2009, **39**, 93–126.
- [3] M. Neisser and S. Wurm, *Adv. Opt. Technol.*, 2012, **1**, 217–222.
- [4] M. Neisser and S. Wurm, *Adv. Opt. Technol.*, 2015, **4**, 235–240.
- [5] H. J. Levinson, *Principles of lithography*, SPIE press, 2005, vol. 146.
- [6] U. Okoroanyanwu, *Chemistry and Lithography*, SPIE Press, 2010.
- [7] T. Kozawa and S. Tagawa, *Jpn. J. Appl. Phys.*, 2010, **49**, 030001.
- [8] T. Itani and T. Kozawa, *Jpn. J. Appl. Phys.*, 2012, **52**, 010002.
- [9] B. Cardineau, R. Del Re, H. Al-Mashat, M. Marnell, M. Vockenhuber, Y. Ekinci, C. Sarma, M. Neisser, D. A. Freedman and R. L. Brainard, *Proc. SPIE*, 2014, **9051**, 90511B.
- [10] D. De Simone, I. Pollentier and G. Vandenberghe, *J. Photopolym. Sci. Technol.*, 2015, **28**, 507–514.
- [11] H. Xu, K. Sakai, K. Kasahara, V. Kosma, K. Yang, H. C. Herbol, J. Odent, P. Clancy, E. P. Giannelis and C. K. Ober, *Chem. Mater.*, 2018, **30**, 4124–4133.
- [12] J. Kreutzer, M. Puchberger, C. Artner and U. Schubert, *Eur. J. Inorg. Chem.*, 2015, **2015**, 2145–2151.
- [13] P. Walther, M. Puchberger, F. R. Kogler, K. Schwarz and U. Schubert, *Phys. Chem. Chem. Phys.*, 2009, **11**, 3640–3647.
- [14] P. Kolodner, A. Katzir and N. Hartsough, *J. Vac. Sci. Technol. B*, 1983, **1**, 501–504.
- [15] S. Kimura and K. Takami, *Appl. Opt.*, 1988, **27**, 3675–3678.
- [16] T. Mizokuro, H. Mochizuki, N. Tanigaki, X. Mo, N. Yamamoto and T. Hiraga, *Jpn. J. Appl. Phys.*, 2005, **44**, L1449–L1451.
- [17] F. Ciardelli, G. Ruggeri and A. Pucci, *Chem. Soc. Rev.*, 2013, **42**, 857–870.
- [18] P. R. Sundararajan, *J. Polym. Sci., Part B: Polym. Phys.*, 2018, **56**, 451–478.
- [19] A. J. Berro, A. J. Berglund, P. T. Carmichael, J. S. Kim and J. A. Liddle, *ACS Nano*, 2012, **6**, 9496–9502.
- [20] L. Wu, M. Tiekink, A. Giuliani, L. Nahon and S. Castellanos, *J. Mater. Chem. C*, 2019, **7**, 33–37.
- [21] L. Wu, M. Baljovic, G. Portale, D. Kazazis, M. Vockenhuber, T. Jung, Y. Ekinci and S. Castellanos, *J. Micro/Nanolithogr., MEMS, MOEMS*, 2019, **18**, 013504.
- [22] R. Del Re, J. Passarelli, M. Sortland, B. Cardineau, Y. Ekinci, E. Buitrago, M. Neisser, D. A. Freedman and R. L. Brainard, *J. Micro/Nanolithogr., MEMS, MOEMS*, 2015, **14**, 043506.
- [23] E. C. Mattson, Y. Cabrera, S. M. Rupich, Y. Wang, K. A. Oyekan, T. J.

- Mustard, M. D. Halls, H. A. Bechtel, M. C. Martin and Y. J. Chabal, *Chem. Mater.*, 2018, **30**, 6192–6206.
- [24] G. Kickelbick and U. Schubert, *Chem. Ber.*, 1997, **130**, 473–477.
- [25] G.-S. Liou, S.-H. Hsiao, N.-K. Huang and Y.-L. Yang, *Macromolecules*, 2006, **39**, 5337–5346.
- [26] S.-H. Hsiao and Y.-T. Chiu, *RSC Adv.*, 2015, **5**, 90941–90951.
- [27] M. J. Frisch, G. W. Trucks, H. B. Schlegel, G. E. Scuseria, M. A. Robb, J. R. Cheeseman, G. Scalmani, V. Barone, G. A. Petersson, H. Nakatsuji, X. Li, M. Caricato, A. Marenich, J. Bloino, B. G. Janesko, R. Gomperts, B. Mennucci, H. P. Hratchian, J. V. Ortiz, A. F. Izmaylov, J. L. Sonnenberg, D. Williams-Young, F. Ding, F. Lipparini, F. Egidi, J. Goings, B. Peng, A. Petrone, T. Henderson, D. Ranasinghe, V. G. Zakrzewski, J. Gao, N. Rega, G. Zheng, W. Liang, M. Hada, M. Ehara, K. Toyota, R. Fukuda, J. Hasegawa, M. Ishida, T. Nakajima, Y. Honda, O. Kitao, H. Nakai, T. Vreven, K. Throssell, J. A. Montgomery, J. Peralta, J. E., F. Ogliaro, M. Bearpark, J. J. Heyd, E. Brothers, K. N. Kudin, V. N. Staroverov, T. Keith, R. Kobayashi, J. Normand, K. Raghavachari, A. Rendell, J. C. Burant, S. S. Iyengar, J. Tomasi, M. Cossi, J. M. Millam, M. Klene, C. Adamo, R. Cammi, J. W. Ochterski, R. L. Martin, K. Morokuma, O. Farkas, J. B. Foresman and D. J. Fox, *Gaussian 16, Revision A.03*, Gaussian, Inc., Wallingford CT, 2016.
- [28] D. Andrae, U. Haeussermann, M. Dolg, H. Stoll and H. Preuss, *Theor. Chim. Acta*, 1990, **77**, 123–141.
- [29] F. Weigend and R. Ahlrichs, *Phys. Chem. Chem. Phys.*, 2005, **7**, 3297–3305.
- [30] S. A. Campbell, *The Science and Engineering of Microelectronic Fabrication*, Oxford University Press, 1996.
- [31] G.-M. Tang, R.-H. Chi, W.-Z. Wan, Z.-Q. Chen, T.-X. Yan, Y.-P. Dong, Y.-T. Wang and Y.-Z. Cui, *J. Lumin.*, 2017, **185**, 1–9.
- [32] J. Kreutzler, P. Blaha and U. Schubert, *Comput. Theor. Chem.*, 2016, **1084**, 162–168.
- [33] W. Lao, C. Xu, S. Ji, J. You and Q. Ou, *Spectrochim. Acta, Part A*, 2000, **56**, 2049–2060.
- [34] Z. Ding, Q. Zhao, R. Xing, X. Wang, J. Ding, L. Wang and Y. Han, *J. Mater. Chem. C*, 2013, **1**, 786–792.
- [35] S. Liu, P. Lin, F. Niu, P. Zeng and B. Zhang, *Materials*, 2018, **11**, 617.
- [36] L. Hu, S. Liu, G. Xie, W. Yang and B. Zhang, *J. Mater. Chem. C*, 2020, **8**, 1002–1009.
- [37] S. M. Bonesi and R. Erra-Balsells, *J. Lumin.*, 2001, **93**, 51–74.
- [38] J. Passarelli, M. Murphy, R. Del Re, M. Sortland, L. Dousharm, M. Vockenhuber, Y. Ekinici, M. Neisser, D. A. Freedman and R. L. Brainard, *Proc. SPIE*, 2015, **9425**, 94250T.
- [39] A. Chapiro, *Radiat. Phys. Chem.*, 1979, **14**, 101–116.

- [40] J. F. Ambrose, L. L. Carpenter and R. F. Nelson, *J. Electrochem. Soc.*, 1975, **122**, 876.

Unravelling the effect of fluorinated ligands in hybrid EUV photoresists by X-ray spectroscopy*

Abstract

Organic-inorganic hybrid compounds are arising as promising resist materials for extreme-ultraviolet (EUV) lithography, a new technique introduced in the semiconductor industry for the fabrication of integrated circuits of sub-10 nm feature size. In this work, we show that the sensitivity to EUV radiation of zirconium oxo clusters with methacrylate ligands is substantially enhanced when a small fraction of the ligands are replaced by trifluoromethylacrylates. We studied the details of the chemical changes that occur in thin films of the precursor and the partially fluorinated materials using scanning transmission X-ray microscopy (STXM) and X-ray photoelectron spectroscopy (XPS). Evidence is presented for radical chain polymerization as a mechanism for the solubility switch. Yet, XPS results also indicate that Zr–F bonds are formed during the exposure to EUV light in the fluorinated material, dissociative electron attachment being likely involved. Our observations show that, while fluorinated ligands enhance EUV absorption, their effect on the reactivity of the material might be more critical, thereby contributing to an increase in the sensitivity of the resist in both ways.

*L. Wu, I. Bespalov, K. Witte, O. Lugier, J. Haitjema, M. Vockenhuber, Y. Ekinci, B. Watts, A. M. Brouwer, and S. Castellanos, "Unravelling the effect of fluorinated ligands in hybrid EUV photoresists by X-ray spectroscopy", *J. Mater. Chem. C*, 2020, DOI: 10.1039/d0tc03216f. The electronic supplementary information is available at <http://dare.uva.nl/en>.

7.1 Introduction

EUV lithography is a cutting-edge technology that can enable the fabrication of integrated circuits for computer chips and memory devices with feature sizes below 10 nm.^{1,2} Thanks to the employment of shorter wavelength (13.5 nm) than in previous lithographic techniques (193 nm), EUV lithography can yield a higher resolution. Yet, a challenge remains; to find photoresist materials that can efficiently absorb the EUV photons from the optical projection and transform them into high-quality nanopatterns after development.^{3–5}

Although photoresists based on polymeric platforms have been used in optical lithography until now, these materials are not optimal for EUV lithography for several reasons,⁶ one of the most important being their low EUV absorptivity.^{5,7} Therefore, finding new resists that fulfill the requirements for the fabrication of the next generation of integrated circuits is of paramount importance. EUV resists should be able to print high-quality patterns with feature sizes below 20 nm at cost-effective exposure times, that is, using low EUV doses (ideally < 20 mJ/cm²).^{8,9} Further, a low defect density in the patterns is required, an aspect that has been correlated to the EUV absorptivity of the resist. That is, high absorptivity reduces some type of defects in the final pattern.^{10,11} Heterogeneities in the composition of the resist film are also considered a source of defects,^{12,13} since they contribute to the stochastic distribution of chemical reactions around the photon absorption area.

Molecular materials that incorporate metals in their structures—typically known as inorganic resists—are gaining interest^{5,14,15} since they offer higher EUV absorption cross-sections and have yielded better nanopatterning performance compared to polymer-based ones.^{6,8,9} Yet, what makes the design of a novel EUV resist challenging is that the chemistry induced by EUV photons is not well understood.¹⁶ EUV photons, with the energy of 92 eV, do not initiate “classical” photochemistry, but rather eject electrons from the valence band or, when applicable, from some inner core orbitals to the continuum, leading to the ionization of the molecule. The ejected photoelectron has an excess of kinetic energy that is transferred to the surroundings through inelastic scattering events. During the scattering, more molecules can be ionized so that secondary electrons are generated, which have a broad distribution of kinetic energies in the 0–80 eV range.¹⁴ Therefore, the chemistry induced by EUV photons is the result of the electron-induced chemistry^{17–19} and the chemical processes that the ionized molecules undergo. Furthermore, the probability of absorbing EUV photons by molecules is mainly determined by their elemental composition rather than by the selection rules based on the characteristics of the frontier molecular orbitals that apply in photochemistry.^{7,20}

Metal oxo clusters (MOCs) are promising materials for the next generation of inorganic EUV resists. First, they comprise metals, which can significantly enhance the EUV absorptivity of the material, as explained above. Second, they are molecularly defined, meaning that they consist of molecular units of small size and thus offer homogeneity in their composition. Both characteristics are expected to benefit the lithographic performance in terms of roughness and defect density

in the patterns.^{12,13,21} And, third, in the case of MOCs comprising carboxylate ligands, the composition of their organic shell can be easily modified by means of ligand exchange reactions. This provides a quite straightforward manner of changing the properties of the layer (*e.g.*, density and processability) and its reactivity towards EUV light with small synthetic effort.^{22–24}

In this work, we introduce a small fraction of fluorinated methacrylate ligands in Zr-based resists that originally have an organic shell composed of solely methacrylate ligands. The incorporation of the fluorine species aimed at increasing the EUV absorptivity (and, in consequence, the sensitivity) of the material. As shown below, the “doping” of the organic shell²³ substantially enhances the material’s sensitivity in EUV lithography. The chemical changes resulting from EUV exposure in both materials were monitored by means of scanning transmission soft X-ray microscopy (STXM) and X-ray photoelectron spectroscopy (XPS). These techniques are especially convenient to study EUV resists, since they can be applied on very thin films (~ 30 nm thick) and give very specific information about changes in chemical bonding, *i.e.*, they can be used to elucidate what type of reactions occur in the thin film. It was found that, in addition to the cross-linking reactions between methacrylate ligands happening in both clusters, the presence of fluorinated ligands opened a new reaction path where C–F bonds are dissociated, thus making the fluorinated material more reactive towards EUV photons.

7.2 Experimental

7.2.1 Thin-film deposition and EUV exposure

The pristine $\text{Zr}_6\text{O}_4(\text{OH})_4\text{Mc}_{12}$, Mc = methacrylate, here labeled as **ZrMc**, was synthesized as previously reported.²⁵ A reaction mixture of **ZrMc** (5 mM) with one molar equivalent of trifluoromethyl acrylic acid (5 mM) was prepared in a mixed solvent of chloroform and propylene glycol methyl ether acetate (PGMEA), in a CHCl_3 :PGMEA ratio of 9:1 (v/v). The mixture was sonicated for 2 minutes and filtered through a $0.2 \mu\text{m}$ PTFE filter before spin-coating. The resist film containing the doped system **ZrMcF** was deposited by spin-coating at 2100 rpm for 30 seconds with an acceleration of 3000 rpm/s onto the substrate of choice. Three different types of substrates were used, depending on the experiment to be performed: (1) 30 nm thick SiN_x membranes with a window size of $2.5 \times 2.5 \text{ mm}^2$ supported by a Si frame ($7.5 \times 7.5 \text{ mm}^2$, $525 \mu\text{m}$ thick) purchased from Norcada for STXM; (2) Cr (*ca.* 2 nm thick)/Au (*ca.* 18 nm thick) coated Si chips ($10 \times 10 \text{ mm}^2$) for XPS; and (3) $20 \times 20 \text{ mm}^2$ Si substrates for the dose test (contrast curve) and line/space patterns. Thin films of **ZrMc** were prepared from a filtered solution (10 mg/mL) in CHCl_3 :PGMEA 9:1 (v/v), using the same spin-coating conditions as for **ZrMcF**. The thin films were exposed to EUV photons (92 eV with 4% bandwidth) at the XIL-II beamline of the Swiss Light Source (SLS) synchrotron at the Paul Scherrer Institute (PSI)²⁶ using an open-frame mask with an aperture size of $0.5 \times 0.5 \text{ mm}^2$ or of $1.7 \times 1.7 \text{ mm}^2$ for STXM

or XPS, respectively. Diffraction gratings on SiN_x membranes are used to create sinusoidal aerial images resulting in line/space patterns with different half-pitches.

7.2.2 Near edge X-ray absorption fine structure (NEXAFS)

NEXAFS investigations were performed *ex situ* at the PolLux beamline (X07DA) of the synchrotron radiation facility SLS at the PSI, using STXM with an energy resolution of $E/\Delta E > 3000$ for the 270–350 eV energy range.^{27–30} The NEXAFS measurements were performed under normal incidence in the “line-scan” mode in each region of interest with a length of 25 μm . On each position, the transmitted photon flux I was measured in an energy scan with varying energy step sizes for different regions of the spectrum (270–282 eV, 0.5 eV step; 282.1–293.0 eV, 0.2 eV step; 293.25–300.00 eV, 0.25 eV step; 301–350 eV, 1 eV step; dwell time 100 ms) was recorded. Repeating the measurement on the same location showed that there was no noticeable radiation damage. Reference measurements (I_0) were made on a blank membrane or on the clean areas of the developed samples. The absorbance is expressed as $A = \ln(I_0/I)$. The edge-step normalization and the spectra fitting were carried out using the Athena software package³¹. Pre-edge and post-edge normalizations were applied. For identification of the position and the amplitude of the peak resonances, the absorption spectra were fitted using several Gaussian line shapes and one step-function at the position of the ionization potential. The positions of the peaks were set according to the spectral features in the reference (not exposed) sample. The values for the ionization potential in the step function, the peaks centroids, as well as amplitudes and widths for the Gaussian line shapes of the exposed samples were set equal to those obtained from fitting of the reference sample.

7.2.3 X-ray photoelectron spectroscopy (XPS)

XPS measurements were performed *ex-situ* in a Scienta Omicron HiPP3 analyzer, with a monochromatic Al $K\alpha$ source (energy of 1486.7 eV). A survey spectrum was obtained with a pass energy of 200 eV and an energy step of 0.5 eV; a pass energy of 100 eV and energy step of 0.1 eV were employed for F 1s, O 1s, C 1s, and Zr 3d high-resolution spectra. Each spectrum was fitted as a convolution of Gaussian and Lorentzian line shapes using UNIFIT software in order to determine the concentration and components of every element.

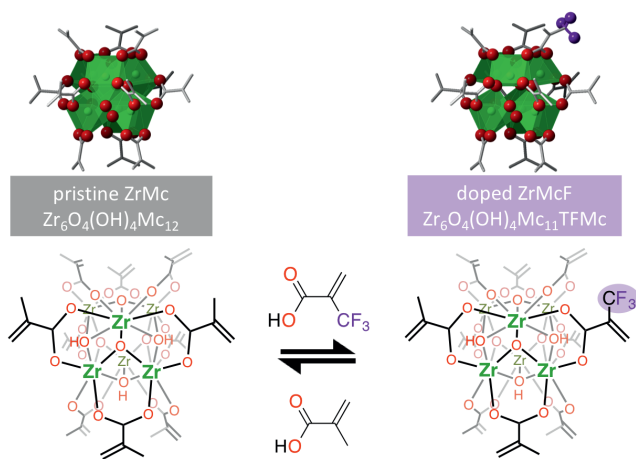
7.3 Results and Discussion

7.3.1 The effect of fluorinated ligands on resist sensitivity

Recently, the Zr-oxocluster comprising methacrylate ligands in the organic shell, $\text{Zr}_6\text{O}_4(\text{OH})_4\text{Mc}_{12}$, abbreviated as **ZrMc**, was proven to act as a negative tone EUV resist.³² The material rendered a relatively good sensitivity in terms of the minimum dose necessary to change the solubility in the solvent used to deposit thin

films of the pristine material (D_0). This dose is measured by means of contrast curves, an experiment in which the thickness of exposed resist remaining after development (for a fixed time) is measured for varying exposure doses. This gives evidence of changes in the solubility rate and, therefore, proof of chemical changes after exposure.³³ Despite the good sensitivity of the material, its linear absorbance at 92 eV is rather low (calculated $4.2 \mu\text{m}^{-1}$, experimental $5 \mu\text{m}^{-1}$).²⁰

Aiming at the enhancement in the EUV absorptivity of the material, a fluorinated version of the methacrylate ligand was introduced in the organic shell. Metal oxo clusters comprising carboxylate ligands undergo ligand exchange reactions with ligands that feature the same chelating groups. This allows for the easy modification of the composition of their organic shell.^{22–24,34,35} The incorporation of the fluorinated ligand was thus performed by means of ligand exchange reaction using a low ratio of fluorinated methacrylate ligands, TFMc, in relation to the methacrylate ligand, Mc, present in the original cluster (an average of 1 TFMc over 12 ligands). That is, we doped **ZrMc** with TFMc ligands to yield a mixture of clusters with an average molecular formula $\text{Zr}_6\text{O}_4(\text{OH})_4\text{Mc}_{11}\text{TFMc}$, here **ZrMcF** (Scheme 7.1). By doping the organic shell most of the physicochemical properties of the material, such as its processability in solvents, are preserved while the specific effect of the doping ligand in the lithographic performance can be tracked down. It should be noticed that the incorporation of the fluorinated ligand in the molecular structure even in such a small ratio can increase the linear



Scheme 7.1: Ligand exchange reaction on **ZrMc** to synthesize the doped **ZrMcF**. On top, 3D representations of the cluster made from the crystal X-ray diffraction data of the pristine **ZrMc**.²⁵ green octahedra represent the coordination geometry of Zr^{4+} cations, red spheres represent oxygen atoms, grey bars represent the carbon backbone of the ligands. Fluorine atoms were added for representation purposes. Protons in μ_3 -bridging OH groups of the oxo-cluster are omitted for simplicity.

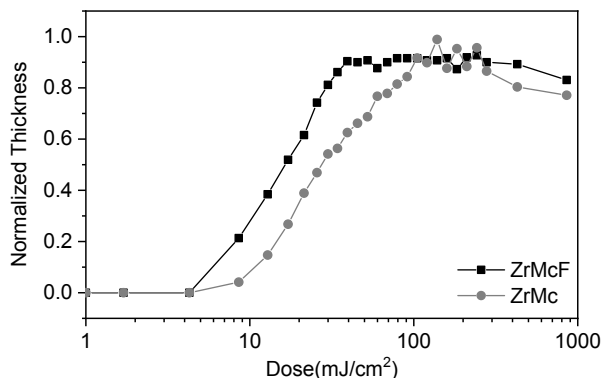


Figure 7.1: Contrast curves obtained for **ZrMc** and **ZrMcF** after exposure to EUV using an open-frame mask.

EUV absorptivity of the resist by 10%.³⁶

The pristine **ZrMc** and the doped **ZrMcF** compounds were deposited by means of spin-coating on silicon substrates. The thin films were exposed to EUV (synchrotron light at 92 eV) using an open-frame mask for large areas (aperture size of $1.7 \times 1.7 \text{ mm}^2$ or $0.5 \times 0.5 \text{ mm}^2$) or by means of interference lithography (EUV-IL)^{2,26,37} to print dense line/space patterns. The exposed thin films of both materials were subsequently developed using the same conditions (developer and development time). The contrast curves of the two resists indicate that the fluorinated material renders higher sensitivity (Fig. 7.1) and an improvement of the printability of dense lines pattern was observed; while **ZrMc** could only resolve dense lines of 50 nm width using a dose of 57 mJ/cm², **ZrMcF** could print 30 nm lines at 36 mJ/cm² (Fig. S7.2 in Supporting Information). It should be noticed that, the development conditions are not optimized for the doped material, as our main goal was to compare both resists.

7.3.2 NEXAFS

Previous works have proposed that metal oxoclusters based on Zr and Hf and comprising methacrylate ligands undergo cross-linking between the double bonds of neighboring molecules upon EUV exposure.^{32,38} This reaction is probably initiated by radicals that are generated after ionization. Here, NEXAFS spectroscopy was used to monitor the cross-linking reaction in both EUV resists. This technique is element-specific and gives information of the chemical bonding of the studied element since resonant transitions from the core atomic orbitals to empty molecular orbitals are selectively promoted.

In particular, NEXAFS spectroscopy was performed using scanning transmission soft X-ray microscopy (STXM).^{27,39} This technique enables recording X-ray absorption in the soft X-ray regime with a spatial resolution of down to 20 nm.

The combination of EUV exposure and *ex-situ* STXM analysis is thus a powerful way to investigate the chemical changes undergone by the resists upon EUV exposure. This is because different doses of EUV can be applied in different regions of the same sample, and changes in the X-ray absorption can then be mapped and correlated to each EUV dose. In particular, the soft X-ray energy range promotes electronic transitions from the carbon K-edge (1s orbital), which directly corresponds to the detection of changes in the carbon backbone of the organic ligands.^{40–42}

C K-edge NEXAFS spectroscopy was performed for the two materials, **ZrMc** and fluorine-doped **ZrMcF**. For each compound, a spectrum of the thin film before exposure to EUV light was recorded as reference (Fig. 7.2). The spectra of the unexposed thin films of both **ZrMc** and **ZrMcF** in Fig. 7.2 displayed clear, sharp peaks corresponding to electronic transitions from the C 1s orbital on the C=C terminal bond to the π^* orbital of the methacrylate ligand, C 1s $\rightarrow \pi^*(\text{C}=\text{C})$, at ~ 284 eV and to the electronic transitions from the 1s orbital of the C atom on the carboxylate group to the π^* orbital, C 1s $\rightarrow \pi^*(\text{C}=\text{O})$, at ~ 288 eV.^{40,43} The fits of the relevant peaks contributing to the NEXAFS spectra are shown in Fig. 7.2, and their assignments to electronic transitions are listed in Table 7.1.

The fits of both the peaks assigned to C 1s $\rightarrow \pi^*(\text{C}=\text{C})$ and the 1s $\rightarrow \pi^*(\text{C}=\text{O})$ transitions in **ZrMc** and **ZrMcF** required at least two components each

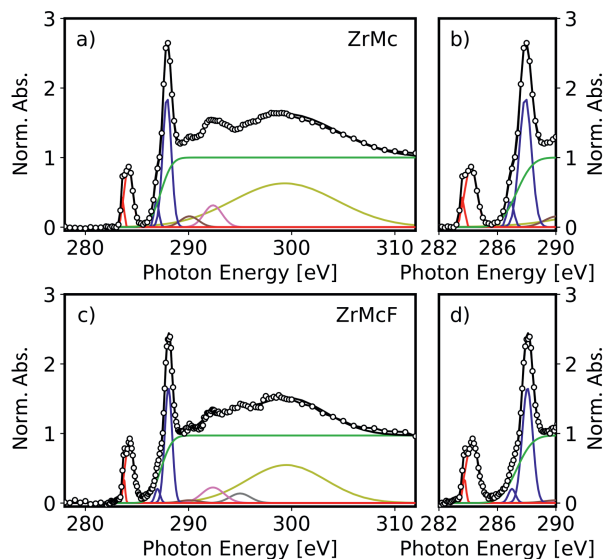


Figure 7.2: Fitted NEXAFS spectra of the C K-edge region **a)** of the **ZrMc** resist **(b)** zoomed-in range) and **c)** of the doped **ZrMcF** resist **(d)** zoomed-in range) before exposure. Gaussian peaks fit resonant transitions and the step-function (green line) fits the ionization to the continuum (edge).

Table 7.1: Assigned electronic transitions to the fitted components in the NEX-AFS spectra of **ZrMc** and **ZrMcF**

Energy (eV)	Assignment	Ref.
283.6, 284.2	C 1s \rightarrow π^* (C=C)	40
286.9, 287.9	C 1s \rightarrow π^* (C=O)	40,43
290.1	C 1s \rightarrow σ^* (C-H)	44
292.4	C 1s \rightarrow σ^* (C-H)	44
295.0	C 1s \rightarrow σ^* (C-F) ^a	45,46
299.5	C 1s \rightarrow σ^* (C-C)	44

^aOnly present in the spectrum of **ZrMcF**.

(Fig. 7.2). This could arise from different environments or coordination modes of the methacrylate ligands. As a matter of fact, in the crystalline form, the **ZrMc** cluster already presents two binding modes for the methacrylate ligands: chelating (one carboxylate group coordinates on Zr^{4+} cations) and bridging (one carboxylate group coordinates to two Zr^{4+} cations).²⁵ In addition, we suspect that the carboxylate ligands in the cluster rearrange when they are deposited as thin films, which would also lead to different binding modes and environments around the carboxylate groups.³² However, the exact origin of the different contributions to these peaks is outside the scope of this work.

Different areas on one sample (either containing **ZrMc** or **ZrMcF**) were exposed to four different EUV doses (50, 100, 200, and 500 mJ/cm^2) and each sample was developed, as represented in Fig. 7.3a. The spectra from the four non-dissolved features were then recorded with STXM. Fig. 7.3b displays the evolution of the C K-edge absorption spectra of both materials normalized to the continuum at ~ 320 eV after EUV exposure. Note that the absorbance in the ionization regime is a measure of the total amount of carbon present. Therefore, this normalization allows monitoring the proportion of carbon species of interest relative to the total carbon contents. Overlapping with the C K-edge continuum, two peaks at 333.8 eV and 346.5 eV were also detected (Fig. S7.4). These peaks belong to the Zr $M_{2,3}$ -edge, *i.e.* they originate from excitations of Zr 3p electrons. Although the analysis of this absorption edge is beyond the scope of the present work, we noted that the intensity of the peaks in the normalized spectra was constant over dose.

Further trends that support chemical changes in the ligands rather than just their cleavage and loss is the evolution of the 290–310 eV region, where the C 1s \rightarrow σ^* (C-H/C-C) transitions occur. Although an explanation of the spectral shape evolution is non-trivial and not attempted here, we observed that the spectra of **ZrMc** and **ZrMcF** at the highest dose (500 mJ/cm^2) closely resemble the C K-edge spectrum of polymethylmethacrylate (PMMA), which is the product of polymerization of methyl methacrylate (see Fig. S7.5 in Supporting Information). This resemblance is in agreement with the formation of some kind of Zr-containing hybrid polymer after **ZrMc** and **ZrMcF** are exposed to EUV light.

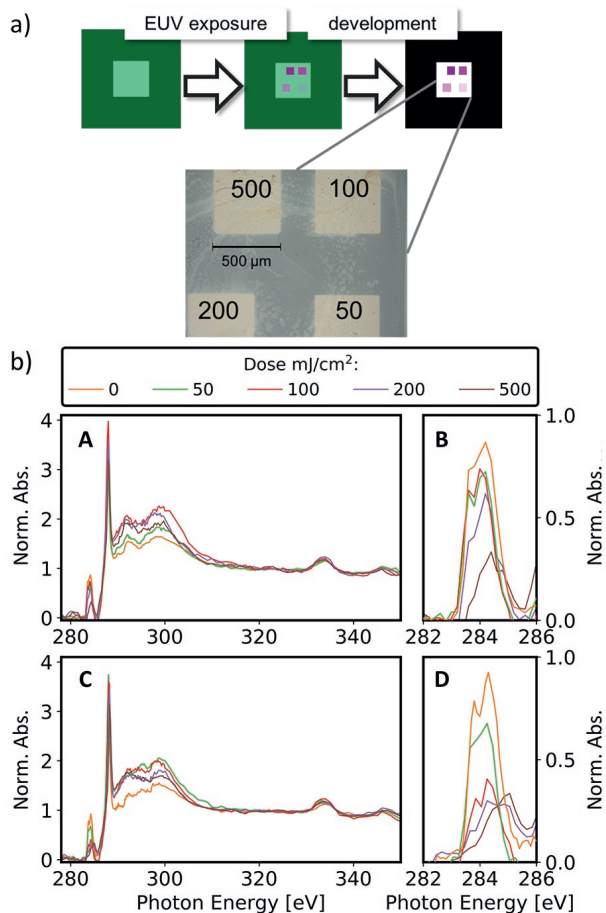


Figure 7.3: a) Scheme showing the workflow for the experiment. The resists were spin-coated on SiN_x membranes and exposed to EUV. Then, the samples were developed so that the unexposed material was selectively dissolved and the clean membrane was left between exposed areas. An optical microscope image of the sample after development is shown. EUV doses on each squared area are given in mJ/cm². b) NEXAFS spectra of **ZrMc** (A & B) and **ZrMcF** (C & D) before and after exposure normalized to the continuum. C and D zoom into the pre-edge region with the absorption peak assigned to C 1s → π* (C=C) transition.

A clear decrease of the C 1s → π* (C=C) peak with increasing EUV exposure dose is observed for both materials (Fig. 7.4a). Furthermore, the absorbance ratio between the peaks assigned to C=C and the ones assigned to the COO ($A_{C=C}/A_{C=O}$ in Fig. 7.4b) also decreases with EUV exposure. This indicates that methacrylate ligands are not just cleaved and outgassed but also the concentration of C=C double bonds decreases through another process. These results are in agreement with the cross-linking mechanism proposed for the **ZrMc** material in

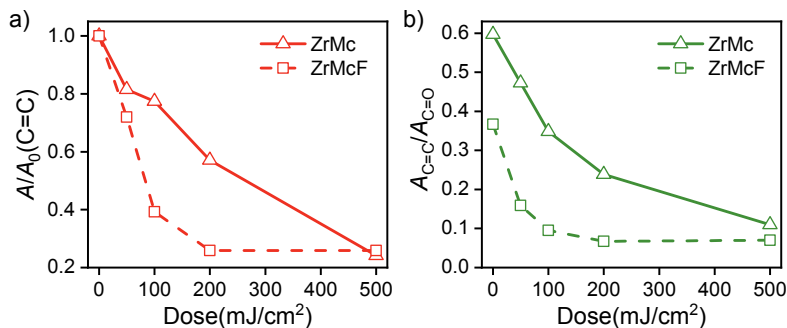


Figure 7.4: Evolution of the absorbance value (A) of some fitted peaks in normalized spectra as a function of dose. **a)** Absorbance of peaks assigned to C 1s $\rightarrow \pi^*$ (C=C) ($A_{283.6} + A_{284.2}$) relative to initial values (A/A_0); **b)** Absorbance ratio between peaks assigned to C 1s $\rightarrow \pi^*$ (C=C) ($A_{283.6} + A_{284.2}$) and to C 1s $\rightarrow \pi^*$ (C=O) ($A_{286.9} + A_{287.9}$).

previous works:^{32,38} Radical species resulting from ionization can lead to chain polymerization reactions among neighboring methacrylate ligands, thus decreasing the C=C concentration in the material.

It should be noted that a small amount of decarboxylation upon EUV exposure (< 20%) was reported for **ZrMc** in a previous work³² based on XPS studies (see below for XPS on **ZrMcF**). Yet, in NEXAFS, the C 1s $\rightarrow \pi^*$ (C=O) peak showed a two-step behavior with an initial increase and a subsequent decrease for doses above 100 mJ/cm² (Fig. S7.6 in Supporting Information) for both materials. It should be kept in mind that the increase in the peak is relative to the continuum. So, this could indicate that other carbon species contributing to the continuum are lost while few decarboxylation events occur. In addition, the intensity of the C 1s $\rightarrow \pi^*$ (C=O) peak can change depending on the functional groups that are next to the COO unit. In particular, this transition is lower when π systems are conjugated to the COO group compared to aliphatic groups.⁴⁷ Therefore, cross-linking reactions at lower doses might lead to an increase in the C 1s $\rightarrow \pi^*$ (C=O) peak intensity, whereas a slight amount of decarboxylation at higher doses can lead to its decrease. It should also be noted that XPS probes only the surface of the thin film, whereas NEXAFS experiments, performed in transmission mode, probe the whole film. The fraction of COO groups that are lost in the bulk is probably below 20%.

We observed that the decrease in the C=C/COO absorbance ratio was faster in the case of the F-doped material, **ZrMcF**, compared to the case of **ZrMc** (Fig. 7.4b), thus indicating that a larger number of reactions per incident photon occurs in the doped compound compared to the non-fluorinated **ZrMc**. Although **ZrMcF** is expected to have a slightly higher linear absorptivity, the increase is calculated as only 10% (4.2 vs. $4.6 \mu\text{m}^{-1}$),³⁶ which does not explain the remarkable difference in reactivity between the two compounds. The differences in the cross-

linking reaction efficiency are in line with the trends observed for the sensitivity of the two materials. As explained above, **ZrMcF** proved to need less EUV dose to render the whole thin film insoluble in the contrast curves.

7.3.3 X-ray photoelectron spectra

To gain further insights into the role of the fluorine-containing ligand in the EUV-induced chemistry of **ZrMcF**, XPS was used to track changes in this element. The spectra in the F 1s region (Fig. 7.5a) revealed the clear appearance of a new fluorine species upon EUV irradiation. The chemical shift for this species is typical for inorganic fluoride.^{48,49} This peak increases as a function of dose (empty green triangles in Fig.7.5b), while, at the same time, the F 1s peak assigned to fluorine bonded to carbon originally present in the fluorinated ligand, decreases (filled

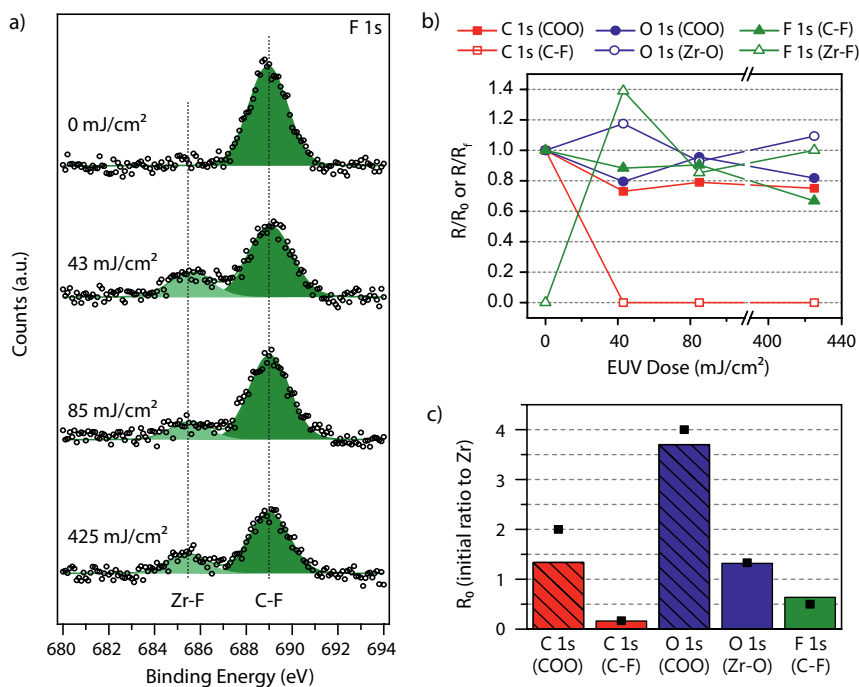


Figure 7.5: **a)** High-resolution XPS of the F 1s peak of the unexposed and the exposed **ZrMcF** resist; experimental data plotted in circles, fitted components shown in green areas. **b)** Species ratio relative to Zr (R) at each EUV dose expressed as a fraction of the initial ratio (R/R_0) and, in the case of the appearing Zr-F species in F 1s, as a fraction of the final ratio (R/R_f). **c)** Species ratio relative to Zr of the **ZrMcF** unexposed thin film (R_0) calculated from the fitting of C 1s, O 1s and F 1s peaks in the X-ray photoelectron spectra (bars) and theoretical ratios calculated from the molecular formula (black squares).

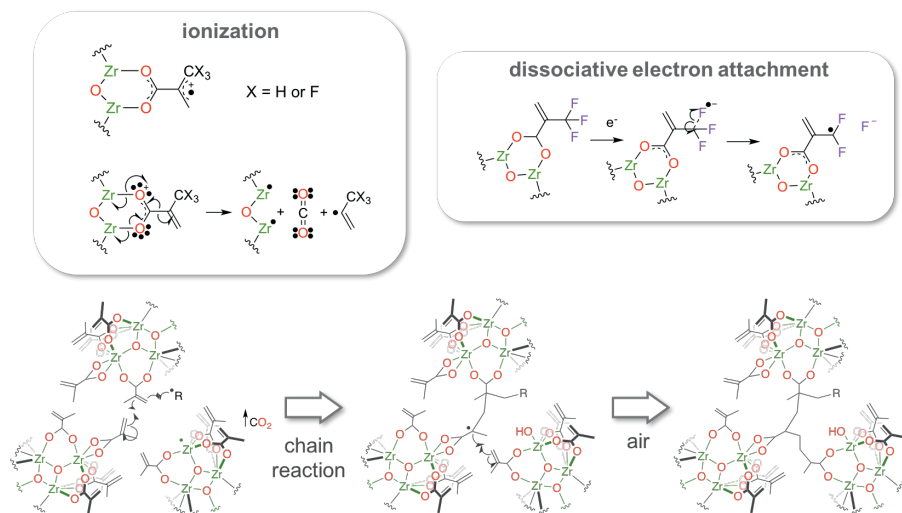
green triangles in Fig. 7.5b). It is known that low energy electrons can easily lead to dissociation of C–F bonds.^{50,51} This result thus indicates that the C–F bond is dissociated, and the resulting fluoride ion is stabilized in the material, most likely through the interaction with the metal cations by forming Zr–F bonds. In fact, this particular hexanuclear Zr-clusters has shown affinity for F[−] ions when they are constituents (nodes) of a metal-organic framework,⁵² and related ZrO_x particles decorated with carboxylate ligands have been used to remove F[−] ions from water.⁵³

For O 1s and C 1s spectra, the evolution of the peak profile followed the trends previously reported for **ZrMc**.³² The fitting of the O 1s peak (Fig. S7.7) suggests a slight decrease of oxygen species from carboxylate groups (531 eV, filled blue circles in Fig. 7.5b) and a concomitant increase of the oxide-type species (530 eV, empty blue circles in Fig. 7.5b). This is in line with a small number of decarboxylation reactions followed by the oxidation/hydroxylation of the Zr-sites after EUV exposure in the presence of air, since the measurements were done *ex-situ*. The slight loss of carboxylate groups is also in agreement with the small decrease of the peak at 289 eV (red squares in Fig. 7.5b) observed in the fitting of the C 1s peak in the XPS spectra (Fig. S7.7). Yet, **ZrMcF** displayed a new peak in the C 1s spectrum at 292.4 eV compared to the spectrum of **ZrMc**, which is assigned to the carbon atoms participating in the C–F bond of the fluorinated ligands. Unfortunately, accurate tracking of this peak as a function of dose is not possible due to its low intensity. Yet, the spectra indicate a decrease of this species with exposure.

Therefore, in addition to a higher degree of cross-linking per incident EUV photon, **ZrMcF** undergoes an extra reaction where C–F bonds are cleaved and fluoride species are formed. In fact, it is likely that such cleavage further induces polymerization reactions as it can result in the formation of transient radicals that initiate the cross-linking of the double bonds. The EUV-induced reactions for ZrMcF are shown in Scheme 7.2. Partial decarboxylation, ligand cross-linking and the intercalation of fluorine atoms in the resulting network lead to the solubility contrast in **ZrMcF**.

7.4 Conclusion

The doping of the organic shell of a Zr-based oxo cluster composed of methacrylate ligands with an analogous fluorinated ligand (trifluoromethacrylate) led to the enhancement of EUV lithographic performance. NEXAFS experiments in the C K-edge energy range revealed that the concentration of terminal double bonds in both the pristine material and the partially fluorinated analogue decreases at faster rates than the concentration of carboxylate groups upon EUV radiation. This trend is in line with a polymerization reaction involving the terminal double bonds of the methacrylate ligands, which would result in a decrease in the solubility of the clusters upon EUV exposure and would thus enable the formation of patterns with EUV lithography. The evolution of the X-ray absorption spectra



Scheme 7.2: Reactions induced by EUV that lead to the formation of radicals which can initiate cross-linking of the terminal double bonds in the methacrylate ligands.

with incident dose points at a more efficient reaction in the fluorine-containing material compared to the undoped one, *i.e.* more double bonds react for the same incident dose. Furthermore, X-ray photoelectron spectroscopy indicates that an extra reaction pathway takes place in the doped resist: the dissociation of C–F bond and formation of inorganic fluoride, presumably stabilized by the formation of Zr–F bonds. We thus attribute the better printability of the material doped with fluorinated ligands to the synergistic contribution of two factors: a slightly higher EUV absorptivity and the appearance of a new reaction pathway where C–F bonds are cleaved. The latter could be a source of radical species that further initiate the cross-linking reactions, which leads to a new product comprising fluoride ions. This work shows how a simple modification in the molecular structure of a hybrid material can result in a significant optimization of the material as an EUV resist. Mainly, the introduction of different functionalities in the organic shell of this type of materials can open new reaction channels originating from the ionization of the molecules and/or from their interaction with low energy electrons.

Bibliography

- [1] R. M. M. Hasan and X. Luo, *Nanomanuf. Metrol.*, 2018, **1**, 67–81.
- [2] B. Päivänranta, A. Langner, E. Kirk, C. David and Y. Ekinici, *Nanotechnology*, 2011, **22**, 375302.
- [3] A. Lio, *Proc. SPIE*, 2016, **9776**, 97760V.
- [4] R. A. Lawson and A. P. Robinson, *Frontiers of Nanoscience*, Elsevier, 2016, vol. 11, pp. 1–90.
- [5] L. Li, X. Liu, S. Pal, S. Wang, C. K. Ober and E. P. Giannelis, *Chem. Soc. Rev.*, 2017, **46**, 4855–4866.
- [6] X. Wang, Z. Tasdemir, I. Mochi, M. Vockenhuber, L. van Lent-Protasova, M. Meeuwissen, R. Custers, G. Rispens, R. Hoefnagels and Y. Ekinici, *Proc. SPIE*, 2019, **10957**, 109570A.
- [7] R. Fallica, J. K. Stowers, A. Grenville, A. Frommhold, A. P. G. Robinson and Y. Ekinici, *J. Micro/Nanolithogr., MEMS, MOEMS*, 2016, **15**, 033506.
- [8] D. De Simone, V. Rutigliani, G. Lorusso, P. De Bisschop, Y. Vesters, V. B. Carballo and G. Vandenberghe, *Proc. SPIE*, 2018, **10583**, 105830G.
- [9] D. De Simone, P. Vanelderen and G. Vandenberghe, *J. Photopolym. Sci. Technol.*, 2017, **30**, 613–617.
- [10] H. Fukuda, *Proc. SPIE*, 2019, **11147**, 1114716.
- [11] H. J. Levinson and T. A. Brunner, *Proc. SPIE*, 2018, **10809**, 1080903.
- [12] A. De Silva, L. Meli, D. L. Goldfarb and N. M. Felix, *Proc. of SPIE*, 2019, **10957**, 109570F.
- [13] R. Maas, M.-C. van Lare, G. Rispens and S. F. Wuister, *J. Micro/Nanolithogr., MEMS, MOEMS*, 2018, **17**, 041003.
- [14] P. D. Ashby, D. L. Olynick, D. F. Ogletree and P. P. Naulleau, *Adv. Mater.*, 2015, **27**, 5813–5819.
- [15] C. Luo, C. Xu, L. Lv, H. Li, X. Huang and W. Liu, *RSC Adv.*, 2020, **10**, 8385–8395.
- [16] A. Narasimhan, L. Wisheart, S. Grzeskowiak, L. E. Ocola, G. Denbeaux and R. L. Brainard, *J. Photopolym. Sci. Technol.*, 2017, **30**, 113–120.
- [17] R. T. Frederick, J. T. Diulus, D. C. Hutchison, M. Nyman and G. S. Herman, *ACS Appl. Mater. Interfaces*, 2019, **11**, 4514–4522.
- [18] J. T. Diulus, R. T. Frederick, M. Li, D. C. Hutchison, M. R. Olsen, I. Lyubnitsky, L. Árnadóttir, E. L. Garfunkel, M. Nyman, H. Ogasawara and G. S. Herman, *ACS Appl. Mater. Interfaces*, 2018, **11**, 2526–2534.
- [19] I. Bepalov, Y. Zhang, J. Haitjema, R. M. Tromp, S. J. van der Molen, A. M. Brouwer, J. Jobst and S. Castellanos, *ACS Appl. Mater. Interfaces*, 2020, **12**, 9881–9889.
- [20] R. Fallica, J. Haitjema, L. Wu, S. Castellanos, , A. M. Brouwer and Y. Ekinici, *J. Micro/Nanolithogr., MEMS, MOEMS*, 2018, **17**, 023505.
- [21] H. Xu, K. Sakai, K. Kasahara, V. Kosma, K. Yang, H. C. Herbol, J. Odent,

- P. Clancy, E. P. Giannelis and C. K. Ober, *Chem. Mater.*, 2018, **30**, 4124–4133.
- [22] L. Wu, J. Liu, M. Vockenhuber, Y. Ekinici and S. Castellanos, *Eur. J. Inorg. Chem.*, 2019, **2019**, 4136–4141.
- [23] L. Wu, M. Tiekink, A. Giuliani, L. Nahon and S. Castellanos, *J. Mater. Chem. C*, 2019, **7**, 33–37.
- [24] N. Thakur, L.-T. Tseng, M. Vockenhuber, Y. Ekinici and S. Castellanos, *J. Micro/Nanolith. MEMS MOEMS*, 2019, **18**, 043504.
- [25] G. Kickelbick and U. Schubert, *Chem. Ber.*, 1997, **130**, 473–477.
- [26] N. Mojarad, J. Gobrecht and Y. Ekinici, *Microelectron. Eng.*, 2015, **143**, 55–63.
- [27] J. Raabe, G. Tzvetkov, U. Flechsig, M. Böge, A. Jaggi, B. Sarafimov, M. G. C. Vernooij, T. Huthwelker, H. Ade, D. Kilcoyne, T. Tyliczszak, R. H. Fink and C. Quitmann, *Rev. Sci. Instrum.*, 2008, **79**, 113704.
- [28] B. Watts, S. Finizio, K. Witte, M. Langer, S. Mayr and S. Wintz, *Microsc. Microanal.*, 2018, **24**, 476–477.
- [29] U. Frommherz, J. Raabe, B. Watts, R. Stefani and U. Ellenberger, *AIP Conf. Proc.*, 2010, **1234**, 429–432.
- [30] U. Flechsig, C. Quitmann, J. Raabe, M. Böge, R. Fink and H. Ade, *AIP Conf. Proc.*, 2007, **879**, 505–508.
- [31] B. Ravel and M. Newville, *J. Synchrotron Radiat.*, 2005, **12**, 537–541.
- [32] L. Wu, M. Baljovic, G. Portale, D. Kazazis, M. Vockenhuber, T. Jung, Y. Ekinici and S. Castellanos, *J. Micro/Nanolithogr., MEMS, MOEMS*, 2019, **18**, 013504.
- [33] C. A. Mack, *J. Electrochem. Soc.*, 1987, **134**, 148–152.
- [34] J. Kreuzer, M. Puchberger, C. Artner and U. Schubert, *Eur. J. Inorg. Chem.*, 2015, **2015**, 2145–2151.
- [35] V. Guillerm, S. Gross, C. Serre, T. Devic, M. Bauer and G. Férey, *Chem. Commun.*, 2010, **46**, 767–769.
- [36] L. Wu, M. Vockenhuber, Y. Ekinici and S. Castellanos, *Proc. SPIE*, 2019, **10957**, 109570B.
- [37] N. Mojarad, D. Fan, J. Gobrecht and Y. Ekinici, *Opt. Lett.*, 2014, **39**, 2286–2289.
- [38] E. C. Mattson, Y. Cabrera, S. M. Rupich, Y. Wang, K. A. Oyekan, T. J. Mustard, M. D. Halls, H. A. Bechtel, M. C. Martin and Y. J. Chabal, *Chem. Mater.*, 2018, **30**, 6192–6206.
- [39] K. Witte, I. Mantouvalou, R. Sánchez-De-Armas, H. Lokstein, J. Lebendig-Kuhla, A. Jonas, F. Roth, B. Kanngießner and H. Stiel, *J. Phys. Chem. B*, 2018, **122**, 1846–1851.
- [40] R. Fallica, B. Watts, B. Rösner, G. Della Giustina, L. Brigo, G. Brusatin and Y. Ekinici, *Nanotechnology*, 2018, **29**, 36LT03.

- [41] G. K. Belmonte, C. A. da Silva Moura, P. G. Reddy, K. E. Gonsalves and D. E. Weibel, *J. Photochem. Photobiol., A*, 2018, **364**, 373–381.
- [42] C. A. da Silva Moura, G. K. Belmonte, P. G. Reddy, K. E. Gonsalves and D. E. Weibel, *RSC Adv.*, 2018, **8**, 10930–10938.
- [43] J. Kikuma and B. P. Tonner, *J. Electron Spectrosc. Relat. Phenom.*, 1996, **82**, 53–60.
- [44] O. Dhez, H. Ade and S. G. Urquhart, *J. Electron Spectrosc. Relat. Phenom.*, 2003, **128**, 85–96.
- [45] M. M. Brzhezinskaya, V. M. Morilova, E. M. Baitinger, S. E. Evsyukov and L. A. Pesin, *Polym. Degrad. Stab.*, 2014, **99**, 176–179.
- [46] G. R. Chagas, V. S. V. Satyanarayana, F. Kessler, G. K. Belmonte, K. E. Gonsalves and D. E. Weibel, *ACS Appl. Mater. Interfaces*, 2015, **7**, 16348–16356.
- [47] S. G. Urquhart and H. Ade, *J. Phys. Chem. B*, 2002, **106**, 8531–8538.
- [48] S. G. Rosenberg, M. Barclay and D. H. Fairbrother, *ACS Appl. Mater. Interfaces*, 2014, **6**, 8590–8601.
- [49] Y. Kawamoto, K. Ogura, M. Shojiya, M. Takahashi and K. Kadono, *J. Fluor. Chem.*, 1999, **96**, 135–139.
- [50] M. Orzol, T. Sedlako, R. Balog, J. Langer, G. P. Karwasz, E. Illenberger, A. Lafosse, M. Bertin, A. Domaracka and R. Azria, *Int. J. Mass Spectrom.*, 2006, **254**, 63–69.
- [51] J. Langer, M. Stano, S. Gohlke, V. Foltin, S. Matejcik and E. Illenberger, *Chem. Phys. Lett.*, 2006, **419**, 228–232.
- [52] X. Li, H. Zhang, P. Wang, J. Hou, J. Lu, C. D. Easton, X. Zhang, M. R. Hill, A. W. Thornton, J. Z. Liu, B. D. Freeman, A. J. Hill, L. Jiang and H. Wang, *Nat. Commun.*, 2019, **10**, 2490.
- [53] L. H. Velazquez-Jimenez, R. H. Hurt, J. Matos and J. R. Rangel-Mendez, *Environ. Sci. Technol.*, 2014, **48**, 1166–1174.

Fluorine-rich zirconium oxo clusters with enhanced EUV absorptivity for nanopatterning*

Abstract

The high transparency of Zr towards EUV photons (92 eV) limits the lithographic performance of inorganic-organic hybrid photoresist materials based on this element. In this chapter, a zirconium oxo cluster with fluorine-rich ligands (denoted as ZrTFMc) was prepared in order to increase the EUV absorptivity of the photoresist. Different solvents were tested as developers for contrast optimization. With methyl isobutyl carbinol (MIBC) as the developer, ZrTFMc provided high sensitivity showing the solubility switch at a dose of around 12 mJ/cm² and contrast factor of 3.3. This fluorinated photoresist rendered higher resolution of line-space patterns compared to its non-fluorinated analog. In addition, the resist sensitivity for dense line patterning proved to be strongly affected by the post-exposure baking process, as the dose-to-size could be improved from ~70 mJ/cm² to ~30 mJ/cm² by applying it. The chemical changes of ZrTFMc after EUV exposure and baking were investigated via Fourier transform infrared (FTIR) and UV-visible absorption spectroscopy. This work explores an approach to improve the EUV absorbance and lithographic performance of hybrid photoresist materials with a selected ligand, which can be applicable for other hybrid materials.

*L. Wu, D. Kazazis, Y. Ekinici, and S. Castellanos, "Fluorine-rich zirconium oxo clusters with enhanced EUV absorptivity for nanopatterning", manuscript in preparation. The electronic supplementary information is available at <http://dare.uva.nl/en>.

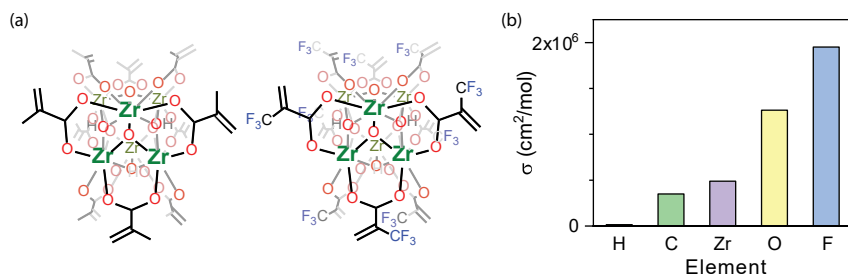
8.1 Introduction

Metal-containing inorganic-organic hybrid materials offer enhanced EUV absorptivity and high etching resistance, compared to conventional polymer-based organic photoresists and therefore they have attracted the interest of researchers as promising EUV photoresists.¹⁻⁴ Metal oxo clusters (MOCs) in particular, provide a platform at molecular level to investigate the reactions that different organic ligands and metal-oxo cores undergo upon EUV irradiation.⁵⁻⁷ One important role of the metallic elements in MOCs is to increase the EUV absorptivity in order to improve the lithographic performance. However, in $\text{Zr}_6\text{O}_4(\text{OH})_4(\text{OMc})_{12}$ (denoted as ZrMc), despite showing good sensitivity as negative-tone EUV resist in contrast curve experiments, the absorbance contribution from the Zr atoms is less than 5%.^{6,8} As a consequence, the absorptivity of Zr-based MOCs cannot compete with other hybrid resists containing metals with high absorption cross-section.^{9,10} The lithographic performance of Zr-based MOC materials is thus hindered by their low EUV absorptivity.

In Chapters 3 and 7, we have demonstrated the effect of introducing a fluorinated ligand into the model EUV photoresist ZrMc on the sensitivity and reactivity of the material, respectively. The detected enhancement induced by the fluorinated ligand suggests that fluorine-rich metal oxo clusters can potentially provide better EUV lithographic performance.

Fluorine-rich photoresists have been studied in the past for different reasons. For example, fluorinated photoresists in ArF (193 nm) immersion lithography can provide a hydrophobic surface for the interface with water.^{11,12} Other examples include fluoropolymer chemically amplified photoresists in 157 nm lithography. In this type of resist, the selective excitation of the photoacid generators embedded in the polymer is required. Since fluoropolymers show low absorbance at this wavelength, they act as an ideal matrix for the photoacid generators.¹³⁻¹⁶ In contrast, fluorinated polymers have been considered in chemically amplified EUV photoresists for the opposite purpose—increasing absorptivity of EUV. Yet, the photoacid generation efficiency can decrease with the presence of the fluorinated units.^{17,18}

In this work, we modified the model molecule ZrMc by replacing the methacrylate ligands with a fluorinated analogue 2-(trifluoromethyl)acrylate (TFMc) in order to increase EUV absorptivity of the photoresist material (Scheme 8.1). The EUV absorptivity of the fluorinated Zr-MOC is expected to be much enhanced with up to 36 F atoms in twelve ligands per molecule. We tested this sensitivity and patterning performance of synthesized ZrTFMc photoresist with different developers and post-exposure bake (PEB) temperatures. We monitored the spectroscopic changes in Fourier transform infrared (FTIR) and UV-visible absorption spectra of ZrTFMc after EUV exposure in order to gain insights into the mechanisms triggered by EUV light and by post-exposure baking in this new material.



Scheme 8.1: (a) Schematic presentation of the molecular structures of ZrMc and the fluorinated analog ZrTFMc. (b) Atomic photoabsorption cross section at 92 eV of elements in the studied material.¹⁹

8.2 Experimental

8.2.1 Synthesis

General Remarks. Reagents and solvents were purchased from Sigma-Aldrich and all dried with molecular sieves before use. ¹H and ¹⁹F NMR experiments were performed on Bruker Avance spectrometers (500 MHz and 300 MHz, respectively). FTIR spectra of bulk samples were recorded with a Bruker ALPHA-II FTIR spectrometer (resolution = 4 cm⁻¹). Solubility test was performed with 3–5 mg sample adding two drops up to 1.5 mL of solvent.

Synthesis of Zr₆O₄(OH)₄(OAc)₁₂ (ZrAc). ZrAc was synthesized by a method similar to the preparation of Zr₆O₄(OH)₄(OMc)₁₂²⁰ using acetic acid instead of methacrylic acid. To a solution of Zr(OiPr)₄ in 1-propanol (70 wt.%, 2 mL, 4.5 mmol) was added dropwise glacial acetic acid (1.0 mL, 17.8 mmol) under stirring in a flask under nitrogen. The reaction mixture was stored at room temperature for 2 days. Colorless crystals were isolated by decanting the mother liquid and dried under vacuum. IR absorptions (ATR, $\tilde{\nu}$, cm⁻¹): 464 (ρ COO, in-plane), 575–722 (δ COO, out-of-plane and ν Zr–O), 953 (ν C–C), 1024 (ρ CH₃), 1255 (ν C–O), 1290–1493 (CH₃ deformation and ν COO, symmetric), 1540 (ν COO, asymmetric), 1713 (ν C=O), 2932 (ν C–H aliphatic), 3013 (ν C–H aliphatic), 3083 (ν C–H aliphatic), and 2700–3700 (ν OH).^{21,22} Elemental analysis calculated for C₂₄H₄₀O₃₂Zr₆: C 20.77, H 2.91, O 36.89, Zr 39.44, found: C 20.70, H 2.89, Zr 39.30.

Synthesis of ZrTFMc from ZrAc. To a suspension of 540 mg ZrAc (0.4 mmol, 1.0 eqv.) in 10 mL DCM, 640 mg TFMAA (4.6 mmol, 11.7 eqv.) was added. The mixture was sonicated for 10 minutes and became a homogeneous solution. The solvent was removed under vacuum and the product was washed with heptane and pentane in sequence. ¹H NMR (σ , ppm, in CDCl₃, 25 °C): 6.68 (s, 1H), 6.34 (s, 1H) and 1.98 (s, 0.36H in acetate ligand). The chemical formula of the product can thus be estimated as Zr₆O₄(OH)₄(OTFMc)_{10.7}(OAc)_{1.3} on av-

erage. ^{19}F NMR (ppm, in CDCl_3 , 25 °C): -65.75 (s). IR absorptions (ATR, $\tilde{\nu}$, cm^{-1}): 465 (ρ COO, in-plane), 590–722 (δ COO, out-of-plane and ν Zr–O), 994 (ρ CH_2), 1068–1208 (ν C–F), 1250 (ν C–O), 1323 (ρ C–C=C and ν C–O), 1342–1500 (ν COO, symmetric), 1500–1636 (ν COO, asymmetric), 1660 (ν C=C), 1715 (ν C=O), 2700–3600 (ν OH and = CH_2), and 3637 (ν μ_3 -OH). Elemental analysis calculated for $\text{C}_{48}\text{H}_{28}\text{F}_{36}\text{O}_{32}\text{Zr}_6$: C 24.55, H 1.20, F 29.13, O 21.80, Zr 23.31. Found: C 23.54, H 1.18, F 28.13, Zr 22.37.

8.2.2 Thin film deposition

ZrTFMc was dissolved in 1:1 (v/v) ethyl acetate: chloroform solution (15 mg/mL). The solution was sonicated for 2 minutes and filtered before spin-coating. With 2000 rpm spinning speed (3000 rpm/s acceleration) applied for 30 seconds, the thickness of the spin-coated thin films is 38–40 nm, measured on a KLA Tencor Profiler P7. Samples were deposited on Si wafers ($525 \pm 25 \mu\text{m}$ in thickness) for lithographic tests, on quartz substrates ($500 \pm 20 \mu\text{m}$) for UV-visible absorption measurements, double-side polished Si substrates ($200 \pm 10 \mu\text{m}$) for FTIR spectroscopy and Au (18 nm)/Cr (2 nm) coated Si substrates for X-ray photoelectron spectroscopy.

8.2.3 EUV exposure and post-exposure characterization

The spin-coated thin films were exposed to EUV light (92 eV) at the XIL-II beamline of the Swiss Light Source at the Paul Scherrer Institute. Open-frame exposures were conducted for sensitivity (contrast curve) and spectroscopic studies. ZrTFMc thin films ($20 \times 20 \text{ mm}^2$) were exposed to 20, 50, and 200 mJ/cm^2 at different spots (exposure area of $6.8 \times 6.8 \text{ mm}^2$) and characterized with FTIR and UV-visible absorption spectroscopy. The unexposed areas were used to record the corresponding reference spectra. Samples for nanopatterning tests were exposed using EUV interference lithography through a mask with designed dense lines and spaces in half-pitches of 22, 30, 40, and 50 nm. FTIR spectra of spin-coated thin films were measured using a Bruker Vertex 80v spectrometer (resolution = 10 cm^{-1}) and fast-Fourier transform (FFT) low-pass filtering was applied to 2000–4000 cm^{-1} range with a cutoff of 0.04 Hz to remove the interference fringes in the spectra. SEM images were obtained on a FEI Verios 460 SEM with a high voltage of 2.0 kV. Thickness measurements were conducted with a Bruker atomic force microscopy (AFM) from the edge of the thin film using the ScanAsyst mode.

8.3 Results and discussion

8.3.1 EUV absorptivity enhancement by fluorinated ligands

The estimation of the enhancement in EUV absorptivity provided by fluorinated ligands in $\text{Zr}_m\text{Mc}_n\text{TFMc}_n$ MOCs ($m + n = 12$) thin films is shown in Fig. 8.1. The linear absorption coefficient (α) is calculated as $\alpha = \mu \cdot \rho / \text{Mw}$,¹⁰ where

μ is the sum of atomic photoabsorption cross-section at 92 eV in cm^2/mol ,¹⁹ ρ is the material density in g/cm^3 and M_w is the molecular weight in g/mol . It is assumed that the molecular packing of this series of MOCs remains the same as the methacrylate analog in crystalline structure.²⁰ The transmittance of the material towards EUV irradiation is calculated as $T = e^{-\alpha d}$ according to the Beer–Lambert law, where d is the film thickness (40 nm).

The linear absorbance coefficient of ZrMc is estimated as $4.2 \mu\text{m}^{-1}$ (measured $5 \mu\text{m}^{-1}$),¹⁰ and can be raised to $8.9 \mu\text{m}^{-1}$ with the organic ligand shell fully replaced by TFMc ligands, according to the calculated value above. As a lower bound, if the molecular volume of the calculated structure is taken into consideration (see the simulation results in Table S8.1 in Supporting Information), the estimation of α (ZrTFMc) is modified to $8.1 \mu\text{m}^{-1}$ (black dot in Fig. 8.1), which is still 94% higher than the linear absorbance of the non-fluorinated ZrMc. To confirm such enhancement in absorptivity, EUV transmittance measurement will be carried out in future experiments.

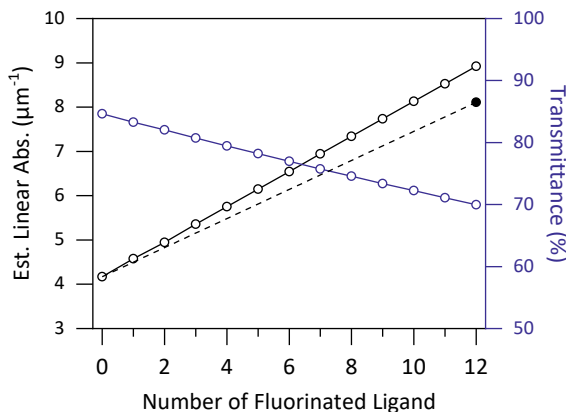


Figure 8.1: Estimated linear absorption coefficient and transmittance (film thickness = 40 nm) of $\text{Zr}_6\text{Mc}_m\text{TFMc}_n$ ($m + n = 12$) as a function of the number of trifluoromethacrylate ligands in the MOCs.

8.3.2 Solubility test and effect of developers

ZrTFMc is expected to be applicable as a negative tone EUV photoresist based on the mechanisms discussed for its analogues in Chapters 2 and 7. Therefore, a proper developer is supposed to dissolve the unexposed area of ZrTFMc thin film while leaving the exposed patterns intact. To find a proper solvent as the developer, 16 solvents were tested, as listed in Table 8.1 with the corresponding Hansen solubility parameters,²³ vapor pressure, and viscosity.

Hansen solubility parameters were proposed by Charles M. Hansen in 1967 to predict the solubility of materials in a solvent from three parameters that consider

Table 8.1: Physical properties of solvents tested for ZrTFMc

Solvent	Hansen Solubility Parameters (MPa ^{0.5})				Vapor pressure (hPa) ^b	Viscosity @20°C (cP) ^b
	Dispersion δ_d	Polar δ_p	H-Bonds δ_H	Total ^a δ		
Soluble						
Ethanol	15.8	8.8	19.4	26.5	59	1.08
Acetonitrile	15.3	18.0	6.1	24.4	97	0.34
Isopropanol	15.8	6.1	16.4	23.6	44	2.07
Methyl isobutyl carbinol(MIBC)	15.4	3.3	12.3	20.0	5	4.1–5.2
Acetone	15.5	10.4	7.0	19.9	240	0.30
Propylene glycol monomethyl ether acetate (PGMEA)	15.6	5.6	9.8	19.3	5	1.1 ^c
Methyl ethyl ketone (MEK)	16.0	9.0	5.1	19.1	104	0.43
Chloroform	17.8	3.1	5.7	18.9	210	0.54
Ethyl acetate	15.8	5.3	7.2	18.2	97	0.43
2-Heptanone	16.2	5.7	4.1	17.7	4	0.81
Methyl isobutyl ketone (MIBK)	15.3	6.1	4.1	17.0	21	0.58
Dichloromethane (DCM)	17.0	7.3	7.1	19.8	470	0.42
Insoluble						
Benzene	18.4	0	2.0	18.5	101	0.60
Toluene	18.0	1.4	2.0	18.2	29	0.55
Heptane	15.3	0	0	15.3	48	0.39
Pentane	14.5	0	0	14.5	573	0.23

^a $\delta^2 = \delta_d^2 + \delta_p^2 + \delta_H^2$.

^b From <http://murov.info/orgsolvents.htm>, <https://www.sigmaaldrich.com>, and <https://www.dow.com>.

^c At 25°C.

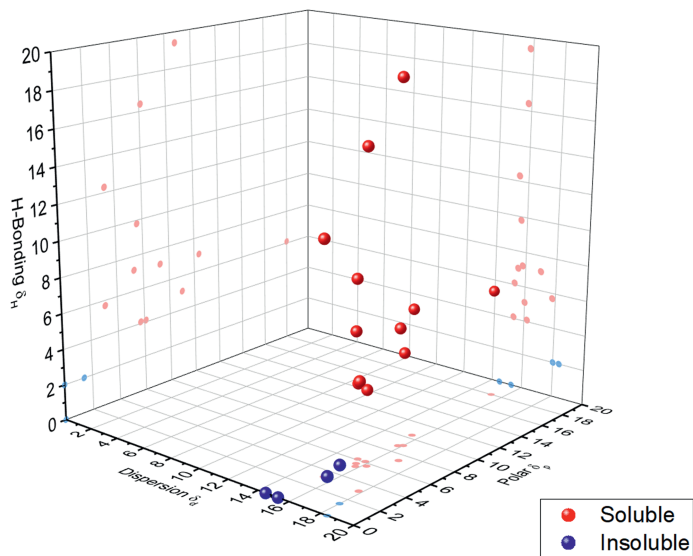


Figure 8.2: Three-dimensional diagram of Hansen solubility parameters of solvents for ZrTFMc.

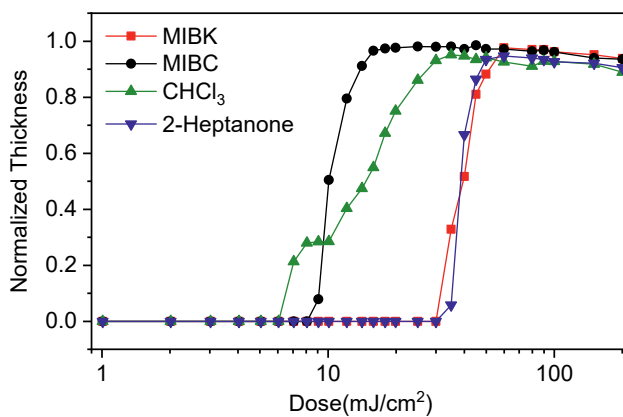


Figure 8.3: Contrast curves of ZrTFMc with four developers for 30 seconds.

molecular interactions of dispersion force (δ_d), dipole–dipole interactions (δ_p), and hydrogen bonds and other forces (δ_H).²⁴ Those parameters can be used to define a range in a three-dimensional space (sphere) within which molecular interactions favor miscibility and solubility. They have been originally developed for and widely used in polymers but also have been applied to inorganic materials and nanoparticle EUV photoresists.^{25–27} An in-depth solubility study is not the goal of this work. Yet the space defined by the parameters after studying the solubility properties of ZrTFMc in the solvents listed above (Fig. 8.2) suggests good solubility of this material in a wide range of solvents, so that more solvents within the sphere could be further tested to optimize the development process of the photoresist.

Four of the solvents, methyl isobutyl carbinol (MIBC), methyl isobutyl ketone (MIBK), chloroform, and 2-heptanone, were used in the EUV sensitivity test as developers. The contrast curves of ZrTFMc in those developers are shown in Fig. 8.3. MIBK and 2-heptanone have similar Hansen solubility parameters and the contrast curves of ZrTFMc with them as developers are comparable with rather low sensitivity and contrast. With MIBC as the developer, ZrTFMc exhibits high sensitivity with dose-to-gel (D_0) of 6 mJ/cm² and maximum solubility switch was achieved at a dose (D_{100}) around 12 mJ/cm², which led to a high contrast factor of 3.3 ($\gamma = 1/\log_{10}(D_{100}/D_0)$).²⁸ With chloroform, the sensitivity is similar to the previous case but the contrast factor is not as high as in MIBC. Therefore, MIBC was used as the developer for the patterning test and further optimization in the next section.

8.3.3 Effect of post-exposure bake

For chemically amplified photoresists, PEB is a crucial step to promote the diffusion of the photoacids generated during exposure along the polymeric matrix. In this fashion, more acid-catalysed deprotection reactions of the polymer side groups can occur and the hydrophobic character of the polymer decreases, ultimately favoring the solubility of the exposed areas in aqueous developers.^{29–32} In non-chemically amplified inorganic photoresists, proper PEB treatment can improve EUV lithographic performance significantly, especially on sensitivity.^{33–35} Yet, the mechanism is not yet well clarified and might be different for different inorganic/hybrid resist, as it not necessarily originating from the diffusion of reactive species. It is possible that photoproducts from EUV irradiation have lower bond dissociation energies or can further react with neighboring molecules and/or oxygen and/or moisture during the baking process, which is usually carried out in air.^{34,36} Besides, the complexity of the baking effect can lead to other unprecedented effects, as in the case of n-butyl Sn-oxo clusters (Sn-oxo cages), for which high-temperature PEB at 150 °C changed the solubility of the pristine material and switched this typically negative-tone photoresist to positive tone photoresist in the same developer.³⁷

In the analogous non-fluorinated material, ZrMc, heating at a temperature lower than 150 °C seems to remove only extra carboxylate ligands/carboxylic acids which are weakly bonded (See Fig. S2.5 in Supporting Information of Chap-

ter 2). In turn, the inorganic core unit $[\text{Zr}_6\text{O}_4(\text{OH})_4]$ can retain its integrity below $400\text{ }^\circ\text{C}$.³⁸ Based on these previous studies, we considered that temperatures below $150\text{ }^\circ\text{C}$ would not affect the unexposed materials and were safe for PEB tests. Yet a thermal stability study of ZrTFMc, such as thermogravimetric analysis (TGA), is required to accurately define a suitable PEB processing window.

Fig. 8.4a shows contrast curves of ZrTFMc without and with PEB at three temperatures (120 , 135 , and $150\text{ }^\circ\text{C}$) applied for one minute. The fact that the curve shifts towards lower doses with higher PEB temperature indicates that the baking treatment after EUV exposure improves the sensitivity in terms of D_0 and D_{100} . Besides, a shrinkage in the thickness of the film with baking temperature is observed. Both the changes with PEB reveal that further chemical reactions are induced in the exposed areas during heating.

Fig. 8.4b–d illustrate the top-down SEM images of line/space patterns of 22 , 30 , and 40 nm half-pitches under different PEB conditions. PEB at $120\text{ }^\circ\text{C}$ improves sensitivity while showing no significant change in the roughness of the patterns in comparison to the ones obtained without PEB. However, with higher baking temperature, although the sensitivity is further improved, increased roughness and bridging defects are observed in the patterns as shown in Fig. 8.4d. The improvement in sensitivity with PEB is also demonstrated in Fig 8.4e and f. The dose-to-size for HP 40 nm decreases from 71 mJ/cm^2 to 38 and 26 mJ/cm^2 with PEB temperature of $120\text{ }^\circ\text{C}$ and $135\text{ }^\circ\text{C}$, respectively. For L/S patterns of HP 30 nm , the dose-to size is 76 mJ/cm^2 without PEB and reduces to 40 mJ/cm^2 and 25 mJ/cm^2 when PEB at 120 and $135\text{ }^\circ\text{C}$ is applied.

8.3.4 EUV-induced chemical changes in ZrTFMc

To identify the chemical changes that the resist undergoes after EUV irradiation, the FTIR spectra of ZrTFMc films exposed with doses of 20 , 50 , and 200 mJ/cm^2 are compared to a reference spectrum of an unexposed thin film in Fig. 8.5a. In the O–H and C–H stretching regions, the absorption band attributed to the μ_3 -OH stretching in the metal-oxo core $[\text{Zr}_6\text{O}_4(\text{OH})_4]$ is observed at 3645 cm^{-1} , the broad band in $3000\text{--}3600\text{ cm}^{-1}$ is assigned to O–H from adsorbed moisture, either at the surface or at the bulk of the film, while bands of $2800\text{--}3000\text{ cm}^{-1}$ are due to aliphatic C–H stretches in acetate ligands that still remain in the structure from the precursor ($\sim 11\%$ in the bulk estimated from the ^1H NMR spectrum in Fig. S8.1). The absorption band arising from C=C stretching is observed at 1660 cm^{-1} . The band centered at 1590 is assigned to asymmetric COO stretching and bands of $1350\text{--}1500\text{ cm}^{-1}$ are assigned to symmetric COO stretching and CH_3 bending. The C–C=C rocking in the TFMc ligands gives rise to the band at 1322 cm^{-1} . Bands in the $1093\text{--}1224\text{ cm}^{-1}$ region arise from C–F stretches in the $-\text{CF}_3$ groups. The band at 994 cm^{-1} is due to the out-of-plane bending of $=\text{CH}_2$ and the bands in $600\text{--}726\text{ cm}^{-1}$ are assigned to a combination of Zr–O stretching and COO bending.

The FTIR spectral changes are demonstrated as relative absorbance (%) referenced to the unexposed sample in Fig. 8.5b. The absorption bands arising from

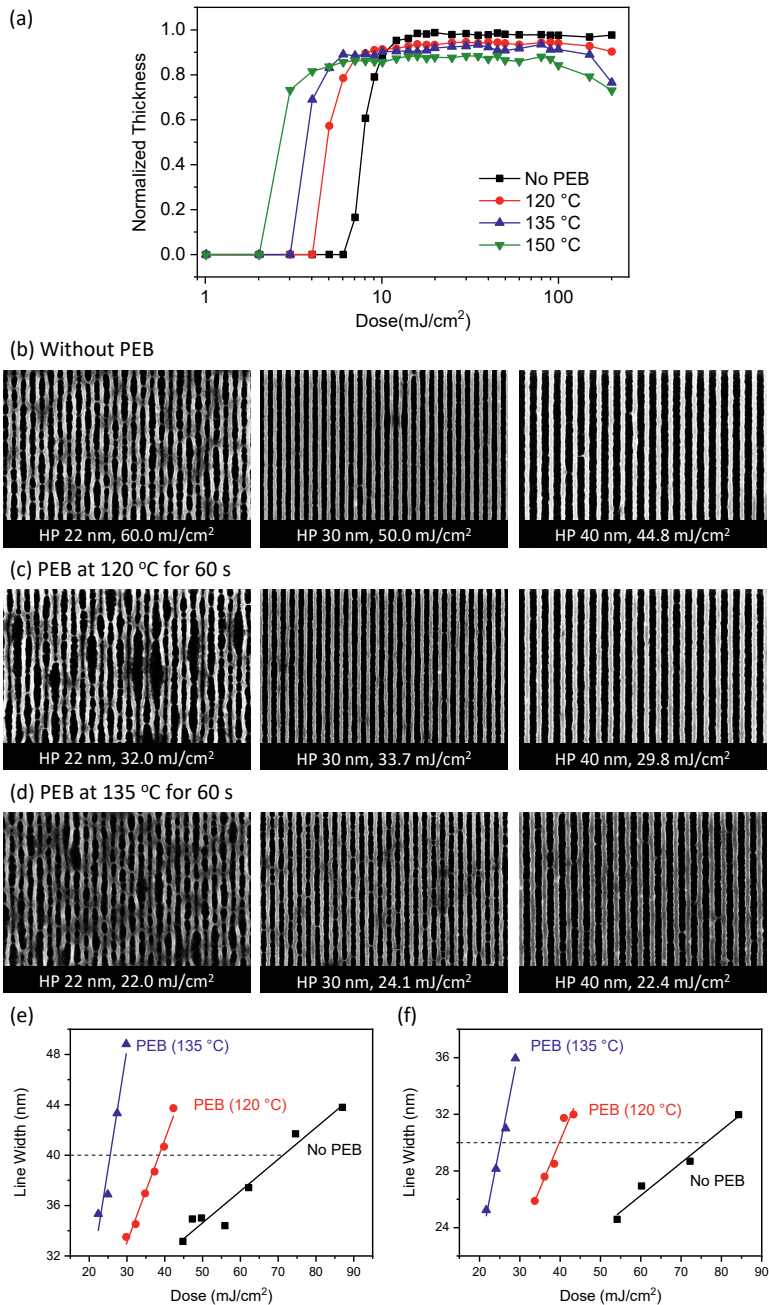


Figure 8.4: (a) Contrast curves of ZrTFMc developed in MIBC with/without post exposure bake for 60 s. (b–d) SEM images at different doses with/without PEB. (e) Dose-to-size of HP = 40 nm and (f) HP = 30 nm.

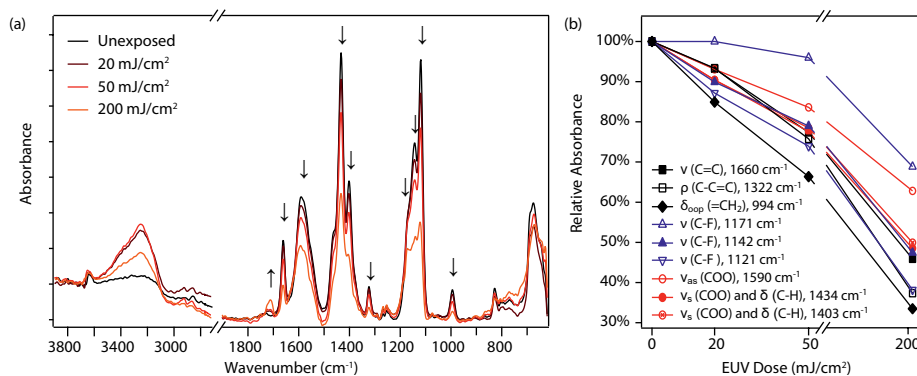


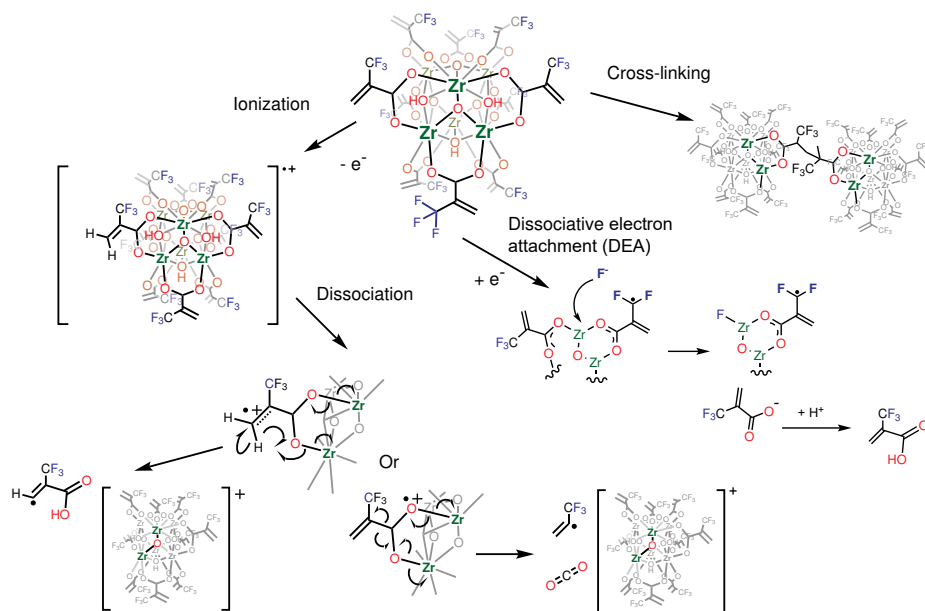
Figure 8.5: (a) FTIR spectra of ZrTFMc films after EUV exposure of 20, 50, 200 mJ/cm² referenced to the unexposed thin film. (b) Relative absorbance intensities of selective bands at different EUV exposure dose.

COO, which centered at 1590 cm^{-1} (ν_{as}), 1434 , 1403 cm^{-1} (ν_s), and 673 cm^{-1} (δ) decrease with EUV exposure. This implies the dissociation of the carboxylate ligands after EUV irradiation. The absorption intensities of the bands associated with $-\text{C}=\text{CH}_2$ at 1660 cm^{-1} (ν), 1322 cm^{-1} ($\delta_{\text{C}-\text{C}=\text{C}}$) and 994 cm^{-1} (δ_{oop}) also decrease with EUV doses, but they drop faster than those due to COO vibrational modes. This indicates that, in addition to ligand loss, some of the C=C bonds participate in cross-linking reactions, as in the analogous non-fluorinated material ZrMc.⁶ The lower intensity of bands in C-F stretching regions after EUV exposure points at the cleavage of C-F bonds or of the $-\text{CF}_3$ group. This change can lead to reduced hydrophobicity of the exposed material and thus the broad band of O-H stretching in $3000\text{--}3600\text{ cm}^{-1}$ increases in exposed samples compared to the pristine material. Besides, a new band at 1710 cm^{-1} assigned to $\nu_{\text{C}=\text{O}}$ is detected after EUV irradiation. Based on the spectroscopic results in this chapter and in the closely related material presented in Chapter 7, the proposed reaction mechanisms for ZrTFMc are summarized in Scheme 8.2.

The UV absorption spectra (Fig. 8.6) agree with the FTIR spectral changes and the mechanisms proposed above. The bleach at $\sim 191\text{ nm}$, attributed to $\pi \rightarrow \pi^*$ electronic transitions of C=C is indicative of decreasing double bonds upon EUV exposure, either due to the cross-linking of alkene terminal groups or the dissociation and loss of the TFMc ligands.

8.3.5 Mechanistic insights in PEB

In order to identify how the PEB can further induce chemical reactions in the exposed film and how those changes finally lead to a lower solubility in the developer of choice (MIBC), in Fig. 8.7 are compared to the FTIR spectra of ZrTFMc thin films after three sequential processes—exposure, PEB, and development—at different doses. Without exposure, the film was completely removed by the de-



Scheme 8.2: Proposed reactions induced by EUV that lead to the loss of COO, C-F and C=C and formation of C=O.

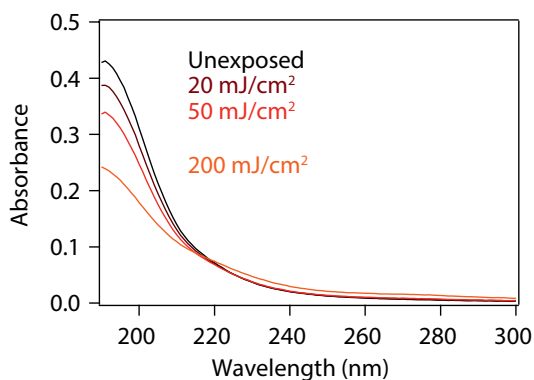


Figure 8.6: UV absorption spectra of ZrTFMc.

veloper, showing only O–H stretch from adsorbed moisture and noise from the baseline (Si–O–Si stretching at 1100 cm^{-1})³⁹ in the FTIR spectrum. This indicates that $120\text{ }^{\circ}\text{C}$ baking has no effect on the solubility of the material. Only a slight decrease of ligands-related vibrational modes was detected, which might be due to the removal of some extra weakly bonded ligands by the baking or simply to slight variations in the film thickness from sample to sample (38–40 nm). At 20 and 50 mJ/cm^2 , there is no significant change in the sample with PEB. At these doses, the solubility of ZrTFMc has been switched after exposure and the exposed area remains after development. Remarkably, the insoluble areas give spectra that are identical to the non-developed ones. At 200 mJ/cm^2 , the difference between three spectra of each processing step is also negligible. Therefore the sensitivity improvement from PEB is due to chemical changes that cannot be detected with this IR measurement. Possibly, changes in the absorption band corresponding to Zr–F stretching could be observed in the region below 475 cm^{-1} ,^{40–42} but this is outside the available spectral range. It could be that baking induces the condensation among neighboring oxo core units that have lost ligands during exposure. The created MOC network can be responsible for the increase in roughness and bridging defects with higher PEB temperatures.

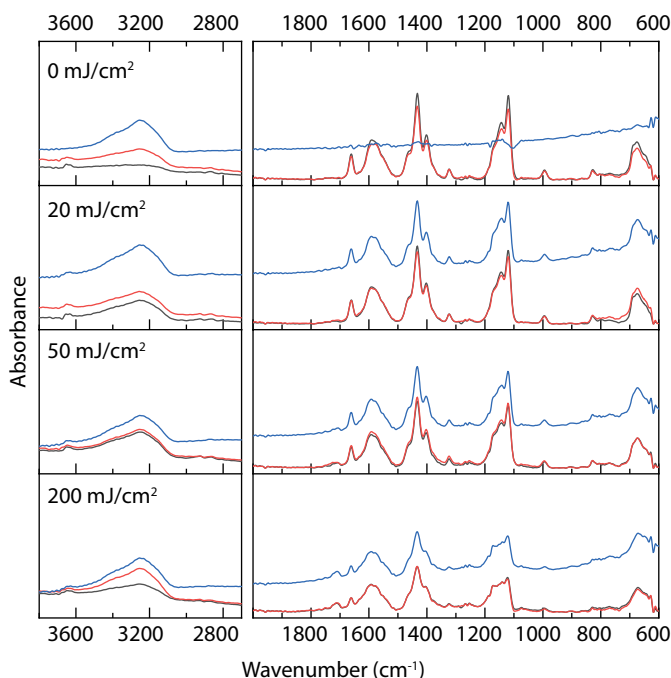


Figure 8.7: FTIR spectra of ZrTFMc thin films as exposed (in grey), after PEB at $120\text{ }^{\circ}\text{C}$ for 1 minute (in red) and after development in MIBC for 30 seconds (in blue).

8.4 Conclusion

We synthesized a new Zr-based metal oxo cluster with fluorine-rich and cross-linkable organic ligands. The absorptivity towards EUV of this ZrTFMc cluster is expected to be much higher compared to its non-fluorinated analog. The good solubility of ZrTFMc in a wide range of solvents allows for future optimization of lithographic processing with different developers. In addition, PEB helps to further improve the sensitivity of this EUV photoresist.

Zirconium is one of the most transparent metal elements towards EUV. We have demonstrated in this work that the EUV absorptivity of metal-based organic-inorganic hybrid photoresist can be significantly enhanced with proper modification of the organic shell in the molecular design. In addition, a different functional group can provide better processability and lead to improvements in the lithographic performance. We are confident that our work provides an alternative strategy for rational designs of new EUV photoresist materials in addition to incorporating high-absorbing metal elements.

Bibliography

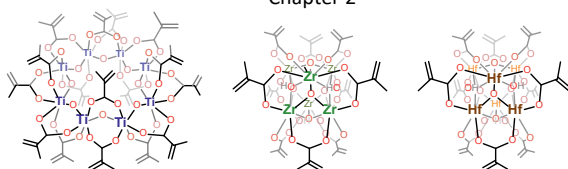
- [1] J. Passarelli, M. Murphy, R. Del Re, M. Sortland, L. Dousharm, M. Vockenhuber, Y. Ekinici, M. Neisser, D. A. Freedman and R. L. Brainard, *Proc. SPIE*, 2015, **9425**, 94250T.
- [2] J. Jiang, B. Zhang, M. Yu, L. Li, M. Neisser, J. S. Chun, E. P. Giannelis and C. K. Ober, *J. Photopolym. Sci. Technol.*, 2015, **28**, 515–518.
- [3] L. Li, X. Liu, S. Pal, S. Wang, C. K. Ober and E. P. Giannelis, *Chem. Soc. Rev.*, 2017, **46**, 4855–4866.
- [4] C. Luo, C. Xu, L. Lv, H. Li, X. Huang and W. Liu, *RSC Adv.*, 2020, **10**, 8385–8395.
- [5] S. Castellanos, L. Wu, M. Baljozovic, G. Portale, D. Kazazis, M. Vockenhuber, Y. Ekinici and T. Jung, *Proc. SPIE*, 2018, **10583**, 105830A.
- [6] L. Wu, M. Baljozovic, G. Portale, D. Kazazis, M. Vockenhuber, T. Jung, Y. Ekinici and S. Castellanos, *J. Micro/Nanolithogr., MEMS, MOEMS*, 2019, **18**, 013504.
- [7] N. Thakur, L.-T. Tseng, M. Vockenhuber, Y. Ekinici and S. Castellanos, *J. Micro/Nanolith. MEMS MOEMS*, 2019, **18**, 043504.
- [8] L. Wu, M. Vockenhuber, Y. Ekinici and S. Castellanos, *Proc. SPIE*, 2019, **10957**, 109570B.
- [9] R. Fallica, J. K. Stowers, A. Grenville, A. Frommhold, A. P. G. Robinson and Y. Ekinici, *J. Micro/Nanolithogr., MEMS, MOEMS*, 2016, **15**, 033506.
- [10] R. Fallica, J. Haitjema, L. Wu, S. Castellanos, , A. M. Brouwer and Y. Ekinici, *J. Micro/Nanolithogr., MEMS, MOEMS*, 2018, **17**, 023505.
- [11] D. P. Sanders, L. K. Sundberg, R. Sooriyakumaran, P. J. Brock, R. A. DiPi-

- etro, H. D. Truong, D. C. Miller, M. C. Lawson and R. D. Allen, *Proc. SPIE*, 2007, **6519**, 651904.
- [12] A. Otake, M. Miura, K. Tsuchiya and K. Ogino, *J. Photopolym. Sci. Technol.*, 2008, **21**, 679–684.
- [13] R. R. Kunz, T. M. Bloomstein, D. E. Hardy, R. B. Goodman, D. K. Downs and J. E. Curtin, *JJ. Vac. Sci. Technol. B*, 1999, **17**, 3267–3272.
- [14] H. V. Tran, R. J. Hung, T. Chiba, S. Yamada, T. Mrozek, Y.-T. Hsieh, C. R. Chambers, B. P. Osborn, B. C. Trinqué, M. J. Pinnow, D. P. Sanders, E. F. Connor, R. H. Grubbs, W. Conley, S. A. MacDonald and C. G. Willson, *J. Photopolym. Sci. Technol.*, 2001, **14**, 669–674.
- [15] H. Ito, H. D. Truong, M. Okazaki and R. A. DiPietro, *J. Photopolym. Sci. Technol.*, 2003, **16**, 523–536.
- [16] M. Rothschild, T. M. Bloomstein, T. H. Fedynyshyn, V. Liberman, W. Mowers, R. Sinta, M. Switkes, A. Grenville and K. Orvek, *J. Fluorine Chem.*, 2003, **122**, 3–10.
- [17] S. Ikeda, K. Okamoto, H. Yamamoto, A. Saeki, S. Tagawa and T. Kozawa, *Jpn. J. Appl. Phys.*, 2010, **49**, 096504.
- [18] N. Nomura, K. Okamoto, H. Yamamoto, T. Kozawa, R. Fujiyoshi and K. Umegaki, *Jpn. J. Appl. Phys.*, 2015, **54**, 06FE03.
- [19] B. L. Henke, E. M. Gullikson and J. C. Davis, *At. Data Nucl. Data Tables*, 1993, **54**, 181–342.
- [20] G. Kickelbick and U. Schubert, *Chem. Ber.*, 1997, **130**, 473–477.
- [21] K. Ito and H. J. Bernstein, *Can. J. Chem.*, 1956, **34**, 170–178.
- [22] J. Kreutzer, P. Blaha and U. Schubert, *Comput. Theor. Chem.*, 2016, **1084**, 162–168.
- [23] C. M. Hansen, *Hansen solubility parameters: a user's handbook*, CRC press, 2007.
- [24] C. M. Hansen, *The three dimensional solubility parameter and solvent diffusion coefficient: Their importance in surface coating formulation*, PhD thesis, Danish Technical Press, Copenhagen, 1967.
- [25] C. M. Hansen, *Prog. Org. Coat.*, 2004, **51**, 77–84.
- [26] K. V. S. N. Raju and M. Yaseen, *Langmuir*, 1992, **8**, 43–47.
- [27] L. Li, S. Chakrabarty, J. Jiang, B. Zhang, C. K. Ober and E. P. Giannelis, *Nanoscale*, 2016, **8**, 1338–1343.
- [28] S. A. Campbell, *The Science and Engineering of Microelectronic Fabrication*, Oxford University Press, 1996.
- [29] T. Itani, H. Yoshino, S. Hashimoto, M. Yamana, N. Samoto and K. Kasama, *Microelectron. Eng.*, 1997, **35**, 149–152.
- [30] H. Ito, *Microolithography- Molecular Imprinting*, Springer, 2005, vol. 172, pp. 37–245.
- [31] A. De Silva, N. Felix, J. Sha, J.-K. Lee and C. K. Ober, *Proc. SPIE*, 2008,

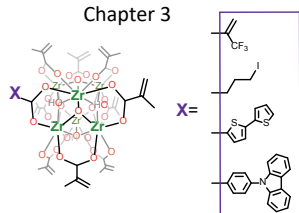
- 6923**, 69231L.
- [32] Y. Vesters, D. De Simone and S. De Gendt, *Proc. SPIE*, 2017, **10143**, 1014324.
 - [33] Y. Ekinici, M. Vockenhuber, B. Terhalle, M. Hojeij, L. Wang and T. R. Younkin, *Proc. SPIE*, 2012, **8322**, 83220W.
 - [34] J. Haitjema, Y. Zhang, M. Vockenhuber, D. Kazazis, Y. Ekinici and A. M. Brouwer, *J. Micro/Nanolithogr., MEMS, MOEMS*, 2017, **16**, 033510.
 - [35] X. Wang, L.-T. Tseng, I. Mochi, M. Vockenhuber, L. van Lent-Protasova, R. Custers, G. Rispens, R. Hoefnagels and Y. Ekinici, *Proc. SPIE*, 2019, **11147**, 1114711.
 - [36] Y. Zhang, *Organotin Photoresists for extreme ultraviolet lithography*, PhD thesis, University of Amsterdam, 2019, pp. 51–62.
 - [37] Y. Zhang, J. Haitjema, M. Baljovic, M. Vockenhuber, D. Kazazis, T. A. Jung, Y. Ekinici and A. M. Brouwer, *J. Photopolym. Sci. Technol.*, 2018, **31**, 249–255.
 - [38] G. C. Shearer, S. Chavan, J. Ethiraj, J. G. Vitillo, S. Svelle, U. Olsbye, C. Lamberti, S. Bordiga and K. P. Lillerud, *Chem. Mater.*, 2014, **26**, 4068–4071.
 - [39] A. L. Smith, *Spectrochim. Acta*, 1960, **16**, 87–105.
 - [40] J. He, X. Cai, K. Chen, Y. Li, K. Zhang, Z. Jin, F. Meng, N. Liu, X. Wang, L. Kong, X. Huang and J. Liu, *J. Colloid Interface Sci.*, 2016, **484**, 162–172.
 - [41] G. V. Jere and M. T. Santhamma, *Inorg. Chim. Acta*, 1977, **24**, 57–61.
 - [42] R. D. Peacock and D. W. A. Sharp, *J. Chem. Soc.*, 1959, 2762–2767.

Summary

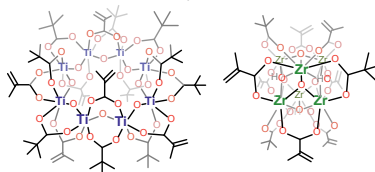
Chapter 2



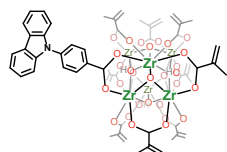
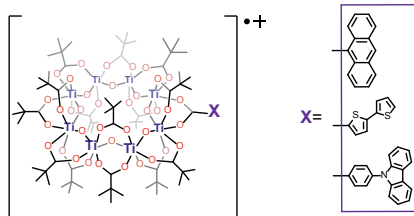
Chapter 3



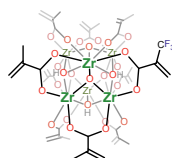
Chapter 4



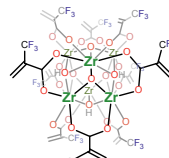
Chapter 5



Chapter 6



Chapter 7



Chapter 8

The down-scaling of transistors and improvement in computing performance of chips is continued by utilizing extreme ultraviolet (EUV) light in photolithography. Photoresists are crucial materials used in photolithography for printing patterns on chips. While resists comprising metallic elements and organic moieties are arising as the most promising materials for EUV lithography, the lack of understanding of the patterning mechanisms in this type of material hinders rational designs of the resists with optimal lithographic performance.

Chapter 1 provides a brief introduction to EUV lithography and EUV photoresists. Different material platforms are summarized and examples of patterning mechanisms in various photoresists are described. Metal-based molecular hybrid materials attract our interest and metal oxo clusters (MOCs) are studied as model EUV resist materials in this thesis.

These studies begin with a discussion about the impact of metal components on the resist behavior in **Chapter 2**. Metal oxo clusters comprising methacrylate ligands and different metal-oxo cores of Ti, Zr, and Hf, respectively, are tested as EUV photoresists. The low solubility and poor quality of spin-coated thin films of the Ti-based MOCs hinder their further investigation, while EUV printabilities of methacrylate MOCs based on Zr and Hf are demonstrated. The Hf-based MOC resist displays higher sensitivity than the Zr-based analogue, in agreement with the trend in their EUV absorptivity. Spectroscopic analysis on the EUV-exposed materials reveals that the loss of a small portion of carboxylate groups accompanied by cross linking of the terminal alkene groups in the methacrylate ligands are responsible for the solubility switch in these materials after EUV exposure.

The impact of organic components on absorptivity and reactivity towards EUV photons and the ultimate performance of MOC resists are discussed in Chapters 3–8. **Chapter 3** presents a method to investigate the effect of specific functionalities on the sensitivity of metal oxo clusters via doping the methacrylate shell of zirconium oxo clusters with fluorinated, iodinated and extended aromatic ligands. The introduction of each of these functionalities in small ratios of 1:11 and 2:10 to the methacrylate ligand preserves the solubility and processability of the precursor material. The incorporation of fluorine or iodine atoms shows improvement in the sensitivity of the resist while extended aromatic units are detrimental to the sensitivity. Further investigations to reveal the mechanistic explanations of these effects are presented in Chapters 5–7.

Chapter 4 describes another method to prepare MOCs featuring two types of ligands. MOCs with mixed-ligand shells are synthesized via ligand exchange reactions followed by a purification step with amine-functionalized resins. Ti- and Zr-based MOCs are prepared with pivalate and methacrylate ligands in the ratios of 10:6 and 4:8, respectively. The mixed ligands on the cluster surface improve the solubility and enable the thin film deposition of Ti-based MOCs for lithographic tests. In Zr-based MOCs, incorporation of pivalate ligands decreases the number of terminal double bonds in the organic shell, showing lower EUV sensitivity as a photoresist than the methacrylate Zr-MOC. These two cases demonstrate the impact of organic ligands on the solubility, processability, and reactivity towards EUV light in MOC-type resists.

Chapters 5 and 6 focus on extended aromatic carboxylate ligands. EUV light is ionizing radiation and the primary electrons generated upon EUV irradiation induce further ionization in the resists. Therefore, photoionization studies can help us to gain understanding of *in situ* reactions of molecules upon EUV exposure. In **Chapter 5** we investigate the photoionization process of a series of pivalate titanium oxo clusters doped with extended aromatic structures in combination of computational studies. Those doped Ti-MOCs are ionized by atmospheric pressure photoionization (APPI) and brought into the gas phase. The isolated parent ions in an ion trap are exposed to synchrotron radiation in the 7–12 eV range where ionization thresholds of these molecules are expected while products of photodissociation and photoionization are monitored by mass spectroscopy at each energy step. This study shows that those parent ions featuring aromatic ligands have lower photoionization thresholds than the precursors without doping. Besides, because of hole stabilizing properties from the conjugated structures, they are ionized in a non-dissociative way, whereas the pivalate parent ions undergo ligand dissociation upon photoionization.

In **Chapter 6** we take a closer look at aromatic ligands in MOCs for EUV lithography. We functionalize methacrylate zirconium oxo clusters with carbazole benzoate which was studied in the previous chapter. The aim is to modify the electronic structure to favor ionization and to provide the material with fluorescence. As an EUV photoresist, the carbazole doped Zr-MOC is much less sensitive than the methacrylate precursors, so that higher exposure doses are required for the solubility switch. Fluorescence microscopy and spectroscopy are used to characterize the structural changes of the MOC after EUV exposure for further mechanistic information, in combination with infrared and UV absorption spectroscopy. The spectral changes of the exposed material indicate that the loss of methacrylate ligands and the crosslinking of C=C bonds occur upon EUV exposure while carbazole ligands are rather inert. Yet fluorescence quenching is observed in the exposed films, possibly because electron transfer processes compete with emissive decays in the irradiated material. The hole trapping mechanism discussed in the previous chapter is applicable to explain the lower EUV reactivity here.

Chapters 7 and 8 are devoted to fluorinated crosslinkable ligands. The enhancement in resist sensitivity by the introduction of a small fraction of fluorinated ligands into MOCs has been described in Chapter 3. **Chapter 7** provides further mechanistic insights into this effect via scanning transmission X-ray microscopy and X-ray photoelectron spectroscopy. The results evidence radical polymerization as a mechanism for the solubility switch. In addition, dissociation of C–F bonds and formation of Zr–F bonds in the EUV exposed samples are observed in the spectra. The enhancement of fluorinated crosslinkable ligands in material absorptivity and reactivity upon EUV demonstrated in this work motivates the study in the next chapter.

This thesis is completed by **Chapter 8** on a fluorine-rich zirconium oxo cluster. Zirconium oxo clusters featuring fluorinated crosslinkable ligands are synthesized from acetate MOC precursors in this chapter. This new MOC shows good solubility and processability, and renders higher resolution in lines-and-spaces patterning

than the MOCs studied in previous chapters. Chemical changes in the material after EUV exposure and baking are investigated via infrared and UV-visible absorption spectroscopy.

We thus have demonstrated how the modification of the organic-shell composition in hybrid materials can be used to significantly improve the resist performance, and have discussed which reaction mechanisms can be induced by different functionalities. The generated knowledge can be applied in oxo clusters featuring other metals with higher EUV absorption cross-section than Zr, such as Hf, Zn, or Sn, so that the lithographic performance of metal oxo clusters could be further improved.

Samenvatting

Door het verkleinen van transistors worden computerchips steeds kleiner en efficiënter. Om dit te bereiken wordt fotolithografie gebruikt met licht van steeds kleinere golflengtes, met als nieuwste ontwikkeling extreem ultraviolet (EUV) licht met een golflengte van 13,5 nm. Fotolakken, meestal aangeduid met de Engelse term “photoresist”, of kortweg “resist”, zijn cruciale materialen die in de fotolithografie worden gebruikt voor het overbrengen van patronen op chips. Een dunne laag photoresist op een ondergrond wordt belicht met een patroon, waarbij de oplosbaarheid in de belichte delen verandert. Het belichte (of onbelichte) deel van de laag wordt vervolgens weggewassen waarna een bewerking op het vrijgekomen oppervlak kan plaatsvinden. Resists die metallische elementen en organische groepen bevatten lijken de meest veelbelovende materialen voor EUV-lithografie te worden, maar het gebrek aan kennis van de chemische werkingsmechanismen in dit type materialen belemmert het onderbouwd ontwerpen van resists met optimale lithografische resultaten.

Hoofdstuk 1 is een korte inleiding tot EUV-lithografie en EUV-photoresists. Verschillende typen materialen worden besproken en voorbeelden van patroonvormingsmechanismen in verschillende photoresists worden beschreven. Moleculaire hybride materialen, gebaseerd op metalen, staan sterk in de belangstelling en metaal oxo-clusters (MOC's) worden in dit proefschrift bestudeerd als ‘model’ EUV-resists. Dit begint met een discussie van de invloed van de metaal-componenten op het resistgedrag in **Hoofdstuk 2**. Metaal oxo-clusters die methacrylaatliganden en verschillende metaal oxo-kernen van respectievelijk Ti, Zr en Hf bevatten, worden getest als EUV-photoresists. Op Ti gebaseerde MOC's hebben een slechte oplosbaarheid en de gespinoate dunne films zijn van matige kwaliteit, maar methacrylaat MOC's op basis van Zr en Hf blijken heel geschikt voor het vormen van patronen onder invloed van EUV licht. De op Hf gebaseerde MOC-resist vertoont een hogere gevoeligheid dan de op Zr gebaseerde, in overeenstemming met de trend in hun EUV-absorptievermogen. Spectroscopische analyse van de aan EUV blootgestelde materialen laat zien dat het verlies van een klein deel van de carboxylaatgroepen, in combinatie met onderlinge verbinding van de alkeengroepen in de methacrylaatliganden, verantwoordelijk is voor de verandering in

oplosbaarheid in deze materialen.

De invloed van de organische componenten op absorptie en reactiviteit ten opzichte van EUV-fotonen en de uiteindelijke prestaties van MOC-resists worden besproken in de hoofdstukken 3–8. **Hoofdstuk 3** laat een methode zien om het effect van specifieke functionaliteiten op de gevoeligheid van metaaloxoclusters te onderzoeken door de methacrylaatschil van zirkoniumoxoclusters voor een deel te vervangen door liganden die fluor, jodium, of grotere aromatische groepen bevatten. Door elk van deze functionele groepen in kleine verhoudingen van respectievelijk 1:11 en 2:10 ten opzichte van het methacrylaatligand te introduceren, worden de oplosbaarheid en verwerkbaarheid van het oorspronkelijke materiaal behouden. Het opnemen van fluor- of jodiumatomen leidt tot een verbetering in de gevoeligheid van de resist, terwijl uitgebreide aromatische eenheden de gevoeligheid juist nadelig beïnvloeden. Verder onderzoek naar de mechanistische verklaringen van deze effecten wordt gepresenteerd in de hoofdstukken 5–7.

Hoofdstuk 4 beschrijft een andere methode om MOC's te bereiden met twee soorten liganden. MOC's met gemengde ligandschillen worden gesynthetiseerd via liganduitwisselingsreacties gevolgd door een zuiveringsstap met aminegefunctionaliseerde harsen. Op Ti en Zr gebaseerde MOC's worden bereid met pivalaat- en methacrylaatliganden in verhoudingen van respectievelijk 10:6 en 4:8. De gemengde liganden op het clusteroppervlak verbeteren de oplosbaarheid en maken het mogelijk om met op Ti gebaseerde MOC's dunne films te vormen die geschikt zijn voor lithografische tests. In op Zr gebaseerde MOC's vermindert de opname van pivalaatliganden het aantal terminale dubbele bindingen in de organische schil, wat leidt tot een lagere EUV-gevoeligheid als fotoresist dan de methacrylaat Zr-MOC. Deze twee gevallen laten de invloed zien die organische liganden hebben op de oplosbaarheid, verwerkbaarheid en reactiviteit van resists van het MOC-type onder invloed van EUV-licht.

Hoofdstukken 5 en 6 richten zich op grotere aromatische carboxylaatliganden. EUV-licht is ioniserende straling en de primaire elektronen die worden gegenereerd bij EUV-bestraling induceren verdere ionisatie in de resists. Foto-ionisatiestudies kunnen ons daarom helpen om inzicht te krijgen in in situ reacties van moleculen bij blootstelling aan EUV-straling. In **Hoofdstuk 5** onderzoeken we het foto-ionisatieproces van een reeks pivalaat-titanium oxoclusters gedoteerd met uitgebreide aromatische structuren in combinatie met computationele studies. Die gedoteerde Ti-MOC's worden geïoniseerd door foto-ionisatie bij atmosferische druk (Atmospheric Pressure Photoionization, APPI) en in de gasfase gebracht. De geïsoleerde ionen in een ionenval worden blootgesteld aan synchrotronstraling in het gebied van 7–12 eV waar ionisatiedrempels van deze moleculen worden verwacht, terwijl producten van fotodissociatie en foto-ionisatie bij elke energiestap met massaspectrometrie worden gedetecteerd. Deze studie toont aan dat de ionen met aromatische liganden lagere foto-ionisatiedrempels hebben dan de uitgangsverbindingen zonder deze groepen. Bovendien zijn de geconjugeerde structuren na ionisatie stabiel, in tegenstelling tot de pivalaat-moederionen die liganden verliezen als gevolg van foto-ionisatie.

In **Hoofdstuk 6** gaan we dieper in op aromatische liganden in MOC's voor

EUV-lithografie. We functionaliseren methacrylaat-zirkoniumoxo-clusters met het carbazoalbenzooat dat in het vorige hoofdstuk al werd bestudeerd. Het doel is om de elektronische structuur te veranderen om ionisatie te bevorderen en om het materiaal van fluorescentie-eigenschappen te voorzien. Als EUV-photoresist is het met carbazoal gedoteerde Zr-MOC veel minder gevoelig dan de methacrylaatprecursors, zodat hogere blootstellingsdoses nodig zijn voor de oplosbaarheidsverandering. Fluorescentiemicroscopie en spectroscopie worden gebruikt om de structurele veranderingen van de MOC na EUV-blootstelling te karakteriseren om verdere mechanistische informatie te verkrijgen, in combinatie met infrarood- en UV-absorptiespectroscopie. De spectrale veranderingen van het belichte materiaal geven aan dat het verlies van methacrylaatliganden en de verknoping van C=C-bindingen optreden bij blootstelling aan EUV, terwijl de carbazoalliganden tamelijk inert zijn. Toch wordt fluorescentie-uitdoving waargenomen in de belichte films, mogelijk omdat elektronenoverdrachtsprocessen concurreren met emissieverval in het bestraalde materiaal. Hetzelfde mechanisme dat in het vorige hoofdstuk werd besproken, is ook van toepassing om de lagere EUV-activiteit hier te verklaren.

De hoofdstukken 7 en 8 zijn gewijd aan fluor bevattende verknopbare liganden. De verbetering van resistgevoeligheid door de introductie van een kleine fractie gefluoreerde liganden in MOC's is beschreven in hoofdstuk 3. **Hoofdstuk 7** geeft meer mechanistisch inzicht in dit effect via raster transmissie röntgenmicroscopie en röntgen foto-elektron spectroscopie. De resultaten tonen radicaalpolymerisatie aan als een mechanisme voor de oplosbaarheidsverandering. Bovendien laten de spectra zien dat C-F bindingen zijn gedissocieerd en dat Zr-F bindingen zijn gevormd in de aan EUV blootgestelde monsters. De verbetering gegeven door gefluoreerde verknopbare liganden in materiaalabsorptie en reactiviteit op EUV, aangetoond in dit werk, is een aanzet tot het onderzoek in het volgende hoofdstuk.

Dit proefschrift wordt afgerond met **Hoofdstuk 8**, waarin een fluorrijke zirkoniumoxocluster wordt behandeld. Zirkoniumoxoclusters met gefluoreerde verknopbare liganden zijn gesynthetiseerd uit acetaat-MOC-precursors. Deze nieuwe MOC vertoont een goede oplosbaarheid en verwerkbaarheid, en levert een hogere resolutie in lijn-en-ruimtepatronen op dan de MOC's die in eerdere hoofdstukken zijn beschreven. Chemische veranderingen in het materiaal na blootstelling aan EUV en uitbakken worden onderzocht via infrarood en UV-zichtbare absorptiespectroscopie.

In dit proefschrift hebben we laten zien hoe de modificatie van de organische schil-samenstelling in hybride materialen kan worden gebruikt om de resistprestaties aanzienlijk te verbeteren, en we hebben besproken welke reactiemechanismen kunnen worden geïnduceerd door verschillende chemische functionaliteiten. De gegenereerde kennis kan worden toegepast in oxo-clusters met andere metalen met een hogere EUV-absorptiedoorsnede dan Zr, zoals Hf, Zn of Sn, zodat de lithografische prestaties van metaal oxo-clusters verder kunnen worden verbeterd.

List of Publications

This thesis is based on the following publications:

Chapter 2: S. Castellanos, L. Wu, M. Baljozovic, G. Portale, D. Kazazis, M. Vockenhuber, Y. Ekinici, and T. Jung, “Ti, Zr, and Hf-based molecular hybrid materials as EUV photoresists”, *Proc. SPIE*, 2018, **10583**, 105830A;

L. Wu, M. Baljozovic, G. Portale, D. Kazazis, M. Vockenhuber, Y. Ekinici, T. Jung, and S. Castellanos, “Mechanistic insights in Zr-and Hf-based molecular hybrid EUV photoresists”, *J. Micro/Nanolithogr., MEMS, MOEMS*, 2019, **18**, 013504.

Chapter 3: L. Wu, M. Vockenhuber, Y. Ekinici, and S. Castellanos, “The role of the organic shell in hybrid molecular materials for EUV lithography”, *Proc. SPIE*, 2019, **10957**, 109570B.

Chapter 4: L. Wu, J. Liu, M. Vockenhuber, Y. Ekinici, and S. Castellanos, “Hybrid EUV resists with mixed organic shells: a simple preparation method”, *Eur. J. Inorg. Chem.*, 2019, **2019**, 4136-4141.

Chapter 5: L. Wu, M. Tiekink, A. Giuliani, L. Nahon, and S. Castellanos, “Tuning photoionization mechanisms of molecular hybrid materials for EUV lithography applications”, *J. Mater. Chem. C*, 2019, **7**, 33-37.

Chapter 6: L. Wu, M. F. Hilbers, O. Lugier, N. Thakur, M. Vockenhuber, Y. Ekinici, A. M. Brouwer, and S. Castellanos, “Introduction of a fluorescent ligand in an inorganic extreme ultraviolet resist”, manuscript in preparation.

Chapter 7: L. Wu, I. Bepalov, K. Witte, O. Lugier, J. Haitjema, M. Vockenhuber, Y. Ekinici, B. Watts, A. M. Brouwer, and S. Castellanos, “Unravelling the effect of fluorinated ligands in hybrid extreme ultraviolet photoresists by X-ray spectroscopy”, *J. Mater. Chem. C*, 2020, DOI: 10.1039/d0tc03216f.

Chapter 8: L. Wu, D. Kazazis, Y. Ekinici, and S. Castellanos, “Fluorine-rich zirconium oxo clusters with enhanced EUV absorptivity for nanopatterning”, manuscript in preparation.

Other Publications:

- C. Dieleman, W. Ding, L. Wu, N. Thakur, I. Bepalov, B. Daiber, Y. Ekinici, S. Castellanos, and B. Ehrler, “Universal direct patterning of colloidal quantum dots by (extreme) ultraviolet and electron beam lithography”, *Nanoscale*, 2020, **12**, 11306-11316.
- J. Haitjema, L. Wu, A. Giuliani, L. Nahon, S. Castellanos, and A. M. Brouwer, “Photo-induced fragmentation of a tin-oxo cage compound”, *J. Photopolym. Sci. Technol.*, 2018, **31**, 243-247.
- R. Fallica, J. Haitjema, L. Wu, S. Castellanos, A. M. Brouwer, and Y. Ekinici, “Absorption coefficient of metal-containing photoresists in the extreme ultraviolet”, *J. Micro/Nanolithogr., MEMS, MOEMS*, 2018, **17**, 023505.
- R. Fallica, J. Haitjema, L. Wu, S. Castellanos, A. M. Brouwer, and Y. Ekinici, “Absorption coefficient and exposure kinetics of photoresists at EUV”, *Proc. SPIE*, 2017, **10143**, 101430A.
- Z. Wang, J. Xu, L. Wu, X. Chen, S. Yang, H. Liu, and X. Zhou, “Dissolution, hydrolysis and crystallization behavior of polyamide 6 in superheated water”, *Chin. J. Polym. Sci.*, 2015, **33**, 1334-1343.
- X. Qi, Z. Wang, S. Ma, L. Wu, S. Yang, and J. Xu, “Complexation behavior of poly(acrylic acid) and lanthanide ions”, *Polymer*, 2014, **55**, 1183-1189.

Acknowledgments

I would like to express my deepest appreciation to my supervisors—Dr. Sonia Castellanos and prof. Fred Brouwer for accepting my application, for the support and guidance during my PhD, and for making collaborations with so many different labs and groups possible. Sonia provided me with advice and encouragement throughout every project. Even after she left ARCNL, she offered her weekend hours reviewing each chapter of this thesis. Fred also reviewed the whole thesis and provided valuable advice to the Introduction and Chapter 6 in particular. Both supervisors kindly joined the team to SOLEIL synchrotron and Swiss Light Source to give a hand when we were busy with beamtimes at different beamlines/synchrotrons.

I would also like to express my sincere gratitude to prof. Wybren Jan Buma, prof. Bas de Bruin, Dr. Stefania Grecea, prof. Reinder Coehoorn, prof. Moniek Tromp, and Dr. Roberto Fallica, for accepting the invitation to be part of the doctorate committee and for offering the time reviewing the manuscript.

I very much appreciate my coworkers and collaborators from ARCNL, UvA, AMOLF, Paul Scherrer Institute, SOLEIL synchrotron, and the University of Groningen. The works in this thesis would not have been done without their help. Thanks to Yu Zhang as my best synchrotron buddy and for the discussion and her experience sharing at our teatime, Jarich Haitjema for his help in elipsometry, SOLEIL and PSI visits, Olivier Lugier for his help in XPS, STXM and night shifts, Neha Thakur for her kind help during PSI and SOLEIL visits, especially in night shifts, Ivan Bepalov for the major contribution to the STXM measurement and analysis, Martijn Tiekink for the synthesis of carbazole benzoic acid and assistance in SOLEIL, Jeremy Liu for conducting the ligand exchange experiment with resins and the best lab journal notes that I have seen, Martijn and Jeremy again for their enthusiasm in their internship projects; to Michiel Hilbers of UvA for the laser alignment and his help with confocal microscope; to Michaela Vockenhuber, Dimitrios Kazazis, Roberto Fallica, Li-Ting Tseng, and Yasin Ekinci of XIL-II beamline and LMN in PSI for the help with EUV openframe exposure experiments, interference lithography and transmission measurements; to Katharina Witte and Benjamin Watts of the PulLux beamline in PSI for the help with STXM

measurement and discussion; to Milos Baljovic and Thomas Jung of LMN in PSI for the help with XPS; to Alexandre Giuliani and Laurent Nahon at the DESIRS beamline of SOLEIL synchrotron for the help with the VUV-MS experiments and data processing; and to Giuseppe Portale of RUG for the GISAXS measurement and analysis. To all those beamline scientists again who set examples for me by analyzing and solving problems calmly, no matter what happened. Thanks should also go to people of AMOLF: Mark Willemse and Niels Winkelaar for wafer dicing, and Bob Drent, Dimitry Lamers, Andries Lof, and Igor Hoogsteder for their technical support in the NanoLab.

Special thanks to Maarten van der Geest and Jarich for their help with de samenvatting, Mark Koenis for his kind help with thesis formatting, and Olivier and Najmeh Sadegh for being my paranympths. To Pavel Antonov, Victor Vollema, and Fiona Elam for their help with AFM in ARCNL. Also to Sander van Leeuwen, Mark Mol, Hans Sanders, Wim Roeterdink, and Michiel for their technical supports in the labs. To the staff of the Molecular Photonics Group: Fred, Sonia, prof. Wybren Jan Buma, prof. Sander Woutersen, prof. Hong Zhang, Dr. René Williams, and Dr. Annemieke Pettrignani for their comments and suggestions in the discussion during group meetings. To Wim van der Zande, Claire van Lare, and Sander Wuister of ASML for the information and feedback. To Silang Zhou and Si (Crystal) Chen who provided me with a bed and dinner every time I visited RUG for experiments.

I would like to thank all the colleagues and alumni of the Molecular Photonics Group in UvA, the EUV Photoresists, Nanophotochemistry and other groups in ARCNL for the nice working atmosphere: Bruno Martins (my first lunch buddy and a very helpful and welcoming colleague), Robbert Bloem (the source of news and suggestions), Olivier (a perfect office mate who always gave off calm vibes), Carin Werner, Lotte Metz (who was always enthusiastic every time I met her in the lab), Paul Le Lan, Felix Martin (who made a nice manual for QCM), Marie-Noëlle Amairi, Marco Wemekamp, Unnati Pokharel, Aniket Thete, Ivan Bespalov (who clarified the charging effects in LEEM for me), Quentin Evrard, Dongdong Zheng (the cuvettes provider), Dina Petrova (the group activity organizer and who changed the way of group meeting), Yansong Feng (the desiccator opener and chemicals search engine), Yanni Wu (a very nice neighbor in the lab), Benjamin Strudwick, Roberto Cota, Maximilian Paradiz (“a very smart person” remarked by Dongdong), Hernán Velásquez, Jiayun Fan, Ivan Romanov, Federico Modesti, Daire Gibbons, Zoi Melissari, Begum Demirkurt, David van Grinsven, Chao Chun Hsu and many others.

Many thanks to my supervisors and colleagues during my master’s project in RUG. The experience in the Feringa Group equipped me with synthesis skills and Dr. Depeng Zhao, my daily supervisor at the time, supported my application for the PhD position. To my supervisor and alumni during my bachelor’s study at Donghua University who encouraged me to open my mind, to become an independent researcher, and to take a step to go to Groningen in the first place.

This year has been difficult for everyone. Mengqi (Maisie) Du of ARCNL and my dear friends Lu Wang in Montreal, Shiqi Xia in Nanjing, and Si Chen in

Groningen were particularly helpful to me at a few times during my writing when I got very emotional from the combination of quarantine, homesickness and the deadline for submission.

Last but not least, I would like to thank my parents for their unconditional love and support.

